

## University of Southampton Research Repository ePrints Soton

Copyright © and Moral Rights for this thesis are retained by the author and/or other copyright owners. A copy can be downloaded for personal non-commercial research or study, without prior permission or charge. This thesis cannot be reproduced or quoted extensively from without first obtaining permission in writing from the copyright holder/s. The content must not be changed in any way or sold commercially in any format or medium without the formal permission of the copyright holders.

When referring to this work, full bibliographic details including the author, title, awarding institution and date of the thesis must be given e.g.

AUTHOR (year of submission) "Full thesis title", University of Southampton, name of the University School or Department, PhD Thesis, pagination

**UNIVERSITY OF SOUTHAMPTON**

FACULTY OF ENGINEERING, SCIENCE AND MATHEMATICS

School of Physics and Astronomy

**Silicon Photomultipliers in Radiation Sensing Applications**

by

**Mark Abbott Foster**

Thesis for the degree of Doctor of Philosophy

September 2010

UNIVERSITY OF SOUTHAMPTON

## ABSTRACT

FACULTY OF ENGINEERING, SCIENCE & MATHEMATICS

SCHOOL OF PHYSICS AND ASTRONOMY

Doctor of Philosophy

SILICON PHOTOMULTIPLIERS IN RADIATION SENSING APPLICATIONS

by Mark Abbott Foster

The Silicon Photomultiplier (SiPM) is a novel photon sensing device, with potential applications in particle physics, astronomy and general gamma-ray spectroscopy.

Various SiPM designs were evaluated for these roles by coupling them to a range of scintillators, including LSO, NaI(Tl) and CsI(Tl). It was found that a LSO-SiPM gamma-ray detector provide sufficiently good energy resolution (11% at 511keV) in a very compact package to be of interest in PET imaging. SiPMs were also found to provide competitive spectra to PIN diodes of comparable area ( $1\text{cm}^2$ ) when coupled to CsI(Tl), raising interest in gamma-ray astronomy where a CsI(Tl)-SiPM detector could be used as an imaging element.

Good performance with CsI(Tl) encouraged investigation of SiPMs in the gamma-ray spectroscopy role, specifically radioisotope identification with portable instruments. The ScintiSphere concept was exploited to allow a larger, more sensitive detector to be built using SiPMs without sacrificing spectral quality. An 8cc sphere of CsI(Tl) coupled to a  $1\text{cm}^2$  SiPM array was found to give a noise floor of 35keV and a resolution of 9% at 662keV, closely comparable to a 0.8cc square crystal, despite the factor of 10 improvement in sensitive volume.

Neutron detection with a SiPM array is achieved using LiI(Eu), which was found to resolve thermal neutron captures to 12% FWHM and achieve excellent gamma-ray rejection. In this application, SiPMs are preferable to PIN diodes as they are immune to direct gamma-ray interactions which could degrade gamma-ray rejection. When packaged in a compact moderator of 15mm depth and volume 58cc of HDPE, a compact neutron counter was built and found to be slightly more efficient than a 3"  $\text{He}^3$  tube packaged in 16mm of HDPE.

Finally, an instrument is proposed that exploits the intrinsic advantages of SiPMs. The use of SiPMs with LaBr(Ce) is explored and simulations are carried out of a directional spectrometer, predicted to locate a  $\text{Cs}^{137}$  source of 1mC at 2m to within  $15^\circ$  in 15 seconds.

In conclusion, it is found that SiPMs should be of great interest in these fields due to providing comparable performance to existing systems whilst providing additional benefits such as low power electronics, high gain and immunity to direct X-ray interactions.

# Contents

<b>Abstract</b>	<b>ii</b>
<b>List of Contents</b>	<b>iii</b>
<b>List of Figures and Tables</b>	<b>viii</b>
<b>Declaration of Authorship</b>	<b>xv</b>
<b>Acknowledgements</b>	<b>xvi</b>

## **1. Context and Introduction - Ionising Radiation Sensing**

1.1. The Scintillation Mechanism Briefly Outlined	2
1.1.1. Comparison of Common Scintillators	3
1.2. Detection of Alpha and Beta Particles	5
1.2.1. Interaction of Alpha Particles with Matter	5
1.2.2. Interaction of Beta Particles with Matter	7
1.2.3. Alpha and Beta Particle Detectors	8
1.3. Detection of Neutrons	9
1.3.1. Interactions of Neutrons with Matter	9
1.3.2. Scintillators in Neutron Detection	10
1.4. Detection of Gamma-Rays	11
1.4.1. Interactions of X-rays and Gamma-rays with Matter	11
1.4.2. Gamma Detection Using Scintillators	13
1.4.3. Design of Gamma-Ray Spectrometers	15
1.5. Photodetectors in Ionising Radiation Sensing with Scintillators	18
1.5.1. Photomultiplier Tubes	19
1.5.2. PIN Photodiodes	20
1.5.3. Avalanche Photodiodes	21
1.6. Conclusion	22

## 2. SiPMs in Radiation Sensing

2.1. Silicon Photomultiplier Operating Principle	23
2.2. SiPM Characteristics	26
2.2.1. Factors Affecting Gain	26
2.2.2. Gain Uniformity	26
2.2.3. Photon Detection Efficiency	28
2.2.4. Dark Current	32
2.2.5. Linearity and Dynamic Range	33
2.2.6. Optical Cross-talk	34
2.2.7. Afterpulsing	35
2.2.8. Radiation Hardness and Magnetic Field Insensitivity	37
2.2.9. An Alternative SiPM Design: Back-Illuminated SiPMs	37
2.3. Comparison of SiPMs With Other Photosensors	39
2.4. Potential Interest in SiPMs in Gamma-Ray Sensing	40
2.5. Conclusion	42

## 3. Evaluation of SiPMs with Small Scintillators

3.1. Testing Single SiPMs using Small Crystals	43
3.1.1. Equipment and Preliminary Tests	45
3.1.2. Measurements Using CsI(Tl) and LSO	48
3.1.3. Notes on Geant4 Optical Monte Carlo	51
3.1.4. Simulations and Predictions of Energy Resolution	52
3.1.5. Linearity and Scintillator Proportionality	54
3.2. Potential Applications of Single SiPMs	55
3.2.1. Positron Emission Tomography	55
3.2.2. Personal Dosimetry	56
3.2.3. Summary of Work on Single 3x3mm SiPMs	57
3.3. Tiled Arrays of Silicon Photomultipliers	57
3.3.1. Construction of Tiled Arrays	58
3.3.2. Measurement of Uniformity Across the Array	59
3.3.3. Comparison of Different Scintillators with SiPMs	60
3.3.3.1. Measurements	63
3.3.3.2. Discussion	66
3.3.4. Comparison of Different Array Sizes	66

3.3.4.1.	Measurements and Discussion	67
3.3.4.2.	Summary on Tiled Arrays	69
3.3.5.	Potential Applications of Tiled Arrays with CsI(Tl)	70
3.3.5.1.	Gamma-Ray Spectroscopy for Security Purposes	70
3.3.5.2.	Gamma-ray Astronomy	71
3.3.6.	Potential Improvements in Small SiPM-based Gamma Detectors	72
3.3.6.1.	Improvements in SiPM Technology	72
3.3.6.2.	Application of Recent High-Performance Scintillators	72
3.4.	Conclusion of Evaluation of SiPMs in Radiation Sensing	74

## **4. Development of a Practical Portable Spectrometer**

### **Using SiPMs**

4.1.	Introduction	75
4.1.1.	Requirements and Specification	75
4.1.2.	Exploiting a Novel Scintillator Configuration	76
4.2.	Initial Testing of a Large Sphere for Handheld Spectrometers	77
4.2.1.	Measurement of Energy Resolution	78
4.2.2.	Noise Floor	80
4.2.3.	Conclusion	80
4.3.	Improvement of LCE by Reducing Sphere Volume	81
4.3.1.	Measurement and Discussion	81
4.3.2.	Summary	83
4.4.	Reducing Noise by Reducing SiPM Area	84
4.5.	Combination of a 9-Element Array and Small ScintiSphere	85
4.5.1.	Measurements	85
4.5.2.	Summary on Small Volume ScintiSpheres	89
4.6.	Use of Cooling to Improve Noise Floor	90
4.6.1.	Dark Current with Temperature	90
4.6.2.	Measurements of How Spectral Performance is Improved by Cooling	92
4.6.3.	Conclusion on Cooling	94
4.7.	Conclusions on SiPMs in Practical Spectroscopy	95
4.8.	Potential for Future Improvement	95

## 5. Neutron Detection Using SiPMs

5.1. Introduction	97
5.1.1.Using SiPMs in Neutron Detection	99
5.1.2.A Practical Specification	99
5.2. An Evaluation Detector	100
5.2.1.Choice of Scintillator	100
5.2.2.Neutron Moderation	103
5.2.3.Summary	104
5.3. Detector Design	105
5.3.1.Optical Design Constraints	105
5.3.2.Optical Simulations	106
5.3.3.Moderator Design Considerations	109
5.3.3.1. Efficiency	109
5.3.3.2. Directional Uniformity	111
5.3.4.Moderator Design for an Evaluation Device	112
5.3.5.Sensitivity Simulations	112
5.4. Evaluation Detector Testing	113
5.4.1.Measurement of Optical Performance and the Pulse Height Spectrum	113
5.4.2.ROC Curve Analysis as a Tool for Judging Sensitivity	115
5.4.3.Sensitivity Measurements	116
5.4.4.Directionality Uniformity	119
5.4.5.Analysis of Spectral Artefacts	121
5.4.6.The Temperature Response of the SiPM-LiI(Eu) Combination	123
5.4.7. Summary of the Evaluation Device	124
5.5. Potential Improvements	125
5.5.1.Removing Inefficient Use of Volume	125
5.5.2.Exploiting the Operator as Extra Neutron Moderator	126
5.6. Conclusion on SiPMs in Neutron Detection	128

## **6. Preliminary Study of a Directional Spectrometer**

6.1. Key Requirements	129
6.2. Existing Directional Spectrometer Systems	129
6.3. Detector Concept and Operating Principle	130
6.4. Calculating the Transfer Function	132
6.5. Trial Design and Predicted Performance	134
6.5.1. Optical Performance	134
6.5.2. Directional Response Simulation Method	136
6.5.3. Directional Response Simulation Results	137
6.5.3.1. Calculating Directional Resolution	137
6.6. Summary	139

## **7. Summary**

7.1. Gamma-Ray Sensors	141
7.2. Neutron Counters	144
7.3. A Potential Instrument Exploiting Silicon Photomultipliers	145
7.4. Final Conclusion	145

## **8. References**

8.1. Chapter 1	146
8.2. Chapter 2	148
8.3. Chapter 3	151
8.4. Chapter 4	153
8.5. Chapter 5	154
8.6. Chapter 6	156

# List of Figures and Tables

## 1. Context and Introduction - Ionising Radiation Sensing

Figure – 1.1: A sketch of the energy levels in a scintillator.	2
Table – 1.1: The key properties of a range of commonly used scintillators.	3
Figure – 1.2: A plot of the energy deposit rate (per unit penetration depth) as a function of penetration depth.	5
Figure - 1.3: A sketch of alpha particle flux with increasing penetration depth	6.
Figure – 1.4: The range-density product of a selection of materials plotted against alpha particle energy.	6
Figure – 1.5: A sketch of how the electron flux of a parallel beam falls off with penetration depth into a sample material.	8
Figure-1.6: A diagram outlining the Compton scattering process	12
Figure – 1.7: A sample energy deposit spectrum of a 7.5cm cylindrical NaI(Tl) scintillator read out by a PMT.	14
Figure 1.8: A sketch of the three possible paths taken by optical photons from the interaction side (black circle) to the photosensor.	16
Figure – 1.9: A sketch of the PMT operating principle. Photoelectrons at the cathode are accelerated into the dynode chain where gain is applied.	19

## 2. SiPMs in Radiation Sensing

Figure-2.1: The structure of a typical SiPM microcell.	24
Figure-2.2: A microphotograph of the surface a SiPM photodiode.	24
Figure 2.3: Plots of relative gain showing the uniformity of a Hamamatsu SiPM.	27
Figure-2.4: A plot showing the response of a SiPM to small numbers of photons, demonstrating the ability to count single photons.	28
Figure – 2.5: A repeat of Figure – 2.1.	29

Figure – 2.6: A plot of how light transmission falls off with penetration depth. Also shown is the electric field structure of the SiPM (compare to Figure – 2.5).	30
Figure–2.7: A plot of data provided by SensL for a 3035 SiPM showing how PDE varies with photon wavelength for a 2V overvoltage.	31
Figure-2.8: Data showing how dark noise varies with temperature taken using a 1mm <sup>2</sup> Hamamatsu MPPC (SiPM) operating at a range of bias voltages. (This image is taken from [2-12]).	32
Figure–2.9: This figure shows the calculated linearity of a notional SiPM.	33
Figure–2.10: Optical photons escaping SiPM microcells. Taken from [11].	34
Figure–2.11: A series of microphotographs of trenches cut into the top surface of a SiPM to reduce crosstalk.	35
Figure-2.12: Time distributions of afterpulses for three bias voltages in a 1mm <sup>2</sup> Hamamatsu SiPM. (Taken from ref. [2-16]).	36
Figure-2.13: A diagram of a back-illuminated SiPM taken from [2-21].	38
Table-2.1: Advantages and Disadvantages of SiPMs in Gamma-ray sensing	39
Table – 2.2: A comparison of typical scintillators in the context of use with SiPMs.	41

### 3. Evaluation of SiPMs with Small Scintillators

Figure-3.1: Photon detection efficiency of a SensL 3035 as a function of wavelength.	45
Figure-3.2: A photograph of a SensL 3035 SiPM set into a T08 can with a CsI(Tl) and a LSO crystal, both wrapped in PTFE.	46
Table–3.1: Properties of the SensL 3035 SiPMs used in this study.	46
Table-3.2: The key properties of LSO and CsI(Tl), the scintillators chosen for the initial evaluation of SiPMs.	47
Figure–3.3: Spectra obtained with a single SiPM with LSO and CsI(Tl).	48
Table–3.3: Noise floors and resolutions taken from the spectra above. The upper panel is LSO and the lower is CsI(Tl).	49

Figure-3.4: The measured dark noise continuum of a SensL 3035 with an integration time constant of $2.2\mu\text{s}$ .	50
Table-3.4: The predicted resolution of a $2\times 2\times 15\text{mm}$ scintillator coupled to a 3035 SiPM, for both LSO and CsI(Tl)	53
Figure-3.5: A photograph of three SiPM arrays obtained from SensL. From right to left, they have 16, 9 and 4 elements. Also shown are the CsI(Tl) crystals obtained from Hilger to test them.	59
Figure-3.6: A plot of gain consistency over the 16-element array. The $2\times 2\times 15\text{mm}$ CsI(Tl) scintillator was used.	60
Table-3.5: A table of the scintillators considered in this part of the study.	61
Figure – 3.7: The emission spectra of the scintillators tested. On the secondary axis we also show the SiPM PDE spectrum.	62
Table-3.6: The measured energy resolution at $662\text{keV}$ and noise floor at the 1cps level of the scintillators considered here.	63
Figure – 3.8: The $\text{Cs}^{137}$ spectra taken with the five different scintillators under test.	64
Table-3.7: The measured performance of the three arrays with their respective CsI(Tl) crystals, each sized to provide the same light collection efficiency in each case.	67
Figure-3.9: Some spectra taken with the 16-element array and the $14\times 14\times 28\text{mm}$ CsI(Tl) crystal.	68
Figure-3.10: Spectra taken in the same manner using the 9-element array and the $10\times 10\times 20\text{mm}$ CsI(Tl) crystal.	68
Figure – 3.11: A sample $\text{Cs}^{137}$ spectrum taken from ref [3-23], showing the good performance attained by coupling LaBr(Ce) to an APD. Note that the $32\text{keV}$ peak is visible.	73

## 4. Development of a Practical Portable Spectrometer Using SiPMs

Figure – 4.1: A sketch of the scintillator configuration and packaging.	77
Figure–4.2: Spectra obtained with the first ScintiSphere, a 112cc volume of CsI(Tl) read out by a 16-element array of 3035 SiPMs.	78
Table-4.1: A breakdown of the terms contributing to energy resolution at 662keV for the 112cc sphere (upper panel) and the 100cc sphere with PIN diode (lower panel).	79
Figure–4.3: 662keV gamma-ray spectra taken with each size of sphere. Note how the 64cc and 47cc spheres appear to have the same LCE.	81
Table–4.2: The performance of a range of sphere sizes quantified as noise floor and energy resolution at 662keV. Also shown is the small block for comparison.	82
Table–4.3: The number of counts in the 662keV photopeak as measured by the range of ScintiSpheres, the small block (illuminated from the side).	83
Table–4.4: The performance of a range of spheres and square blocks demonstrating the differences of the 9-element at 16-element array.	84
Figure–4.4: The configuration of the 8cc ScintiSphere packed in AIO and viewed through a glass slide. The glass-slide spacer was necessary due to the array being built onto an oversized glass slide.	85
Figure-4.5: Gamma-ray spectra in the range 59keV to 1330keV obtained with an 8cc sphere and a 9-element SiPM array.	86
Table-4.5: The energy resolutions obtained using the 8cc sphere coupled to a 9-element SiPM array.	86
Table-4.6: The breakdown of the predicted resolution of the 8cc ScintiSphere at 662keV. Each term is expressed in the photons at the $1\sigma$ level, except the FWHM.	87
Table-4.7: The comparative sensitivity of two ScintiSpheres and the 10x10x20mm block, expressed as the number of counts in the 662keV photopeak of $\text{Cs}^{137}$ .	87
Table-4.8: The linearity of the 8cc ScintiSphere measured as the channel number of a range of gamma-ray energies.	88

Figure-4.6: Plots of the data in table-4.8. The deviation even at 1330keV is small, indicating a reasonably linear response.	89
Figure-4.7: A sketch of the 21cc ScintiSphere with the cooling apparatus required to cool the 16-element array.	90
Table-4.9: The recorded dark current as a function of SiPM temperature, taken with a 16-element array of 3035 SiPMs. The bias voltage changes also shown were required to maintain the same gain.	91
Figure-4.8: A plot of the above data, how dark current varied with temperature. The horizontal error bars are the accuracy of the temperature sensor.	92
Table-4.10: The peak channel numbers of a range of gamma-ray energies taken at different temperatures. The gain change is calculated based on the 662keV photopeak.	93
Figure-4.9: Gamma-ray spectra taken with a SiPM cooled by 10K to 15°C.	93

## 5. Neutron Detection Using SiPMs

Figure - 5.1: The energy spectrum of Cf <sup>252</sup> fission neutrons. Taken from [5-2].	98
Table-5.1: The key properties of the two lithium-based scintillators useful in thermal neutron detection. [5-11], [5-10], [5-12], [5-13],	102
Figure-5.2: The inelastic collision of a neutron with a nucleus.	103
Figure-5.3: A cross-section of the scintillator package from Scionix.	105
Table-5.2: The results of optical simulations of the scintillator shown in Figure-5.3 and a light guide.	107
Figure – 5.4: Plots of the LCE and VLCE with increasing light guide length.	107
Figure-5.5: Plots of energy resolution terms for LiI(Eu). (Taken from [5-11]).	108
Table-5.3: The breakdown of energy resolution for both the 4.8MeV neutron capture peak and 1330keV Co <sup>60</sup> gamma-ray photopeak in LiI(Eu).	109
Figure-5.6: A scintillator shown in grey within a white HPDE moderator with four possible neutron paths.	110

Figure-5.7: A sketch of the neutron detector tested here. On the left are some properties including the volume fraction of the LiI(Eu) scintillator itself.	112
Table-5.4: The predicted performance of the neutron detector for a shielded and unshielded $4 \times 10^4$ n/s $\text{Cf}^{252}$ source.	113
Figure-5.8: Pulse height spectra of thermal neutron captures and $\text{Co}^{60}$ gamma-rays.	114
Figure-5.9: An example ROC curve describing how the false positive probability and true positive probability are both linked for a given alarm threshold and count rate.	116
Figure-5.10: The basic configuration of the sensitivity measurements, showing the detector within its moderator and the HDPE shield surrounding the source.	117
Table-5.5: A comparison of the simulated and measured count rates of the LiI(Eu) neutron counter in a 38x48mm HDPE moderator.	117
Table-5.6: The measured performance of the neutron detector tested here, compared against a common $\text{He}^3$ -based detector used in a similar role.	118
Figure – 5.11: The ROC curve for the neutron detector when exposed to an unshielded neutron source.	119
Table-5.7: The directional uniformity of the compact detector when exposed to a shielded source.	120
Figure-5.12: A plot of the above data with error bars set at $1\sigma$ .	120
Table-5.8: Peak and Continuum Count-rates with Varying Moderator Configuration.	122
Figure-5.13: Three neutron spectra showing the thermal peak and continuum with varying moderator configurations.	122
Figure-5.14: The neutron spectra taken at three temperature intervals.	123
Figure-5.15: A thermal neutron spectrum compared to a $\text{Co}^{60}$ spectrum from the AST datasheet for GS20.	126
Table-5.9: Data taken using the LiI(Eu) scintillator demonstrating how the operator may be used as additional moderator.	127

## 6. Preliminary Study of a Directional Spectrometer

Figure-6.1: A sketch of the four detector elements and the definition of coordinates	131
Figure-6.2: $F(0)$ (in blue) and $F(\Psi)$ (in red) and their resolutions.	133
Table-6.1: The scintillation properties of LaBr(Ce). Taken from the Brilliance380 product datasheet [6-6].	134
Table-6.2: A breakdown of the predicted energy resolution at 662keV.	135
Figure-6.3: The response of detectors A and B to a 662keV gamma-ray source at a range of positions from boresight (Angle=0°) to side-on (Angle=90°).	137
Figure-6.4: The transfer function $F$ calculated from the simulated data in Figure-6.3.	138
Figure-6.5: Predicted transfer function for 180keV gamma-rays using an integration time of 15s.	139

# DECLARATION OF AUTHORSHIP

I, ....**Mark Foster**.....,

declare that the thesis entitled

..... **SILICON PHOTOMULTIPLIERS IN RADIATION SENSING APPLICATIONS** .....

and the work presented in the thesis are both my own, and have been generated by me as the result of my own original research. I confirm that:

- this work was done wholly or mainly while in candidature for a research degree at this University;
- where any part of this thesis has previously been submitted for a degree or any other qualification at this University or any other institution, this has been clearly stated;
- where I have consulted the published work of others, this is always clearly attributed;
- where I have quoted from the work of others, the source is always given. With the exception of such quotations, this thesis is entirely my own work;
- I have acknowledged all main sources of help;
- where the thesis is based on work done by myself jointly with others, I have made clear exactly what was done by others and what I have contributed myself;
- parts of this work have been published as: M.A.Foster and D.Ramsden, "A Compact Neutron Detector Based on the use of a SiPM Detector," IEEE Nuclear Science Symposium Conference Record, (2008), 1882-1886

**Signed:** .....

**Date:**.....

# Acknowledgements

I would like to begin by thanking my parents for their never ending support, without which I would not have even been able to begin.

I thank Dr David Ramsden and Dr Tony Bird whose supervision and guidance made this project possible. I am also grateful to the staff of Symetrica Ltd for their sponsorship and giving me this opportunity. From the university, I would like to thank the mechanical workshop staff for their assistance in machining parts, and Dave Clark for his advice on using Geant.

Last (but not least) I thank my girlfriend Moina, who has put up with me and my thesis for the last three years.

# 1. Context and Introduction - Ionising Radiation Sensing

Ionising radiation and its detection represent a fascinating and ever-evolving field of physics, both theoretical and experimental. The ability to detect ionising radiation made atomic and nuclear physics possible, including Rutherford's use of alpha particles to disprove the "plum pudding" atom, and the discovery of radioactive nuclear decay and nuclear fission as a result.

Our understanding of the universe at large has also been improved by the ability to measure ionising radiation, ever since Geiger-Muller tubes were carried into orbit aboard the Explorer satellites. Their discovery of the Van Allen radiation belts, comprised of protons and electrons trapped from the solar wind by the geomagnetic field was key to our understanding of solar-terrestrial interactions. A range of balloon- and space-borne experiments over the last fifty years have observed the far reaches of the universe in gamma-rays and X-rays, leading to a range of discoveries, such as the accretion of hot matter about black holes, and exceptionally violent supernovae that give out a brilliant burst of gamma-rays. Detailed observations have only been possible since the Space Age, as X-rays and gamma-rays cannot penetrate the Earth's atmosphere to ground level and so observatories must be in space, or at high altitude. Medicine and medical science were early benefactors of the new field of physics, where X-rays were used in the first medical imaging technique. A range of medical techniques use radiation for diagnosis by imaging (such as X-rays and PET) or for treatment by killing undesirable cells.

This thesis is a study of how Silicon Photomultipliers (SiPMs), a recently developed photosensor, may be used in radiation sensing. Therefore we are limited to the study of technologies that convert ionising radiation into visible photons. This chapter then serves as an introduction to the detection and measurement of radiation by scintillation. To begin with, the process of scintillation is outlined and the range of scintillating materials is discussed. This chapter then outlines how specific forms of ionising radiation interact with matter and may be detected using scintillators. Finally, current photosensors are described, in order to set the use of Silicon Photomultipliers into context and to define the terms used. Chapter 2 describes in detail the silicon photomultiplier (SiPM) and compares it against the photosensors outlined below to gain understanding of how SiPMs may fit into radiation sensing using scintillators. The remainder of this thesis will present the experiments carried out to test this understanding and to develop it further by finding potential applications where SiPMs may offer distinct advantages over other photosensors. Effort then goes into developing SiPM-based radiation sensors for specific applications.

### 1.1. The Scintillation Mechanism Briefly Outlined

The process of scintillation is the conversion of a charged particle's kinetic energy into optical photons, which may be detected by a photosensor. The exact process varies depending on the scintillator structure, but they all share the same premise. That is, an ionising particle passes through the material and excites a number of electrons into the conduction band. If these electrons were to simply decay by photon emission, these photons could be reabsorbed and the material would not be transparent to its own emissions. Taking the commonly used alkali halide crystal NaI(Tl) as an example, a small concentration ( $10^{-3}$  mole) of thallium is added as an "activator". A different energy structure exists around the thallium atoms in the crystal, between the conduction and valence bands of the NaI. Figure – 1.1 shows an example energy structure.

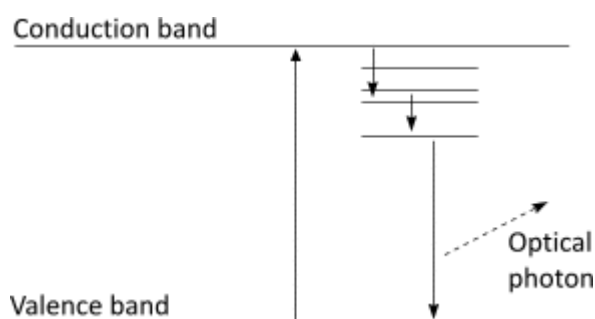


Figure – 1.1: An electron is excited into the conduction band. It then falls into the energy levels of the activator, undergoing an optical transition into the valence band.

Excited electrons may travel to these atoms and fall into the different energy structure, which includes an optical transition. As this optical transition is of less energy than the band gap, the photons will not be absorbed. Therefore, the photon's energy spectrum is that of the activator, not the crystal itself. Also, the length of the scintillation light pulse is determined by the lifetimes of the activator's energy states. The number of photons emitted is theoretically proportional to the energy of the exciting particle and therefore counting these photons allows the energy to be inferred.

Other scintillators, such as organic scintillators, rely on the same premise, but have more complicated energy structures that do not require a dopant as an activator. More details may be found in [1-1].

### 1.1.1. Comparison of Common Scintillators

Detection of radiation using scintillators dates back to the beginning of the 20th century (Rutherford used zinc sulphide, for example), though scintillator development continues to the present day. The most common scintillators are solid, though liquid and gaseous scintillators exist. Solid scintillators are preferred in many applications, such as gamma-ray astronomy and medical imaging, for their high density and superior light yield. Density is especially important for gamma-ray detection, to improve the interaction cross section and sensitivity.

The principal properties of scintillators are the light yield, density and time-constant. The light-yield is the number of optical photons emitted per unit deposited energy. Note that this is the energy deposited by an electron; light yields are typically lower for alpha particles.

Table – 1.1 shows the key properties of a range of common scintillators [1-2], [1-3], [1-4], [1-5], [1-6], [1-7], [1-8] :

	<b>Density</b>	<b>Yield</b>	<b>Peak emission</b>	<b>Time constant</b>
	g/cc	ph/MeV	nm	ns
NaI(Tl)	3.7	38000	420	230
CsI(Tl)	4.5	52000	550	1000
CsI(Na)	4.5	41000	415	600
LYSO(Ce)	7.4	32000	420	40
BGO	7.1	8500	480	300
LaBr(Ce)	5.1	63000	380	16
Lil(Eu)	4.08	11000	470	1500
EJ-200	1.02	10000	425	4

Table – 1.1: The key properties of a range of commonly used scintillators.

A high light yield is desired to improve statistics when counting photons to infer the energy deposited by an exciting particle. The emission spectrum is a factor in this since the photosensor should be most sensitive to photons emitted by the scintillator, and this is an important factor in designing scintillation counters. For example, photomultiplier tubes (see Section 1.5.1) with S11 photocathodes have their peak sensitivity between 400 to 450nm and so NaI(Tl) delivers excellent performance when coupled to such a photomultiplier. In contrast, CsI(Tl) has an emission peak at 550nm and delivers inferior performance despite having a higher light yield. CsI(Tl) is therefore rarely used with photomultiplier tubes but give excellent performance with silicon photodiodes which are more sensitive at longer wavelengths.

Zinc sulphide (ZnS(Ag)) is not available as a single large crystal, due to its tendency to grow in small platelets. It is therefore only available as a powder and it strongly attenuates its own light. It is best used in thin screens for detecting short-ranged particles like alpha-particles or low energy beta-particles. Its light yield is the highest known, contributing to its enduring popularity.

EJ-200 is unique amongst this list as it is an organic scintillator. Whilst it has the lowest density and lowest light yield, organic (plastic) scintillators have the advantage of cost and can easily be cast in larger volumes than inorganic crystals. Plastic scintillators are also robust and less susceptible to cracking.

Lithium iodide (LiI(Eu)) is also unique in that it is the only alkali halide that is sensitive to neutrons. This is achieved using  $\text{Li}^6$  to capture low energy neutrons. This leaves an excited  $\text{Li}^7$  nucleus which then decays into an alpha particle and a triton. The use of LiI(Eu) in neutron detection is explored in chapter 5.

BGO is the only inorganic scintillator on this list that does not require a dopant to act as an activator. The scintillation process is somewhat different and is more like that of organic scintillators than the alkali halides. Knoll gives some detail on this.

Hygroscopy is a frequent problem for scintillators, where exposure to water vapour breaks down the crystal. Most scintillators on the list above are hygroscopic, with the exceptions of EJ-200, BGO and LYSO. Hygroscopic crystals must be kept and used in air-tight containers and viewed through a glass window. CsI(Tl) however has such a slight hygroscopy that it may be used in air, though it must be kept dry and some slight degradation can be expected.

A final practical concern is internal radiation. On this list, LaBr(Ce) and LYSO contain a fraction of naturally occurring radioactive lanthanum ( $\text{La}^{138}$ ) and lutetium ( $\text{Lu}^{176}$ ) isotopes, respectively. Both of these are beta emitters. Internal radiation sources such as these increase the apparent background radiation and whilst this can be subtracted from spectra, it is still undesirable.

## 1.2. Detection of Alpha and Beta Particles

### 1.2.1. Interaction of Alpha Particles with Matter

Alpha particles interact almost exclusively through Coulomb attraction, giving energy to electrons as they pass and exciting them to higher bound states or even freeing them. Alpha particles are heavy compared to the electrons with which they interact so much energy is lost per collision and the alpha particle undergoes a small deflection, so their paths tend to be straight. The energy loss per collision increases as the alpha particle loses energy, which leads to an interesting feature known as the Bragg curve, seen in Figure – 1.2 which plots energy loss rate against penetration depth.

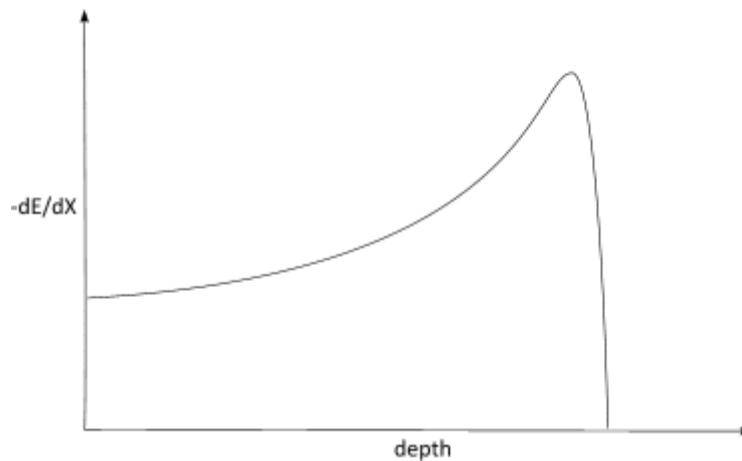


Figure – 1.2: A plot of the energy deposit rate (per unit penetration depth) as a function of penetration depth. Note how the function increases to a peak, due to the interaction cross-section increasing with decreasing energy.

Due to the shape of the Bragg curve, more of the particle energy is deposited at one depth than at any other, dependant on the initial energy. This is of interest in radiotherapy where a proton beam can be used to deposit a lot of energy directly into a tumour instead of any surrounding tissue. Alpha particles have a well-defined range, as shown in Figure –1.3, which is very short compared to other ionising radiations, limited to a few centimetres in air and a few microns in solids. The quoted mean range ( $R_m$ ) is the penetration depth where the flux ( $I$ ) has fallen to a half of its value at the surface ( $I_0$ ). Knoll [1-9] provides a more rigorous analysis of the stopping power of alphas in solids

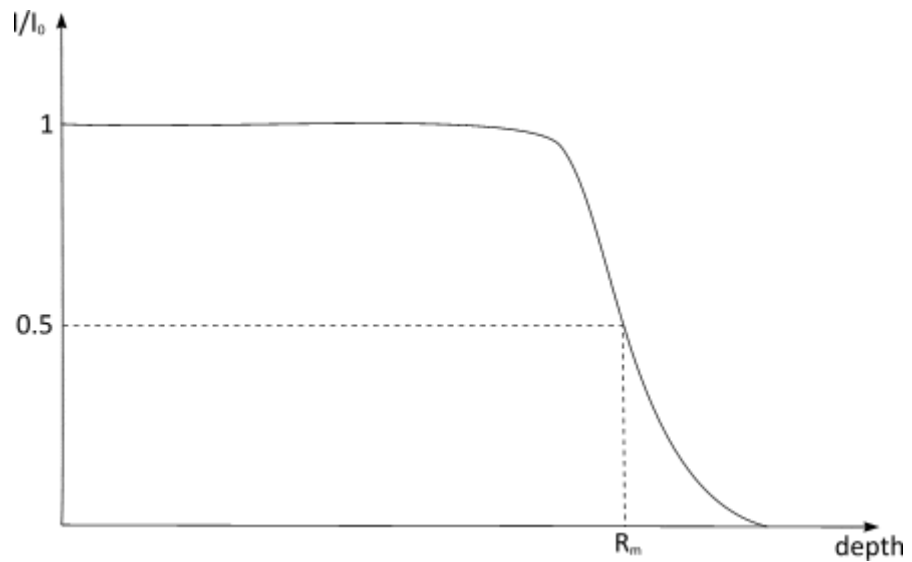


Figure - 1.3: A sketch of how alpha particle flux falls off with increasing penetration depth, assuming a sample material illuminated normal to one face by a parallel beam of monoenergetic alphas.

The range of a parallel beam of alpha particles depends strongly on energy and the density of the target material. Figure – 1.4 shows this by plotting (as a function of energy) the product of range and density for a selection of materials.

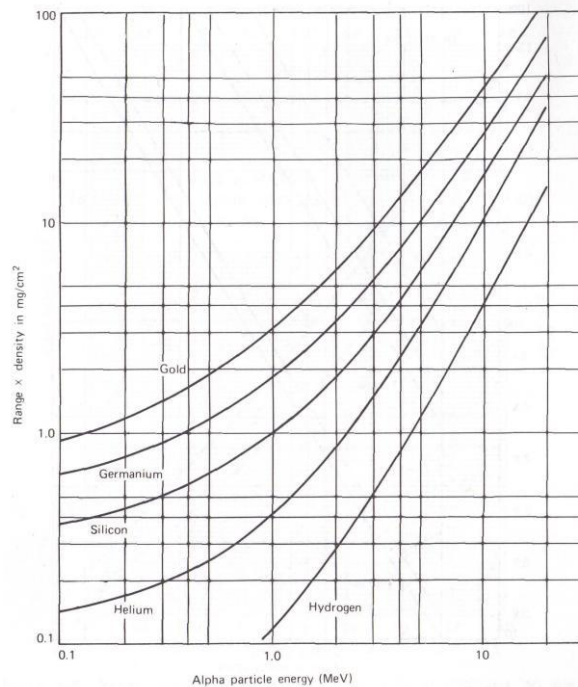


Figure – 1.4: The range-density product of a selection of materials plotted against alpha particle energy. These plots demonstrate the dependency of alpha particle range on density and energy. Taken from Knoll.

The highly ionising nature of alpha particles is also responsible for the lower light output of scintillators when excited by them. During alpha particle absorption in a scintillator, they ionise a much smaller volume than electrons and ionise it more highly, enough to cause a change in the electronic structure of the crystal. This manifests as a reduced light yield per unit energy deposited.

### **1.2.2. Interaction of Beta Particles with Matter**

Beta particles may be either electrons or positrons and so possess charge, and do not interact by the strong nuclear force. Therefore, Coulomb interactions with nuclei and electrons dominate. The vast majority of interactions are with electrons, as they are more numerous and nuclei account for only a small fraction of volume in matter.

Beta particles lose more energy per collision than alpha particles and scatter through greater angles as they are electrons scattering off electrons, so their path is more randomised. Energy may also be lost through bremsstrahlung radiation where decelerating electrons emit photons.

Positrons behave in largely the same way as electrons, as the energy loss per interaction is independent of the sign of the charge. The principle difference occurs at the end of the positron's track, when it has lost its energy, where it annihilates with an electron. This creates two co-linear gamma-rays of 511keV.

The range (defined as the depth where the flux falls by half) of electrons and positrons is not as well defined as that of alpha particles. This is due to the random nature of the scattering. Figure – 1.5 shows how flux falls off with penetration depth.

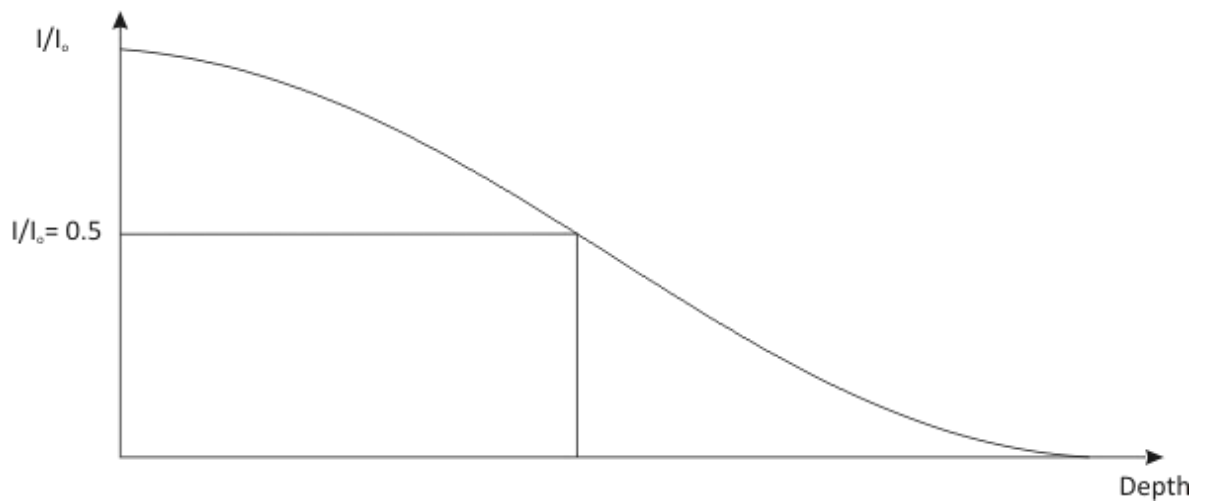


Figure – 1.5: A sketch of how the electron flux of a parallel beam falls off with penetration depth into a sample material.

Range in solids is typically short, and depends on electron density and beta particle energy. Beta particles incident on low density materials like plastic can be expected to lose energy at a rate of 1MeV per 2mm [1-10], though this rule of thumb applies in the energy range of a few MeV.

### 1.2.3. Alpha and Beta Particle Detectors

Detection of alpha particles using scintillators has changed little since the early 20<sup>th</sup> century. The short range of alpha particles in solid matter dictates that the scintillator be packaged with a very thin entrance window. Zinc sulphide (ZnS(Ag)) is a common solution to both these problems. It is only available as an opaque powder, which may be mixed with a binder or deposited onto a substrate to form a thin (<1mm thick) screen. A light guide couples one face to a small photosensor (typically a PMT). The opacity of ZnS(Ag) blocks out ambient light, whilst incident alpha particles can access it unimpeded. The opacity of ZnS(Ag) also prevents such a detector from providing spectroscopic information, as it attenuates its own scintillation light. The light loss depends on the depth of the interaction and is essentially random.

A dedicated beta particle detector can simply use a thicker window to block out alpha particles. ZnS(Ag) in this form attenuates its own light so energy information is lost and gamma-ray rejection relies on the low probability of interaction with the thin disk. A combined alpha/beta particle detector may be constructed using ZnS(Ag) deposited onto a thin (2-3mm) plastic scintillator, such as EJ-200, viewed by a PMT on the other face. Alpha particles are more likely to scintillate in the ZnS(Ag) and beta particles in the plastic, allowing for pulse shape discrimination based on the differing pulse lengths.

An alternative is the use of a silicon diode, typically a surface barrier detector or diffused junction detector [1-11]. The latter has the advantage of not having a thickness of silicon in front of the depletion region of the silicon diode, in which alphas can lose energy or be absorbed. The depletion region is the sensitive region of the diode where the p- and n-junctions of the diode meet and charges migrate between the two. No energy losses outside of the depletion region makes very accurate alpha spectroscopy possible with a very small and simple instrument as no photosensor is required.

### 1.3. Detection of Neutrons

#### 1.3.1. Interactions of Neutrons with Matter

Neutrons have neutral charge and so may only interact by the nuclear forces. Two interactions dominate: inelastic scattering and capture. In the former case, the neutron simply scatters off nuclei in the target material and the incident neutrons kinetic energy is shared between them depending on the nuclear mass. Equation 1.1 shows this relationship:

$$E_{(R|max)} = \frac{4A}{(1+A)^2} E_n \quad (1.1)$$

$E_R$  is the energy of the recoiling nucleus,  $A$  the atomic mass number and  $E_n$  the incident neutron energy. Note how a neutron will share more energy with a lighter nucleus with the lowest extreme being hydrogen, where the incident energy is shared equally. For this reason, neutrons are highly penetrating in high- $A$  materials like lead, but interact more readily with hydrogenous materials like water, plastic or biological tissue.

Neutrons may be captured by nuclei, leaving the latter in an excited state. If the new nucleus then de-excites by the emission of a gamma-ray, then this is termed neutron activation. More useful in neutron detection is when the new nucleus decays by the emission of a charged particle. Some isotopes are useful for this, the three most common are  $^3\text{He}$ ,  $^6\text{Li}$  and  $^{10}\text{B}$ , as they have high capture cross-sections and decay into energetic, heavy, charged particles. They therefore can be used as a method of converting neutrons into charged particles which may then be detected. The efficiency of neutron detection depends on the cross-section of the capture reaction which scales with the inverse of neutron velocity [1-12], so all neutron detectors are more sensitive to low energy neutrons.

Neutron detection may be achieved using both processes. Inelastic scattering may be used in neutron detection, using a scintillator having low- $A$  nuclei, such as plastic scintillators (see above) where hydrogen nuclei are displaced and then deposit the energy. This allows for some measurement of the neutron energy spectrum by unfolding the detector response from

the neutron energy spectrum. An alternative technique is to use a volume of hydrogenous material (water or plastic) as a neutron “moderator” that reduces the energy of an incident neutron until it is in thermal equilibrium with the material. By lowering the neutron’s energy, its capture cross-section with suitable nuclei is increased.

### 1.3.2. Scintillators in Neutron Detection

Neutron scintillators rely on a dopant or constituent element to capture neutrons and then decay, leading to heavy charged particles which then induce scintillation. For this reason, many neutron detectors resemble alpha particle or beta particle detectors.  $\text{Li}^6$  and  $\text{B}^{10}$  are dominant in this field, as they possess large thermal neutron capture cross sections of 940 barns and 3840 barns, respectively [1-13], and energetic decays. A greater capture cross section is exhibited by  $\text{He}^3$  at 5330 barns but there are no scintillators that contain  $\text{He}^3$ . It can only be used as a gas in a proportional counter, and so it is outside of this study. Proton recoil can be exploited using plastic scintillators, where hydrogen nuclei are displaced by energetic neutrons.

$\text{Li}^6$  has a single, highly energetic reaction for thermal neutrons with a Q-value of 4.8MeV which aids gamma-ray rejection, as the peak stands well above the common gamma-ray energy range. Lithium can be used as lithium iodide ( $\text{LiI}(\text{Eu})$ ), a rather dim scintillator with a long decay time but unique for its response to neutrons (see Table – 1.1). It is typically available only in small volumes due to cost and difficulties during manufacture but it is sensitive and the brightest neutron scintillator. Using lithium iodide is complicated by the fact that it is highly hygroscopic and so must be kept hermetically sealed.

Lithium can also be used as a dopant in glass in the form of an oxide with a cerium activator to create an alternative scintillator with similar sensitivity to thermal neutrons. Lithium glass is widely used in neutron counters where durability is desired, being resistant to high temperatures, relatively robust and not hygroscopic. It is available in a large range of shapes and sizes, including long fibres. It is also available with differing concentrations of  $\text{Li}^6$  in the lithium oxide, natural (7.5%), enriched (95%) and depleted (0.1%), depending upon application. As the intention is to count thermal neutrons, only the enriched case will be considered. Lithium glass is roughly half as bright as  $\text{LiI}(\text{Eu})$  but is better matched to PMT readout due to being very blue and quite fast.

The alternative to  $\text{Li}^6$  in scintillators is  $\text{B}^{10}$ , made attractive by its greater cross-section of 3840 barns and higher abundance in natural boron, avoiding the expense of enrichment. Boron oxide (or lithium fluoride) may be mixed with zinc sulphide to exploit the high light output of

the latter to make a thin neutron-sensitive screen. Such a detector may be constructed in the same way as an alpha/beta detector with a light guide and photosensor and relies on the same gamma-ray rejection method. The constraints placed on the choice of photodetector are few, the principal one being that the photosensor is itself not sensitive to gamma-rays. X-rays have sufficiently short range in silicon that they may deposit their energy directly within the depletion region of a photodiode, generating a large pulse that may be mistaken for a neutron.

#### **1.4. Detection of Gamma-Rays**

##### **1.4.1. Interactions of X-rays and Gamma-rays with Matter**

Gamma-rays and X-rays are high energy photons, though the energy ranges where these terms apply can be vague. For the purpose of this thesis, photons in the range 1keV to 10keV will be termed "X-rays" whilst those in the 10keV to 10MeV range will be termed "gamma-rays". Photons above 10MeV are not dealt with in this thesis.

Photons, although they possess no charge, are the mediators of electromagnetic force and this force dominates its interactions. In the X-ray and gamma-ray energy ranges considered here, most photon interactions are with electrons via two processes, photoelectric-absorption and Compton-scattering. The cross sections of each depend on photon energy and the electron density. Photons above 1.022MeV interact with nuclei by pair-production, where the photon's energy is used to create an electron-positron pair.

The relative probabilities of these reactions occurring depend on gamma-ray energy and  $Z$ , the average atomic number of the absorbing material. Lower energy gamma-rays are more likely to interact via the photoelectric effect, for a given  $Z$ , whilst Compton-scattering is more likely in low- $Z$  materials like plastic scintillators for a given gamma-ray energy. This makes spectroscopy more challenging as the energy loss spectrum will contain a greatly reduced full energy peak and a Compton continuum will dominate. Spectroscopy becomes more challenging when incident gamma-rays are not monoenergetic.

The photoelectric effect [1-14] is the name given to interactions where the entirety of the photon's energy is given to an electron. In the energy range of above 1keV, this is sufficient energy to free the electron; work functions are typically no more than a few eV. It will then move through the scintillator and deposit its energy as outlined above. The energy of the excited electron will be the gamma-ray energy less the work function, or binding energy of the electron's initial state.

A photon may scatter off an electron in Compton scattering, giving it a fraction of its energy. Again, the electron will then scatter amongst any others in the material until it escapes or is

recaptured by a positive ion. The incident gamma-ray may then interact again by any process. Figure –1.6 shows a sketch of a scattering collision.

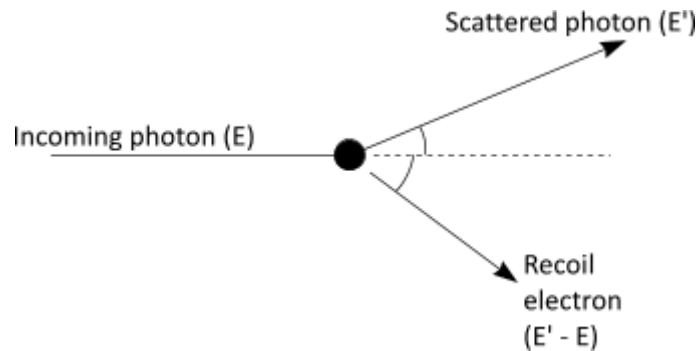


Figure-1.6: A diagram outlining the Compton scattering process

The energy deposited and the photon’s scattering angle are linked through equation-1.2 [1-15]:

$$E' = \frac{E}{1 + \frac{E}{mc^2}(1 - \cos\theta)} \quad (1.2)$$

$E$  is the incident gamma-ray energy,  $E'$  is the energy transferred to the electron and  $\theta$  is the scattering angle. This analysis is oversimplified in that the binding energy of the electron is neglected, which adds a narrow distribution around the scattering angle for any given energy.

Thirdly, a high energy ( $>1.022\text{MeV}$ ) gamma-ray may, in the presence of a nucleus, decay into an electron-positron pair, though this is very unlikely unless the gamma-ray energy is many MeV. The electron and positron then share equally the remaining energy ( $E_{\text{gamma}} - 1.022\text{MeV}$ ) and then interact with the material as described above.

The total probability of the above interactions depends on the electron density, and hence  $Z$ . Interactions between electrons and incident gamma-rays are essentially random, so a beam of parallel gamma-rays incident on a volume will have a flux that falls exponentially with penetration depth ( $t$ ). The range of gamma-rays is characterised by the “attenuation length”, defined to be the depth into a material where the incident gamma-ray flux has fallen by a factor of  $1/e$ . Equation-1.3 gives the exponential function:

$$I = I_0 e^{-\mu\rho t} \quad (1.3)$$

$t$  is the depth of penetration,  $I$  is the intensity,  $I_0$  the incident intensity where  $t=0$ ,  $\rho$  is the density in  $\text{g/cm}^3$  and  $\mu$  is the attenuation coefficient in  $\text{cm}^2/\text{g}$ . From this we can find that the attenuation length is  $\tau = 1/\mu\rho$ .

For this reason, dense scintillators comprised of high-Z elements are preferred since they have a greater attenuation coefficient and so are more sensitive, and a greater fraction of the gamma-ray interactions will be full-energy deposits by the photoelectric effect.

#### 1.4.2. Gamma Detection Using Scintillators

The detection of gamma-rays and X-rays and the measurement of their energies depend on these processes in that it is the energy deposited in the detector by excited electrons that is measured, and the photon energy is inferred from this. Each process contributes to the detector's "response function" which describes the probability distribution of energy deposits.

The energy deposited in each gamma-ray interaction is inferred from the number of photons collected during the resultant scintillation pulse, so by binning events into a histogram we can observe the interaction processes outlined above. The number of photons collected is the product of the gamma-ray energy deposit ( $E_\gamma$ ), scintillator light yield (LY), light collection efficiency (LCE) and photon detection efficiency (PDE). That is:

$$N_{ph} = E_\gamma \times LY \times LCE \times PDE \quad (1.4)$$

In the case of illumination by monoenergetic gamma-rays, the spectrum of energy deposits will contain a Gaussian peak of events where the full photon energy is deposited and a continuum of counts where Compton scattering occurred.

Figure – 1.7 shows a sample spectrum of monoenergetic gamma-rays of 662keV interacting with a NaI(Tl) scintillator (taken from [1-16]).

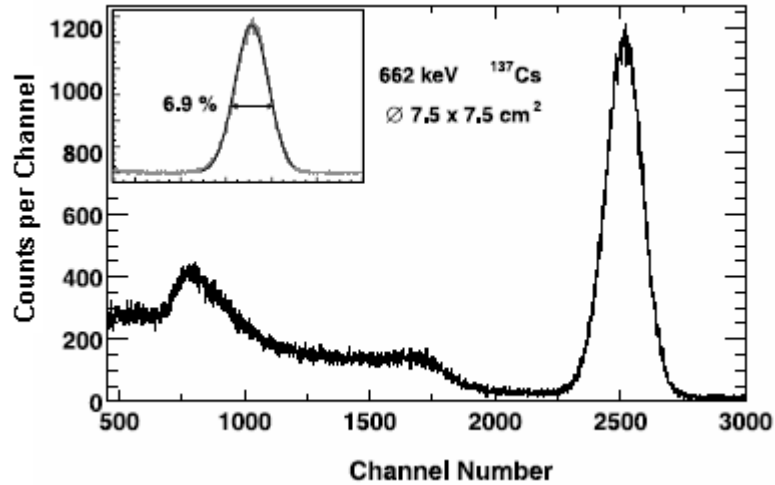


Figure – 1.7: A sample energy deposit spectrum. A 7.5cm cylindrical NaI(Tl) scintillator read out by a PMT was illuminated with gamma-rays from a Cs<sup>137</sup> source (taken from [1-16]). The inset shows a Gaussian fitted to the full-energy peak. The full width at half maximum (FWHM) of that Gaussian is shown to be 6.9%.

Note two major features in the response-function. Firstly, the peak around channel 2500 which represents full-energy deposits through either the photoelectric effect or multiple Compton scatters. Secondly, the continuum of partial energy deposits from Compton scattering. In cases where incident gamma-rays are not monoenergetic, a more complicated spectrum will be observed, a convolution of the detector response function and incident gamma-ray energy spectrum.

The quality of such spectra is characterised by the resolution of the full-energy peak, defined as the FWHM (Full Width at Half Maximum), and the noise floor. The noise floor is where small pulses from low energy gamma-ray interactions cannot be separated from noise in the pulse train, which may arise from the photosensor itself or associated electronics.

The energy resolution of scintillation spectrometers is determined by the variation in the number of photons collected, and the processes that cause it to vary. Energy resolution is given using the following formula:

$$R_T (1\sigma) = \sqrt{R_{stat}^2 + R_{VLE}^2 + R_{INT}^2 + R_{noise}^2} \quad (1.5)$$

Each term here quantifies a process that affects the number of photons collected for a given gamma-ray energy. As the terms are independent, they sum in quadrature.  $R_T(1\sigma)$  is the total

uncertainty in the number of photons counted ( $N_{ph}$ ). The full width at half maximum (FWHM) of the peak is given by equation 1.6:

$$R_{FWHM} = 2.35 \times \frac{R_T}{N_{ph}}. \quad (1.6)$$

$R_{stat}$  arises from photon statistics, specifically the number of optical photons captured by the photosensor. It depends upon scintillator brightness, LCE and detection efficiency of the photosensor, and is calculated as the square root of  $N_{ph}$ .

$R_{V_{LCE}}$  represents the uniformity of light collection efficiency over the volume of the crystal. Uniform LCE, where the number of photons detected is independent of location is essential to achieving good energy resolution. It is calculated as the mean deviation of  $N_{ph}$  from the mean depending on the location of the gamma-ray interaction.

$R_{INT}$  is the intrinsic variation of light output of the scintillator itself and is due to non-proportionality between gamma-ray energy and light output. As it is a property of the scintillator, it represents a fundamental limit on energy resolution.

$R_{noise}$  is the variation in the pulse height due to noise in the detector electronics or photosensor. The contribution of electronic noise may be reduced if the photosensor possesses intrinsic gain. A preamplifier such as the A250 from Amptek [1-17] has an r.m.s noise of 100 electrons and if the photosensor has unity gain (a PIN diode, for example) and collects 2000 photons, then  $R_{noise}$  would be  $\frac{100}{2000} = 5\%$ , a large contribution. However, an APD has a gain of 100, so this term falls to  $\frac{100}{200000} = 0.005\%$ . By the same argument, the noise term is also more significant at low gamma-ray energies where  $N_{ph}$  is low. Photosensor noise is greater in silicon devices than PMTs, and so limits their resolution, especially for large photosensor areas. For this reason, PIN diodes and APDs rarely have area greater than  $1\text{cm}^2$  and are best suited to applications that require small detectors.

### 1.4.3. Design of Gamma-Ray Spectrometers

Two design drivers must be balanced when designing a scintillation counter, the first of which is sensitivity. Sensitivity is important in security devices in order to detect sources efficiently and rapidly, to ensure that searches are quick and have a low chance of missing an illicit source. Sensitivity is also essential in medical applications, such as high energy X-ray imaging or PET, in order to reduce the dose received by the patient whilst the image is built up.

As previously stated, the attenuation length of gamma-rays is shorter in dense scintillators with high Z, where the electron density is high. Such scintillators will therefore be more likely

to stop, and therefore detect, gamma-rays for any given thickness. For this reason, BGO and LYSO are used in PET, as they both have a high density of greater than 7g/cc and so have short attenuation lengths.

Sensitivity also depends on scintillator size. The cross-sectional area that the scintillator presents to the source determines how many gamma-rays strike it. The thickness of the detector determines what fraction of incident gamma-rays interact and are detected, via Equation 1.2.

The second driver of scintillator design is the requirement to carry scintillation light efficiently and consistently from the interaction site to the photosensor. This is quantified as Light Collection Efficiency (LCE). It is important to most applications but critical to ones where gamma-ray spectroscopy is required to maximise counting statistics.

LCE is maximised by ensuring that as great a fraction of the scintillation light reaches the photosensor as possible. In doing this, it is important to remember that scintillators attenuate their own light to some degree, even though the attenuation length may be long. For example, CsI(Tl) has a self attenuation length of 1.8m [1-3]. Figure – 1.8 shows a scintillation event within a scintillator coupled by one face to a photosensor. Three light paths are shown for the three possible ways of reaching the photosensor. The space between the scintillator and reflective coating is exaggerated to show more clearly the two paths *b* and *c* which reflect from different surfaces.

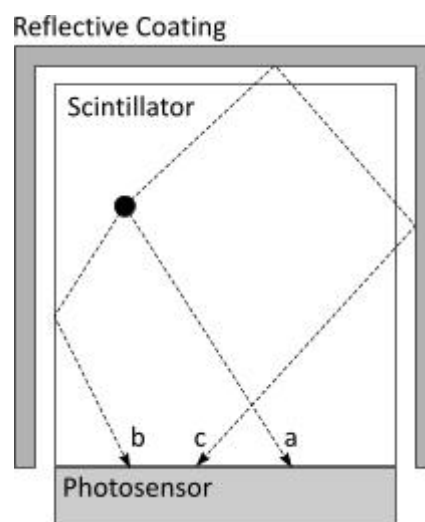


Figure 1.8: A sketch of the three possible paths taken by optical photons from the interaction side (black circle) to the photosensor.

Scintillation light is emitted isotropically from the interaction site, so only a fraction will be directly incident on the photodetector (Path a). The closer the interaction to the photosensor, the greater the solid angle subtended by it and the greater that fraction will be.

The remaining light will reach the surfaces of the scintillator and the fraction that is incident at angles greater than the critical angle (as given by  $\theta_{crit} = \arcsin(n_2/n_1)$ , where  $n_1$  and  $n_2$  are the refractive indexes of the media on either side of the interface) will undergo total internal reflection (Path b).

The fraction of light that escapes should also be reflected back into the scintillator to maximise LCE and improve photon statistics (Path c). This can be achieved by covering the surfaces in a reflective material so that the escaping photons are reflected back into the crystal. Reflectors may be divided into “specular” and “Lambertian” reflectors. As the name implies, when light is incident on the former, it is reflected at the same angle. A leading material for this is ESR (Enhanced Specular Reflector) [1-18] made by 3M, which is highly reflective with  $\epsilon \approx 99\%$ . In the case of Lambertian reflectors, the light is scattered randomly. A range of Lambertian reflectors exist, including the popular PTFE tape (chosen for convenience and cost) and densely packed white powders like MgO and AlO. Whilst packed powder offers excellent reflectivity ( $\epsilon > 98\%$ ), it is inconvenient to handle, so recent advances include solid materials like Spectralon [1-19] and GORE DRP [1-20], both of which are structures of PTFE. Spectralon is formed by sintering PTFE powder into a solid which then may be machined into the desired shape, whilst DRP is a micrometer-scale structure designed to achieve near fully Lambertian reflection.

The choice of reflecting material is a key part of optical design and depends on the desired performance and the crystal geometry. High reflectivity is essential in all cases, especially when multiple reflections are expected before the light will reach the photosensor. Equation 1.6 shows how multiple reflections of light will reduce the number of photons:

$$I = 1 - \epsilon^N \quad (1.7)$$

Where  $I$  is the number of photons,  $\epsilon$  is the reflectivity and  $N$  the number of reflections.

In practice, it is very difficult to have smooth surfaces to exploit total internal reflection, and gamma-ray spectrometers tend to have crystals with a low aspect ratio of up to 4:1 (length to width). Therefore, it is traditional to try to maximise LCE by relying on Lambertian reflection. Numerous studies have searched for the best way to do this, usually in the context of CsI(Tl) coupled to a PIN diode in order to reduce the floor imposed by thermal noise in the diode. Bird et al [1-21] is a good example, in that it covers changes to the crystal geometry such as tapers

and also which surfaces should be abraded to maximise Lambertian reflection and impede total internal reflection. Light collection efficiencies of up to 80% are typical for scintillators of a few cubic centimetres treated in this way.

This brief analysis is intended to show that a trade-off exists in scintillator design, where a large volume is desired to maximise sensitivity but a small volume is optimal for light collection efficiency. For this reason, large volume spectrometers, for example those used in vehicle scanning portals, tend to have poorer spectral performance than small spectrometers. The principles outlined here will be revisited over the course of this thesis when designing scintillator configurations for evaluating and applying SiPMs.

### **1.5. Photodetectors in Ionising Radiation Sensing with Scintillators**

Photodetectors sensitive to the optical photons emitted by scintillators are essential to gamma-ray sensing so understanding their characteristics is essential.

Spectroscopic applications place a number of demands on the photodetector. Ideally, photodetectors convert optical photons into electric pulses proportional to the number of optical photons detected, and thus the energy of the detected gamma-ray.

Another critical concern is photon detection efficiency, the probability of a photon incident on the sensitive surface being collected. Good detection efficiency is essential to detecting low energy events in which the number of photons produced in the scintillator is small and ensuring that these events can be seen above noise in the electrical signal. Good efficiency also improves the counting statistics so the statistical uncertainty ( $R_{\text{stat}}$ ) is reduced and the measurement of the gamma-ray energy deposit is made more accurate.

All electrical signals from photodetectors must be processed to infer the number of photons collected, and all electronics generates a certain quantity of noise. This noise adds a random component to such measurements, and can swamp the signal generated by low energy events where few photons are collected. Therefore, it is advantageous for photodetectors to provide gain to lift the signal above this noise.

By the same token, the photodetector should not generate noise of its own. Such noise differs from noise in the electronics, in that it takes the form of spurious photon counts and may be subject to the same gain as genuine photon counts.

### 1.5.1. Photomultiplier Tubes

The vacuum photomultiplier tube (PMT) is the oldest photosensor in use though it is still dominant in many applications. A PMT consists of a photocathode, a dynode chain and an anode, with potential differences of hundreds of volts between them (see Figure – 1.9 below). The photocathode (a) is made of a metallic material having a low work function to improve the probability of electrons being freed by incident photons. Mixes of alkali metals such as potassium are used for their low work function. Optical photons liberate electrons with little kinetic energy, in the range  $\sim 1\text{eV}$ . Guiding electrodes (b) and a strong electric field accelerate those electrons into the dynode chain (c), where impact ionisation is used to provide electron multiplication and therefore gain. In a ten-stage dynode chain, gain factors up to  $10^6$  are achieved. By measuring the current flowing through the anode (d), we can detect pulses proportional to the number of incident photons. The entire assembly is enclosed in glass (e) and evacuated to prevent the attenuation of electrons in air and to prevent the oxidation of the alkali photocathode. Figure – 1.9 shows a sketch of the PMT principle.

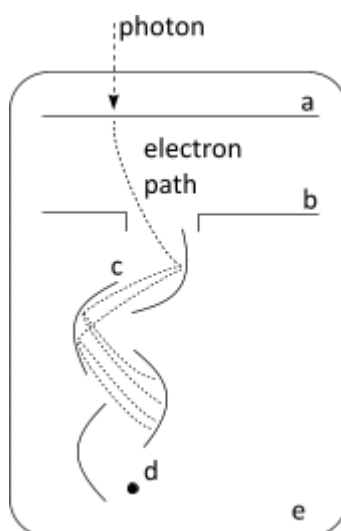


Figure – 1.9: A sketch of the PMT operating principle. Photoelectrons at the cathode are accelerated into the dynode chain where gain is applied. The labelled components are: a = photocathode, b = focussing electrodes, c = dynode chain, d = anode, e = glass vessel

The photon detection efficiency is limited compared to silicon photodiodes. A thick photocathode is needed to attenuate optical photons whilst a thin one is needed to permit extraction of the photoelectrons without them being attenuated by the photocathode again. The best detection efficiency, or Quantum Efficiency (QE) achieved at the time of print is 43% at 380nm [1-22], though a peak of 20-25% is common with standard bi-alkali photocathodes

[1-23]. Uniform collection of photoelectrons from the cathode can contribute to energy resolution, as can non-uniformity in photocathode thickness, though this is minimised by randomising the light coming from the scintillator and uniformity is good in modern PMTs.

High gain and low photocathode noise remain the principal advantages that allow PMT technology to scale well to large areas so they are suitable for reading out large scintillators, something that has not been replicated by solid-state photosensors. PMTs typically provide good energy resolution when combined with NaI(Tl) (6%-7% at 662keV) [1-16] and LaBr(Ce) (~3% at 662keV) [1-6], due to low noise and high gain; the latter removes the contribution of preamplifier noise to energy resolution. In the case of NaI(Tl), the statistical term ( $R_{stat}$ ) and the intrinsic resolution contribute roughly equally to energy resolution. Better resolution is achieved with LaBr(Ce) due to its higher light output and much lower intrinsic resolution.

PMTs have practical problems such as sensitivity to magnetic fields. Electrons in the dynode chain will only have energies of up to a hundred eV, up to the potential difference between dynodes, and so their trajectory can be affected by the geomagnetic field. They are fragile, which can complicate use in portable instruments and a magnetic shield is required. PMTs are also the largest and heaviest of the important photosensors, making them less suitable for smaller devices where space is more important, as a large fraction of the total detector volume is photomultiplier and not scintillator.

### 1.5.2. PIN Photodiodes

Silicon PIN diodes were the first photodiode to be used in gamma-ray spectroscopy and they have found use in applications where PMTs are unsuitable due to size and fragility. The use of a silicon diode allows for very good QE of up to 85% as photoelectrons do not have to be extracted from the light-capturing material, merely drifted through it to electrodes. However, they do not have an intrinsic gain so output signals are small enough to be comparable to preamplifier noise, limiting energy resolution and noise floor. PIN diodes have highest QE above 500nm and so are well suited to exploiting the high light output of CsI(Tl) (peaking at 550nm), and the CsI(Tl)-PIN detector is commonly used. Such a detector using a 1cc CsI(Tl) crystal and a 1cm<sup>2</sup> PIN diode can be expected to achieve an energy resolution of 7% at 662keV. In this case, the high QE has led to good photon statistics and the small crystal allows for uniform light collection due to short path length and the large solid angle of the PIN diode.

PIN diodes also have high dark noise due to thermal excitation of electrons in the depletion region, far higher than in a PMT. This noise scales with the volume of the depletion region, so for a given thickness it scales with area. PIN diodes also have high capacitance which scales

with area, typically 40pF for a 1cm<sup>2</sup> diode [1-24]. Such capacitance loads the preamplifier and generates noise. It is this noise that limits PIN diodes to small devices of a few square centimetres, as both energy resolution and noise floor (the lowest signal that may be detected above the photosensor noise) become worse with area. As an example, the combined noise contribution of amplifier and dark current in [1-25] was measured to be ~800 electrons (FWHM) compared to a signal of ~13000 photoelectrons from a 662keV gamma-ray, a contribution of 6.3% out of a measured resolution of 7.7%. PIN diodes are also susceptible to direct gamma-ray interactions, which can pollute spectra though these can be removed by pulse shape discrimination. The same technique has been demonstrated to be a way of circumventing the noise floor by using the diode to directly collect spectra of low energy (<100keV) gamma-rays whilst using light from a CsI(Tl) scintillator to collect spectra of higher energies [1-26].

PIN diodes have therefore found use in compact applications, or where PMTs are unsuitable. Applications include portable and space-borne instruments where size, weight and ruggedness are important and sensitivity to the geomagnetic field is problematic. However, low noise amplifiers must be used if high performance is required, driving up costs and power consumption. As a rule of thumb, the noise in an amplifier scales with the inverse of the current passing through it, so lower noise demands greater power. Photosensor noise is thermal in origin and so may be reduced by cooling the diode, though again this costs power and weight.

### **1.5.3. Avalanche Photodiodes**

The signal in a photodiode may be raised above electronic noise using an avalanche process that occurs in semiconductors at high bias voltages. Such an avalanche photodiode (APD) uses a proportional mode avalanche to achieve a gain of the order 10-100, greatly reducing the relative significance of preamplifier noise to improve both energy resolution and noise floor. For example, a 1cm<sup>2</sup> APD from Hamamatsu (S8664-1010N) achieved an energy resolution of 5% FWHM at 662keV and a noise floor of 10keV, at room temperature [1-27]. The same APD gives a comparatively modest gain of 50 at a bias voltage of 340V. Thermally excited electrons are also subject to the avalanche process so dark counts remain an issue, though the introduction of gain improves performance overall. This high performance is again limited to small detectors (a sensitive area of ~1cm<sup>2</sup>) by thermal noise, preventing avalanche photodiodes from competing with PMTs in many detectors. The use of APDs is complicated by random variations in the gain achieved in each avalanche, adding a noise term to the energy resolution.

Like PIN diodes, APDs have a thick depletion region so direct gamma-ray interactions may occur. The gain is very sensitive to bias voltage and thermal variations so a stable bias supply with some gain stabilisation mechanism is required in order to obtain the full benefit of gain and ensure good energy resolution.

### **1.6. Conclusion**

Now that the context of radiation sensing with scintillators has been set and the current common technologies have been outlined, attention can now move onto the focus of this thesis, the silicon photomultiplier (SiPM), a novel photosensor. In the next chapter, SiPM technology will be described and then considered in the context of radiation sensing with scintillators.

## 2. SiPMs in Radiation Sensing

In this chapter, SiPMs are described in terms of their operating principle and the characteristics that result from it. They are then critically compared to the photosensors already discussed in the context of gamma-ray sensing applications. Setting them in this context gives some guidance as to how they fit into the range of photosensors and on where their unique characteristics can be exploited.

SiPMs are marketed under several names such as MPPC (Multi Pixel Photon Counter); SSPM (Solid State Photon Counter); AMPD (Avalanche Micro-pixel PhotoDiode), depending on manufacturer. Terms such as SPAD (Single Photon Avalanche Diode) or G-APD (Geiger-mode Avalanche PhotoDiode) refer to the microcells that make up a SiPM. The term “SiPM” is used exclusively throughout this thesis for clarity.

### 2.1. Silicon Photomultiplier Operating Principle

A silicon photomultiplier is a novel solid state photosensor. Unlike PIN diodes or avalanche photodiodes (APD), a SiPM is not comprised of a monolithic device but an array of microscopic avalanche photodiodes, each operating in the Geiger mode to provide very high gain.

The principal difference between an APD and a SiPM photodiode is that the electric field across the depletion region is sufficiently strong that a Geiger-mode avalanche can take place, instead of a proportional-mode avalanche. During an avalanche in a semiconductor, electrons are accelerated to sufficiently high energy to create further electron-hole pairs through impact ionisation. In an APD, the electric field is low enough that each initial electron-hole pair will excite 50-100 further pairs, depending on bias voltage. This means that the charge output of the diode is proportional to the number of incident photons collected by the diode.

In a Geiger-mode avalanche, the electric field is much stronger so that *both* electrons and holes may excite further pairs which then go on to excite further pairs still until all of the charge stored in the diode is released, irrespective of the number of initial electron hole pairs, so that information is lost. A current may then freely flow through the diode, with moving electrons and holes exciting further pairs until the avalanche process is interrupted, or “quenched”. The threshold between the Geiger mode and the proportional mode used by APDs is normally expressed as the “breakdown voltage ( $V_b$ )” which is normally between 45 and 50V. The breakdown voltage is a function of diode thickness as it is an electric field threshold that must be achieved. During Geiger-mode avalanches, the gain is much higher, in the range of  $10^5 - 10^6$ .

Figure – 2.1 shows a typical SiPM photodiode and the electric field structure within as a function of depth (taken from [2-1] and [2-2]). Figure – 2.2 shows a microphotograph of a SiPM photodiode taken from [2-1].

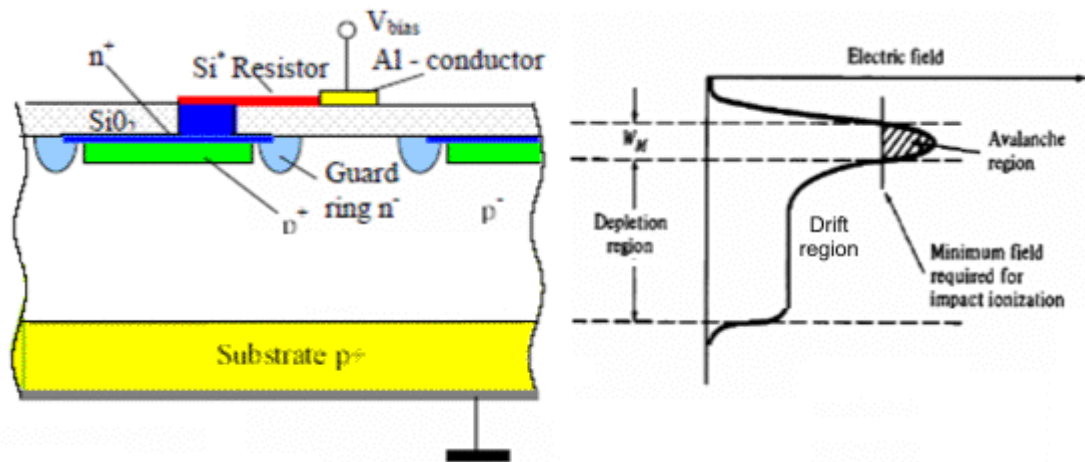


Figure-2.1: The structure of a typical SiPM microcell. The left-hand panel shows the photodiode structure and the right-hand panel shows the electric field structure when reversed biased above the breakdown voltage. When the diode is reverse biased, the electric field points down the page, towards the substrate. Photons are incident from above.

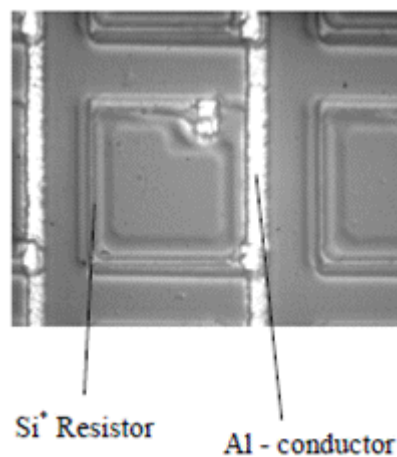


Figure-2.2: A microphotograph of the surface a SiPM photodiode. The Si resistor bounds the active diode area. The Al conductor is common to that strip of photodiodes in the array.

The SiPM structure has been arranged to produce an “avalanche region” between two strongly doped layers where the electric field is high enough for a Geiger mode avalanche to take place. The depletion region extends deeper into the diode through a lightly positively-doped layer. Within the depletion region is the “drift region”, which draws electrons towards the avalanche region.

An incident photon can excite an electron-hole pair at some point in the silicon, which will move through the drift region. Electrons travel up toward the n-junction, whilst holes travel down towards the substrate, and an avalanche may be triggered if one of them enters the avalanche region. This process has implications for photon detection efficiency that are explored in Section 2.2.3.

When an avalanche occurs, the photodiode can be thought of as a discharging capacitor and so the gain is limited by the capacitance of the cell and the overvoltage (defined to be the bias voltage minus the breakdown voltage). For a typical capacitance of 50fF and an overvoltage ( $V - V_B$ ) of 5V, the available charge in the cell is given by  $Q = C(V - V_B) = 5 \cdot 10^{-11} \times 5 = 2.5 \cdot 10^{-10} C$  equal to  $1.56 \times 10^6$  electrons. Therefore the gain in this “typical” case is  $1.6 \times 10^6$ .

A Geiger mode avalanche is self-sustaining and so a current will continually flow through the diode unless interrupted. The absorption of further photons in the diode will not affect the avalanche and so no further photons will be detected. Therefore, the avalanche must be “quenched” to allow further detection of photons. This is the purpose of the Si resistor in Figure – 2.1 which has a resistance in the range of  $\sim 1M\Omega$  and is in series with the diode. As the avalanche starts, the current increases causing a voltage drop across the resistor. When the reverse bias voltage across the diode falls below  $V_B$  the pair-creation rate decreases so the avalanche is no longer self-sustaining and stops. As the avalanche rate drops, so does the current, and the microcell returns to its initial state. This cyclic process is known as passive quenching and is used in all currently marketed SiPM designs. The current output of the diode now has a rise time of typically 1ns and a recovery time of 100ns, the latter being the product of diode capacitance and quenching resistance.

A lone Geiger-mode avalanche photodiode behaves as a binary device with no dynamic range. Therefore, a SiPM is created by arranging arrays of  $10^3$  of these photodiodes per square millimetre on the same substrate and electrically connecting them in parallel by depositing conducting electrodes onto the surface. The combined device now has a dynamic range, as dimmer flashes of light start the avalanche in only a few cells (“firing” is a common term) and brighter flashes would fire more cells, making an “analogue” device with discreet levels.

Note how in the photograph, the pn-junction bounded by the resistor represents only a small fraction of the total surface area. This fill-factor acts to reduce the effective photon detection efficiency of SiPMs relative to PIN diodes.

## **2.2. SiPM Characteristics**

Before comparing SiPMs with other photosensors and considering how they may be used in radiation sensing, it is necessary to understand their characteristics and behaviour, and how these arise from the operating principle.

### **2.2.1. Factors Affecting Gain**

Accurate gamma-ray spectroscopy requires a detector with a stable response, that is, the relationship between gamma-ray energy and pulse height, so the factors that determine and alter gain need to be understood before SiPMs can be used in practical instruments.

Gain depends on overvoltage and can therefore be varied by changing the bias voltage or breakdown voltage. Breakdown voltage varies with temperature, in that it falls as temperature increases. Therefore, for a given bias voltage, the gain can be seen to vary with temperature. For example, Buzhan in [2-1] found a variation in gain of 0.5% per 1K.

This is comparable to that found in a PMT, and this has implications on detector design. A SiPM-based detector will not remain calibrated after a change in temperature, so some correction will need to be applied to stabilise the gain.

Stabilisation may be achieved by exposing the SiPM to a known light flash, such as flashes of light from an LED coupled to the SiPM and scintillator, and adjusting the bias voltage such that this flash produces a pulse of consistent height. The flash will appear as a feature in the gamma-ray spectrum, and keeping the feature in the same MCA channel will ensure that the calibration remains stable.

### **2.2.2. Gain Uniformity**

Consistency of gain over the sensitive area is important in a photosensor. The effect of inconsistent gain is seen in PMTs, where photocathode non-uniformity is widely reported [2-3] and can contribute strongly to pulse height resolution. Such non-uniformity is due to variations in photocathode thickness, leading to variations in quantum efficiency; it may also be due to variations in the collection and acceleration of photoelectrons onto the first dynode.

Gain uniformity has been studied in SiPMs, both over the area of a microcell and also between microcells. An example may be seen in Figure – 2.3, taken from [2-4], which shows how uniform the gain is between cells in the first panel and how uniform the gain is over the area of one cell in the second.

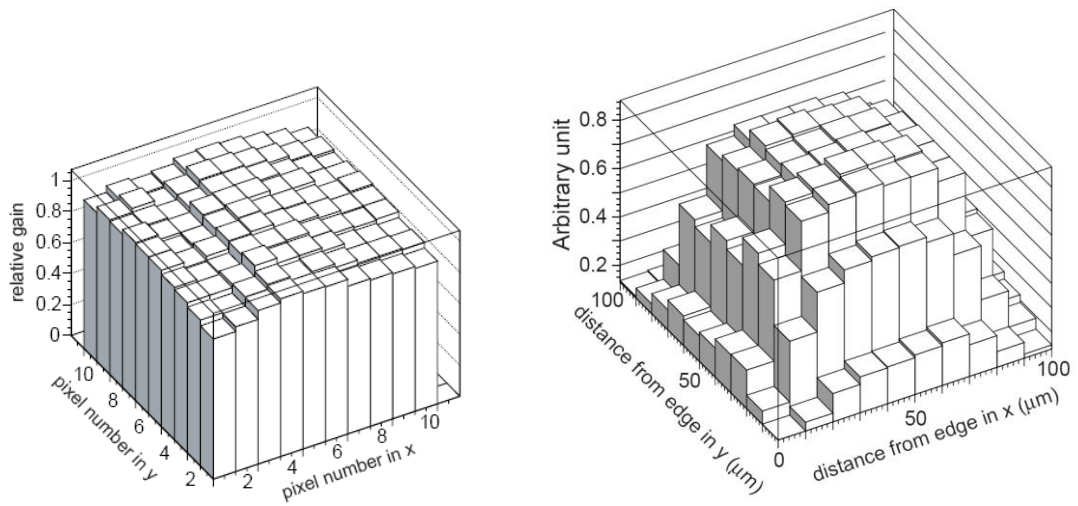


Figure 2.3: Plots of relative gain showing the uniformity of a Hamamatsu SiPM. The left hand panel is the gain of multiple pixels in a 10x10 array of photodiodes. The right hand plot shows the gain of a single microcell. Taken from [2-4].

This data was taken by scanning a narrow laser beam over the surface of a SiPM obtained from Hamamatsu having 100 microcells each 100 microns across. That is, the microcell pitch is 100 microns, which includes Al rails and empty space, which is why the gain rapidly falls off around the edges. Gain is shown in this case to be quite stable between microcells. Further evidence of good gain uniformity is the resolution of single-photon peaks. By exposing a SiPM to a weak pulsed light source, it is possible to build up a spectrum of pulses corresponding to 1, 2, 3 etc microcells fired. The resolution of these peaks will be limited by the gain uniformity. Figure – 2.4 shows such a spectrum taken from [2-5], using a SiPM manufactured by MEPHI (Moscow State Engineering Physics Institute).

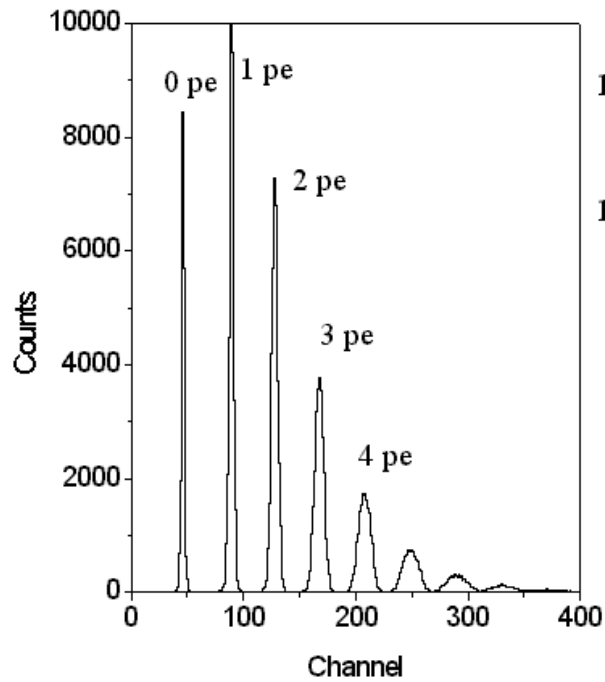


Figure-2.4: A plot showing the response of a SiPM to small numbers of photons, demonstrating the ability to count single photons.

SiPMs have been demonstrated to be accurate photon counters, at least for small numbers of photons and small arrays of diodes. As the number of microcells increases, the resolution of the single photon peak deteriorates due to pulse pile-up of dark counts from thermally excited electrons (See Section 2.2.4). From these good results, we can expect gain uniformity to make only a small contribution to measured energy resolutions.

### 2.2.3. Photon Detection Efficiency

Photon Detection Efficiency (PDE) is the fraction of incident photons that initiate avalanches. The term “quantum efficiency” (QE) is typically used when discussing PIN diodes, as it is the probability of incident photons being absorbed and exciting an electron-hole pair. Other processes are involved in a SiPM, such as the initiation of an avalanche, so other factors must be included and the more correct term is PDE.

Firstly, a “fill factor” must be included as the active diodes occupy only a fraction of the surface area and photoelectrons in the dead space between cells are lost (see Figure – 2.2). Fill factor may be improved by using shorter resistors with higher resistivity to allow the microcells to be packed more tightly, or by using larger microcells. For example, a Hamamatsu S10362-33 SiPM is available with cells of side 25, 50 or 100 microns giving fill factors of 30.8%, 61.5% and

78.5%, respectively [2-6], so this is an effective way of improving PDE. However, increasing microcell size decreases the microcell number, and therefore dynamic range, and increases non-linearity (See Section 2.2.5) so a trade-off exists.

Another factor is the Geiger efficiency: the probability that a charge carrier in the depletion region will trigger an avalanche. This is dependent on bias voltage: higher bias voltages accelerate charge carriers further thus increasing their average energy and the probability of impact ionisation. Piedmont presents a good discussion on this matter in Ref.[2-7]. PDE also has a dependence on photon wavelength, through interaction depth. Figure-2.5 shows a repeat of Figure-2.1. Again, the electric field goes down the page, so electrons drift up and holes drift down. Photons, the coloured dashed lines, are incident from the top of the page.

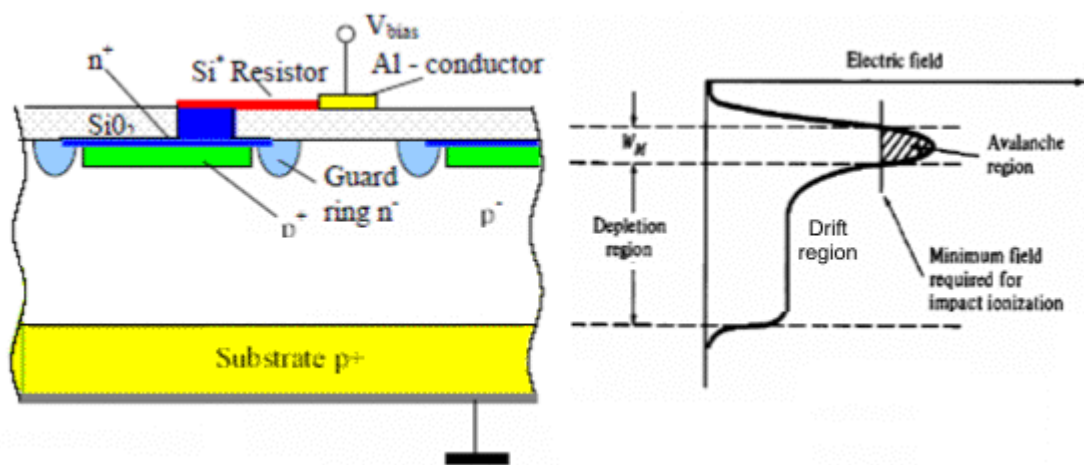


Figure – 2.5: A repeat of Figure – 2.1.

Short wavelength photons (~400nm) do not penetrate deeply into the silicon. Figure – 2.6 shows a plot of how transmitted light intensity falls off with penetration depth into silicon depending on wavelength, with the electric field structure overlaid on the same axis.

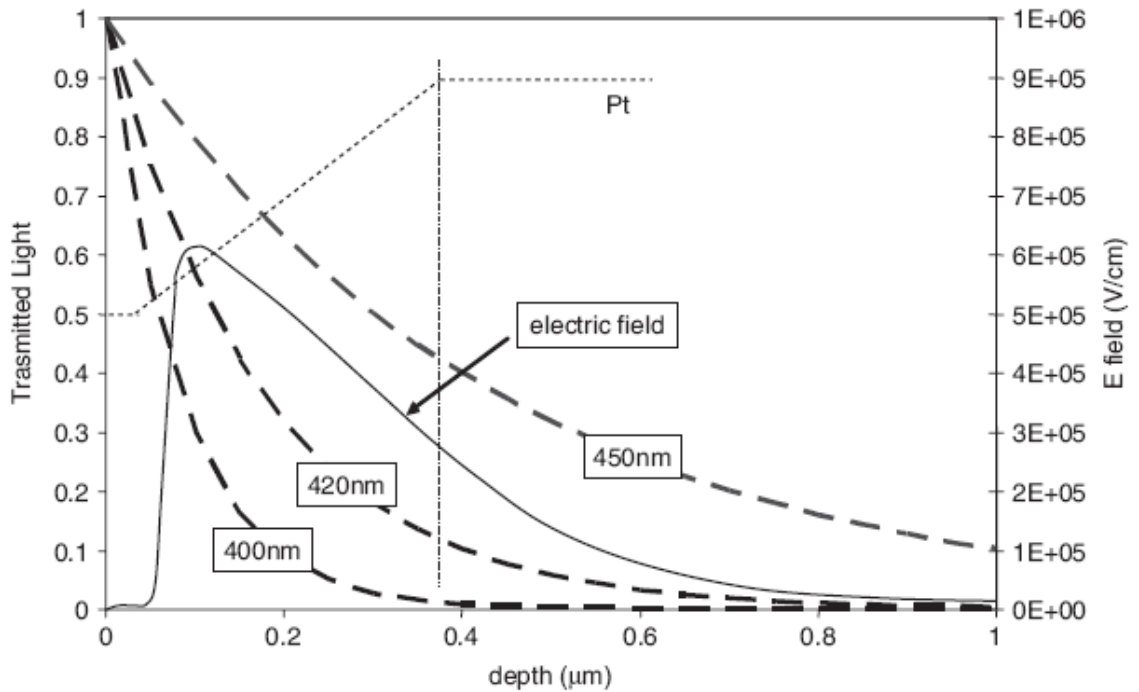


Figure – 2.6: A plot of how light transmission falls off with penetration depth. Also shown is the electric field structure of the SiPM (compare to Figure – 2.5). Finally, the line “Pt” shows the total Geiger probability of an electron-hole pair and how it varies with interaction depth.

Note the plateau starting at 0.37microns. Taken from Ref.[2-7].

Blue photons (400nm) have a greater probability of depositing an electron-hole pair in the dead region up to 0.05microns, instead of in the large drift region beneath, than red photons. In these cases, no avalanche will take place. In other cases, the electron-hole pair will be excited in the n-junction (depth = 0.75microns to 1micron), so the electron will drift away from the avalanche region directly into the electrode and so will not contribute to the avalanche. At the same time, the hole will pass through the avalanche region (the peak in the electric field curve) with a probability of triggering an avalanche. Whilst the hole might then be expected to have a high Geiger efficiency, holes have a high effective mass and so will not be accelerated as rapidly as electrons, hence the probability of impact ionisation is reduced. As the wavelength decreases, an extreme case would be the creation of most electron-hole pairs in the silicon oxide layer on the diode surface thus creating the low wavelength cut-off.

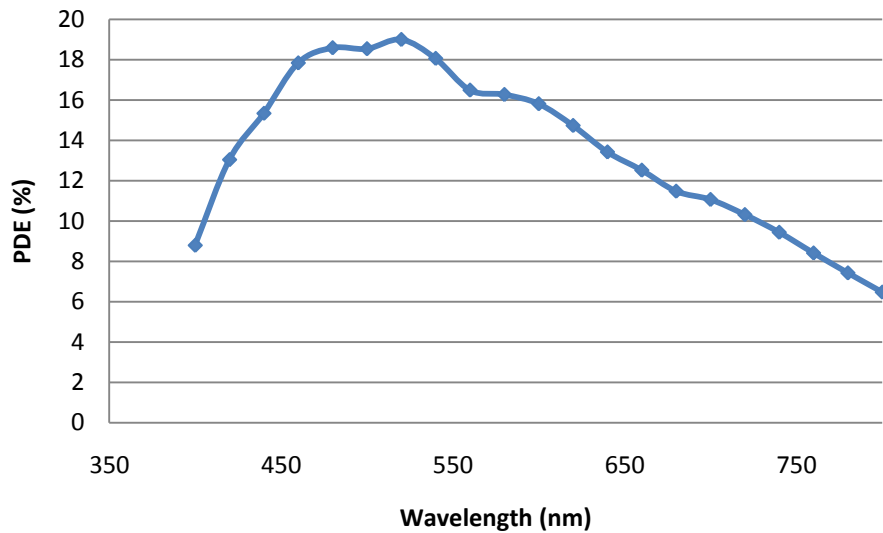
Red photons (~600nm) penetrate more deeply, so when illuminated by red light a greater fraction of the e-h pairs will be excited in the drift region beneath the diode, so that the electrons must pass through the high-field region, increasing Geiger probability. Longer

wavelengths up to the infrared range have a greater probability of passing through the diode entirely and interacting in the substrate, so the PDE slowly tails off as wavelength increases.

Combining the three terms, PDE can be written as:

$$PDE = QE \cdot FF \cdot GE(V_o, \lambda) \quad (2.1)$$

GE is the Geiger efficiency,  $V_o$  is the overvoltage, and  $\lambda$  is the photon wavelength. FF is the fill-factor, the fraction of the frontal area of the SiPM that is sensitive to photons. Figure – 2.7 shows how PDE varies with wavelength for a SensL 3035 SiPM with 35 micron microcells [2-8] as a typical example:



Figure–2.7: A plot of data provided by SensL for a 3035 SiPM showing how PDE varies with photon wavelength for a 2V overvoltage. Note the sharp fall off towards 400nm. This data is not available on the datasheet and was obtained from SensL directly via private communication.

Note how the peak PDE is slightly inferior to what may be achieved with a PMT with a bialkali photocathode [2-9], but much lower than the ~80% expected of a PIN diode [2-10].

It is possible to change the spectral response by inverting the diode, such that the p-junction lies on top. In this arrangement, the above argument would be reversed, with blue photons being captured closer to the p-junction, improving the Geiger efficiency for those electrons. This would improve the response to scintillators such as lanthanum bromide which has an emission peak at 380nm.

### 2.2.4. Dark Current

A significant dark current has been reported in SiPMs. Thermal excitation of electrons over the bandgap generating pulses is the main source of noise at a rate of  $\sim 1\text{MHz/mm}^2$  of SiPM area at room temperature and so may be reduced by cooling. Moser [2-11] reports that the dark current as a function of temperature is described by this equation:

$$I(T) = I(T_0) \frac{T^2 \exp\left(-\frac{E_g}{2kT}\right)}{T_0^2 \exp\left(-\frac{E_g}{2kT_0}\right)} \quad (1.2)$$

$E_g$  is the silicon bandgap,  $T$  is the temperature and  $T_0$  is a reference temperature. The dark current is proportional to the fraction of the Boltzmann distribution above the band gap for any given temperature, hence the presence of the exponential term.

Figure-2.8 shows noise rate varied with temperature and bias voltage (overvoltage is the key property in this case) in a Hamamatsu SiPM

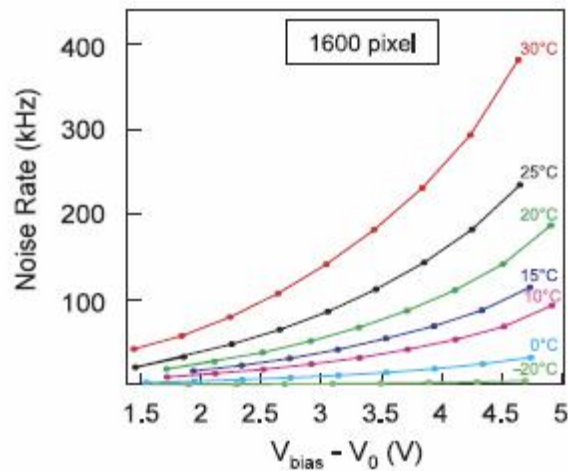


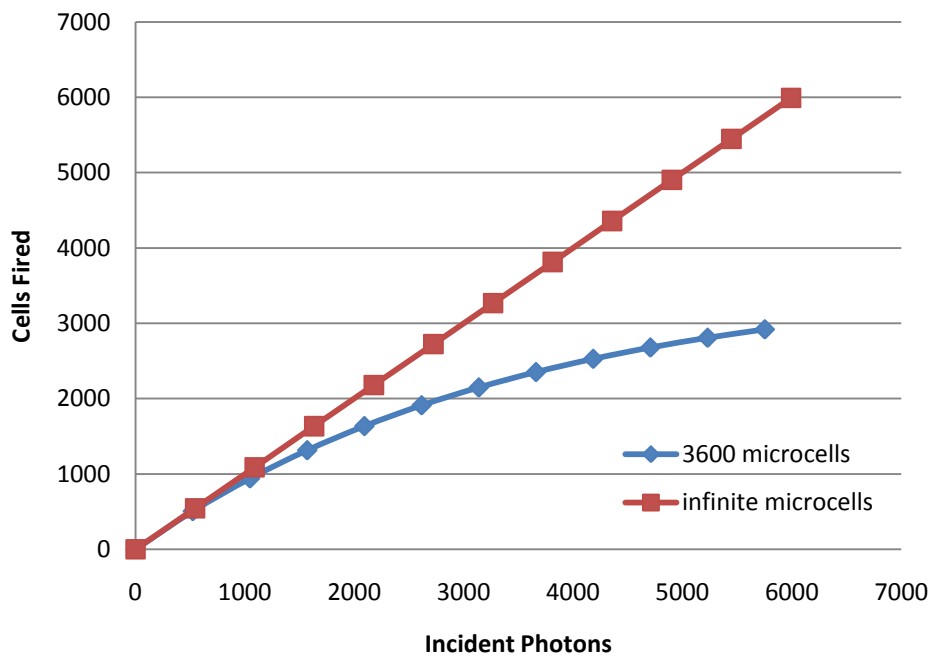
Figure-2.8: Data showing how dark noise varies with temperature taken using a  $1\text{mm}^2$  Hamamatsu MPPC (SiPM) operating at a range of bias voltages. (This image is taken from [2-12]).

For that SiPM, a modest cooling from  $20^\circ\text{C}$  to  $10^\circ\text{C}$  would be sufficient to halve the dark current from  $180\text{kHz}$  to  $90\text{kHz}$ . The dark count rate can be also reduced by reducing the operating voltage in order to reduce the Geiger probability but this would reduce PDE at the same rate.

### 2.2.5. Linearity and Dynamic Range

Linearity is the proportionality of the SiPM response to the number of incident photons. It is limited by the number of microcells on the SiPM due to the probability of more than one photon hitting a single cell during its recovery time and only one of those being detected. For scintillation flashes of more than one photon per pixel, the SiPM begins to saturate. In spectroscopic applications this limits the maximum detectable gamma-ray energy and also introduces a non-linearity between gamma-ray energy and SiPM signal. The dynamic range and linear portion of the dynamic range can be calculated using Poisson statistics by calculating the probability of any given microcell being struck by  $n$  photons, assuming uniform illumination of the SiPM.

Therefore, it is possible to calculate the number of microcells fired and the number of photons lost to saturation as a function of photon number, itself a function of gamma ray energy. This allows the response function (linearity curve) to be calculated. An example is shown below:



Figure–2.9: This figure shows the calculated response of a notional SiPM with 3600 microcells expressed as the number of microcells fired as a function of the number of incident photons.

In the plot above, the SiPM is assumed to be an array of 3600 microcells. It is assumed that the scintillator is very fast (time constant of less than 100ns) and so all of its light will be emitted during one microcell recovery time, resulting in the worst case scenario as far as

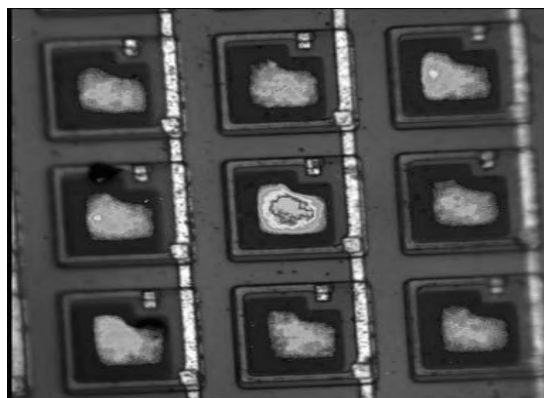
dynamic range is concerned. The blue line shows the number of cells fired and the red line the ideal linear response (simply the number of photons produced multiplied by the PDE which represents the ideal case where there are an infinite number of microcells). This curve has been obtained using Poisson statistics.

During longer pulses from slow scintillators like CsI(Tl) with decay times of a few microseconds, microcells that fire at the beginning of the pulse will have time to recover and fire again. The photon flux (photons/nanosecond) is also lower, so fewer microcells will be firing at any one given time. Therefore, when the pulse is long, the response of the SiPM is much more linear.

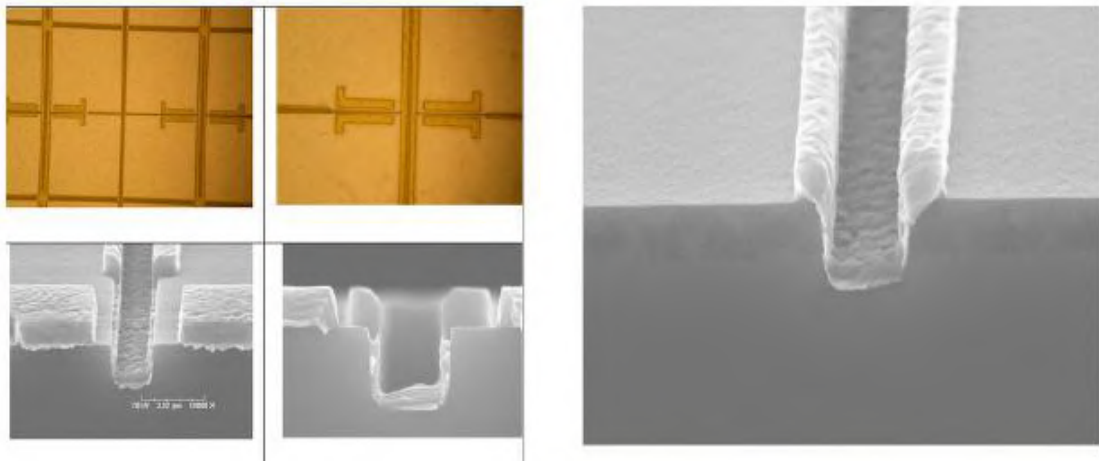
A tradeoff becomes apparent at this point. In order to increase the dynamic range of the detector, one must increase the number of cells. However, this introduces more dead space in a front illuminated SiPM and so reduces the PDE.

### 2.2.6. Optical Cross-talk

During the avalanche process in silicon, the recombination of electron-hole pairs either side of the depletion region emits infrared photons which may then propagate through the silicon and be absorbed in an adjacent microcell. If this occurs within the depletion region, an avalanche may be initiated; so called “cross-talk”. For every electron involved in a Geiger avalanche, there is a  $10^{-5}$  probability of an infrared photon escaping the cell [2-11]. Given that there are  $10^6$  electrons in each avalanche, tens of photons escape the cell. Figure – 2.10 shows a microphotograph of such light escaping from a Mephi SiPM, taken using a Hamamatsu Phemos 1000 emission microscope [2-13] collecting light over many seconds as the cells ignite spontaneously in dark counts. Figure–2.10 shows the emission spectrum of the avalanching silicon.



Figure–2.10: Optical photons escaping SiPM microcells. Taken from [2-11].



Figure–2.11: A series of microphotographs of trenches cut into the top surface of a SiPM to reduce crosstalk.

The problem may be reduced by the introduction of trenches between each cell as shown in Figure – 2.11, above. Trenches prevent photons from passing through the silicon directly into adjacent microcells.

Such measures are effective, reducing crosstalk probability to a few percent [2-14], although this depends on SiPM size, as larger arrays of microcells will be more likely to capture each other's emissions.

Cross-talk becomes more likely at higher overvoltage as the Geiger probability is increased; the same reason why PDE and dark current also increase with overvoltage. Cross-talk is troublesome since it adds another random element to the number of photons counted and so contributes a small amount to energy resolution in gamma-ray spectroscopy. More significantly, it complicates measurement of PDE. Ward and Vacheret [2-15] found that the combined effects of cross-talk and afterpulsing (below) increased PDE by 30%, when measured as photocurrent.

### 2.2.7. Afterpulsing

Afterpulsing is a phenomenon in which a single microcell pulse is rapidly followed by another despite a lack of optical photons. This has been attributed to charge carriers becoming trapped in imperfections in the silicon and then released causing a second avalanche [2-14]. Du et al [2-16] found that the afterpulsing probability reduced with time interval after the initial pulse, to be expected of a trapped state with a non-zero lifetime. Figure-2.12 shows the measured afterpulse probability as a function of time after the initial pulse, for a range of bias voltages.

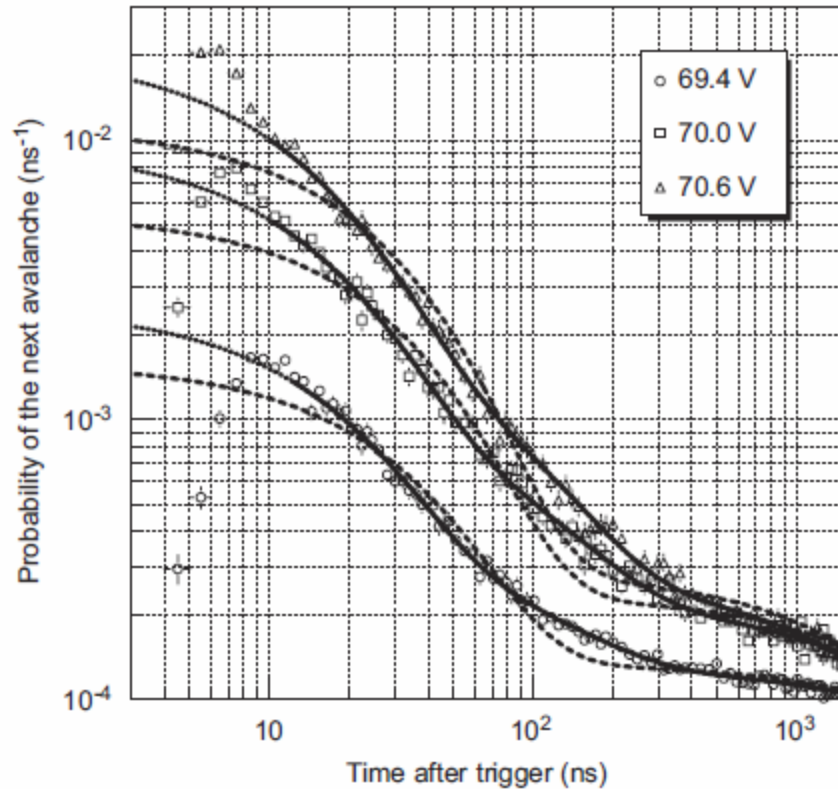


Figure-2.12: Time distributions of afterpulses for three bias voltages in a  $1\text{mm}^2$  Hamamatsu SiPM. (Taken from ref. [2-16]). The dotted and solid lines are attempts by the authors in ref [2-16] to simulate the afterpulsing process, with some success.

The solid and dashed lines represent attempts at calculated fits based on single and double time-constant exponential decays, respectively. A good fit was obtained, except below 10ns due to limitations of the test equipment, indicating that the afterpulsing process can be modelled the decay of a state with a finite lifetime. The time constant calculated here was  $92.7 \pm 5.8\text{ns}$ .

This generation of spurious counts is randomly occurring and therefore can contribute to inaccuracies in photon counting (energy resolution in spectroscopy) and can interfere with PDE measurements. For example, PDE may be calculated from measurements of photocurrent when exposed to a calibrated light source. In this case, afterpulsing and crosstalk will falsely increase the measured PDE [2-17]. This may be avoided by instead counting pulses at the single microcell level when the SiPM is exposed to weak laser light.

### **2.2.8. Radiation Hardness and Magnetic Field Insensitivity**

Performance of SiPMs can be adversely affected by doses of ionising radiation. A test carried out [2-18] involved 200MeV protons and found that SiPMs are slightly more sensitive to radiation damage than other silicon devices such as PIN diodes. Radiation damage affects performance by increasing dark count rate and gain non-uniformity. The dark count was found to increase by an order of magnitude after a 900 Rad dose of 200MeV protons. SiPMs are vulnerable to radiation damage due to their complex structures and trails of ionisation left by heavy particles cause imperfections in the silicon, introducing changes in the depletion region and thus the gain. These imperfections also increase the probability of tunnelling through the band gap and so the dark rate increases.

SiPMs have been found to be resistant to gamma ray damage by Blazey et al [2-19] who exposed a SiPM to 1 MRad of gamma rays and measured no change in SiPM behaviour.

Unlike PMTs, SiPMs are known to be insensitive to magnetic fields, in that their gain does not appear to vary in field of up to 7T [2-20]. SiPMs are also mechanically robust in that they are resistant to vibration and as long as they are not directly damaged. This is due to their basic nature, in that their operational process (the Geiger-mode avalanche) takes place on microscopic scales in a very strong electric field meaning that physical movement does not affect the avalanche. At present, no data is available to quantify their mechanical robustness. However, they are vulnerable to direct damage in the form of scratches across the surface which can occur during manufacture. The complexity and density of the basic SiPM structure is responsible for this.

### **2.2.9. An Alternative SiPM Design: Back-Illuminated SiPMs**

The alternative to the above front illuminated design is the back illuminated SiPM or avalanche drift diode (ADD) such as those developed in ref. [2-21] for use in calorimetry experiments. In this design, the pn junctions are mounted onto the substrate with the weak p layer on top with a shared resistor and electrical contacts. This means that the drift region (where the electric field is lower) is shared and each "pixel" is simply the high field avalanche region surrounding each junction. Around each diode are some positively doped rings which shape the electric field to guide drifting electrons towards the diode, similar in role to the guide electrodes in PMTs. Figure – 2.13 shows a diagram of how a back-illuminted SiPM could be arranged:

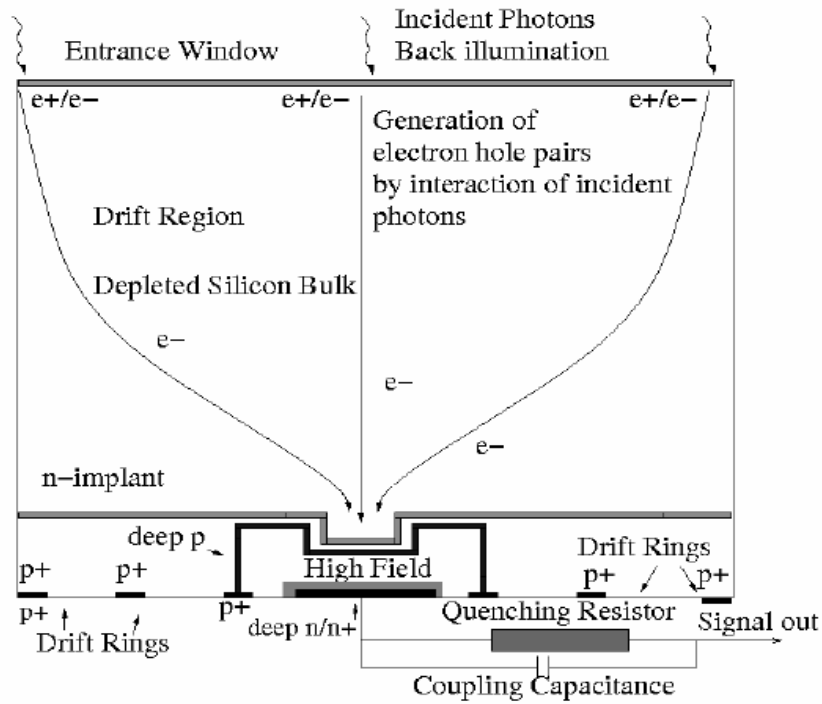


Figure-2.13: A diagram of a back-illuminated SiPM taken from [2-21]. Note how the avalanche regions are now in one volume of silicon and not separated in microcells so less surface area is wasted.

In this SiPM design, the photons (incident from the top of the page) are captured in the depleted silicon bulk in front of the avalanche region. The photoelectrons then drift through the low electric field in the bulk towards the avalanche regions, where the avalanche takes place. The holes all drift to the top of the diode.

This method allows for a greater PDE as the quenching resistors are no longer on the front face of the device and the drift region is shared. This gives a geometric fill of ~90%, dramatically improving the PDE. The PDE is also more consistent over the wavelength range 350 to 1000nm because all photons will interact in the drift region in front of the diodes, irrespective of wavelength. This removes the sharp cut-off in PDE below ~420nm where photons interact at the top surface of the SiPM so that holes are used to initiate the avalanche, not electrons. In a back-illuminated SiPM, blue photons will create electron-hole pairs near the entrance window whilst red photons will create them deeper. In both cases, the electrons will drift towards the avalanche region equally. Therefore, regardless of photon wavelength, only electrons will be used to initiate avalanches, exploiting their lower effective mass and higher Geiger probability.

However, the gain is only 1% of that of the front illuminated SiPMs due to a smaller cell capacitance. Also, the continuous depletion region and densely packed avalanche regions may

also allow a greater crosstalk probability as no trenches exist between them. Back-illumination has been used in CCDs for some time to improve performance, though it increases the unit cost and the wafers are typically thinner and more fragile.

### 2.3. Comparison of SiPMs With Other Photosensors

Now that the characteristics of SiPMs have been reviewed, it is natural at this point to compare them critically to current established photosensors. Such a comparison will allow an assessment of where SiPMs could have an impact in radiation sensing applications. In most applications, especially within gamma-ray sensing, the PMT is the favoured solution due to having by far the lowest noise per unit sensitive area. This makes it the only viable option for applications where a photosensor greater than a few square centimetres is required, such as gamma-ray spectroscopy or large Cerenkov counters.

A PMT is, however, very susceptible to magnetic fields and vibration and there are some cases where photodiodes are preferred. Such applications include gamma-ray telescopes such as INTEGRAL where  $1\text{cm}^2$  PIN diodes are used to read out CsI(Tl) crystals. This combination is chosen for robustness, compact size and low weight, which are key concerns in spacecraft. This choice was also permitted because energy resolution was not considered essential and imaging was to be done in the energy range 100keV and upwards, so the high noise floor in PIN diodes was not a concern. Table – 2.1 lists key advantages and disadvantages of SiPMs:

Advantages	Disadvantages
<ul style="list-style-type: none"> <li>• High gain (<math>10^6</math>)</li> <li>• Single photo counting ability</li> <li>• Fast response</li> <li>• Good timing resolution</li> <li>• Mechanically robust</li> <li>• Compact and light</li> <li>• Magnetic immunity up to 4T (at least)</li> </ul>	<ul style="list-style-type: none"> <li>• High noise</li> <li>• Lower PDE than PIN diodes and APD (20% max)</li> <li>• Small sensitive area (<math>\sim 1\text{cm}^2</math>)</li> <li>• Afterpulsing and crosstalk can complicate single photon counting</li> </ul>

Table-2.1: Advantages and Disadvantages of SiPMs in Gamma-ray sensing

It can be seen from the table that SiPMs are something of a hybrid in that they offer advantages from both PMTs and photodiodes whilst offering a similar mix of disadvantages. For example, they combine the high gain and low QE of a PMT with the small size and high noise of a PIN diode.

SiPMs are unlikely to take over from PMTs in the majority of gamma-ray detection applications, due to the size limit imposed by their high noise. Thus they will compete with PIN diodes and APDs for niche applications where compactness and robustness are important.

## 2.4. Potential Interest in SiPMs in Gamma-Ray Sensing

There are a number of fields within gamma-ray sensing where SiPMs could be of interest. The one that has generated the most interest is Positron Emission Tomography (PET), where detector elements could be constructed from a SiPM and LYSO or BGO scintillators. Current PET systems use small scintillators with a footprint of 3x3mm or 5x5mm read out by arrays of photodiodes or single position-sensitive PMTs (PS-PMT). SiPMs may be of use as direct replacements for the photodiodes, exploiting their high gain to reduce the cost of the electronics required, which can be high as PET systems comprise of many hundreds of elements. They are also more compact and simpler to use than PS-PMTs. Reasonable spectroscopic performance has been achieved with SiPMs and LYSO to date, exploiting the high light output and speed of LYSO [2-22] [2-23].

SiPM are of interest in gamma-ray spectroscopy as they have the potential to replace PIN diodes and APDs by virtue of their higher gain and low operating voltage. However, spectroscopic performance may be limited by poor PDE, though the removal of a significant noise term (through gain) may mitigate this. As SiPMs are small ( $\sim 1\text{cm}^2$ ), they are of interest only in small instruments such as handheld spectrometers or imaging applications such as gamma-ray telescopes or PET. Imaging systems typically rely on multiple small sensors, and SiPMs may be of interest, as their high gain allows for good performance with cheap amplifiers whilst being very compact.

Performance of gamma-ray sensors using SiPMs will be determined largely by the match between the scintillator and SiPM. Therefore, selection of the scintillator will be critical.

Table-2.2 shows the key properties of a range of common scintillators [2-24], [2-25], [2-26], [2-27], [2-28], [2-29], [2-30] :

	<b>Density</b>	<b>Yield</b>	<b>Peak emission</b>	<b>Peak PDE</b>	<b>Time constant</b>
	g/cc	ph/MeV	nm	%	ns
NaI(Tl)	3.7	38000	420	13	230
CsI(Tl)	4.5	52000	550	18	1000
CsI(Na)	4.5	41000	415	13	600
LYSO	7.4	32000	420	13	40
BGO	7.1	8500	480	18	300
LaBr(Ce)	5.1	63000	380	3	16
LiI(Eu)	4.08	11000	470	18	1500
EJ-200	1.02	10000	425	13	4

Table – 2.2: A comparison of typical scintillators in the context of use with SiPMs. This is mostly a reminder of Table-1.1, but with the inclusion of the PDE of a SensL 3035 SiPM at the emission peak of each scintillator.

We can expect SiPMs to perform well with scintillators that output in the SiPM sensitive range of around 450-500nm, such as CsI(Tl) or LiI(Eu). Due to SiPM noise, we can also expect fast scintillators such as LYSO to be favoured. Actual performance will depend on the interplay of these properties. SiPMs fit more naturally with small gamma-ray detectors as their size is limited by noise in the same manner as PIN diodes.

The potential impact of SiPMs on gamma-ray sensing will be the focus of much of this thesis, with tests being carried out on a range of scintillator-SiPM combinations in terms of spectroscopy, PET and others.

Chapter 3 experimentally investigates how SiPMs may be used with scintillators to create useful instruments for a range of applications such as medical imaging or gamma-ray astronomy. Chapter 4 develops a gamma-ray sensor further to develop a useful spectrometer for handheld instruments.

## **2.5. Conclusion**

It has been found that SiPMs are to be considered as an alternative to APDs or PIN diodes in the majority of applications and that they should be considered more as a high-gain APD than a PMT due to their high noise.

The potential for SiPM use in radiation sensing has been outlined, so the following chapters will investigate this in detail. Chapter 3 details how SiPMs may be used with scintillators in a general sense, and Chapter 4 builds on those results to create a spectrometer of useful volume for use in handheld instruments. Chapter 5 explores how SiPMs may be used to build a useful compact neutron detector. Finally, Chapter 6 explores a novel instrument based on high-performance SiPMs in order to understand what may be achievable as SiPMs improve in the future.

### 3. Evaluation of SiPMs with Small Scintillators

Having discussed the operating principle of SiPMs and how they can be expected to behave, this chapter explores how they may be applied in radiation sensing.

SiPMs were evaluated for use in radiation sensing using a range of scintillators, to establish which scintillator-SiPM combinations may be of interest. Both single devices and tiled arrays of SiPMs were tested in order to explore how well SiPM technology scales to sensitive areas up to 2cm<sup>2</sup>. During these studies, a range of applications were identified where SiPMs offer sufficiently good performance or specific advantages to be competitive with existing systems.

This chapter concludes with a discussion of potential methods for overcoming the limitations of SiPM-based radiation sensors as determined in this chapter.

#### 3.1. Testing Single SiPMs using Small Crystals

In these measurements, single SiPMs were tested in order to begin evaluation of SiPMs with the simplest sensor possible. The radiation sensors described in this section are of interest both in their own right and as stepping stones towards larger sensors, achieved by tiling SiPMs into arrays of 4, 9 and 16. Evaluation of SiPM performance is based on the key parameters of energy resolution achieved using SiPMs and the minimum gamma-ray energy resolvable above noise.

Energy resolution is a key parameter in many gamma-ray sensing applications. It is essential for gamma-ray spectrometers intended to identify isotopes as it allows spectral lines to be resolved from each other. Isotope identification is used in geophysics, archaeology for radiodating, and security. In the latter case, it is used to distinguish potentially threatening sources from natural sources in order to prevent false alarms which can impede the flow of commerce through a port or border. Gamma-ray astronomy also requires spectrometers with good energy resolution to understand high-energy processes in the universe. Well resolved energy information can also be used in personal dosimetry to obtain more accurate measurements of absorbed dose.

At this stage, it is important to understand how the processes that determine energy resolution work in the context of SiPMs. Predictions of energy resolution in SiPM-based systems are calculated using the following formula:

$$R_T (1\sigma) = \sqrt{R_{stat}^2 + R_{VLE}^2 + R_{INT}^2 + R_{DR}^2} \quad (3.1)$$

Each term is expressed in or microcells fired (or pulse height) during the scintillation pulse.

- $R_{\text{stat}}$  expresses the variation in pulse height due to counting statistics. When counting multiple events of  $N$  photons, a Gaussian distribution is observed with standard deviation  $\sqrt{N}$ . It depends upon scintillator brightness, LCE and PDE.
- $R_{\text{VLC E}}$  refers to variations in LCE over the volume of the crystal and may be predicted using optical Monte Carlo simulations of the crystal in question. It is calculated as the mean deviation of  $N_{\text{ph}}$  from the mean depending on the location of the gamma-ray interaction. Minimising the variation in LCE over the scintillator volume is a key part of scintillator design.
- $R_{\text{INT}}$  is the intrinsic variation of light output of the scintillator. This is due to the non-proportionality inherent in all scintillators between photoelectron energy and light yield. A gamma-ray may deposit its full energy in multiple interactions, giving rise to a number of electrons which will scintillate with a different light yield. The random nature of this process contributes a statistical variation in the total light yield, summed over the multiple interactions.
- $R_{\text{DR}}$  is the variation in the number of dark counts collected during the integration period. This term is calculated to be the square root of the mean number of dark counts expected during a scintillation pulse, given as the product of noise rate and the integration time.

Since these terms are independent, a quadratic sum is used to produce an estimate of the total resolution. The full width at half maximum (FWHM) of the peak is given by:  $R_{\text{FWHM}} = 2.35 \times \frac{R_T}{N_{\text{ph}}}$ .

Note how there is no term to describe the contribution of preamplifier noise, unlike in PIN diodes. SiPMs offer sufficiently high gain that electronic noise in the electronics is small enough to be negligible. Instead, the contribution due to dark counts takes its place as they occur at random and so may be integrated into the pulse.

There is also no term to describe noise due to variations in gain, like those seen in PMTs (photocathode non-uniformity) or APDs. This is due to the excellent gain uniformity and single photon counting ability demonstrated in Figure – 2.4.

The second parameter in the evaluation is the noise floor, defined to be the minimum gamma-ray energy detectable above the noise in the detector. “Noise” refers to unwanted signal generated by the detector electronics or photosensor. As previously stated, this is dominated by dark counts from the SiPM itself, not detector electronics.

The noise floor is determined by the noise rate in the SiPM, and scales linearly with sensitive area. It is also determined by the light yield and LCE of the scintillator, and the PDE of the SiPM, that is, the number of photons collected as a function of gamma-ray energy deposit.

It is clear that photon statistics,  $N_{ph}$ , is essential to spectrometer performance as it plays a role in determining energy resolution and noise floor.

### 3.1.1. Equipment and Preliminary Tests

For this work, the 3035X13 SiPM from SensL was used. This possessed microcells of dimension 35 microns arrayed in a square active area of side 2.85mm in a total package of 9mm<sup>2</sup>. The cell size allows for 3640 microcells and a fill factor of 60%, leading to a peak PDE of 19% at 520nm at an overvoltage of 2V. At the same overvoltage, a noise rate of 1MHz/mm<sup>2</sup> at 20°C is quoted. This refers to the average rate of single microcell firings triggered by thermal excitation. Figure-3.1 shows the PDE as a function of wavelength at 2V overvoltage.

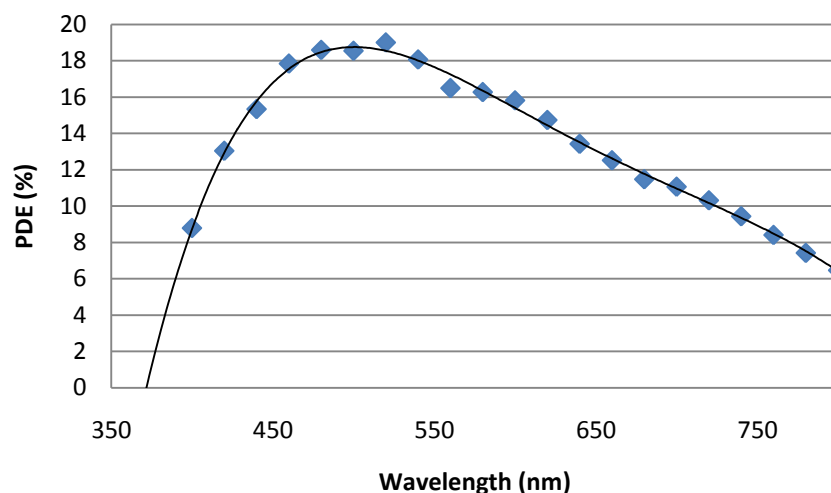


Figure-3.1: Photon detection efficiency as a function of wavelength. The data provided by SensL stops at 400nm, so a trendline is extended into the shorter wavelengths. This is the data shown in Figure – 2.7.

The curve shown here is as expected from the analysis in section 2.3.2, being more sensitive to green light, and so we can expect these SiPMs to be better suited to scintillators with greater output in this region such as CsI(Tl) [3-1], which peaks at 550nm. There is also a plastic

scintillator available with a peak wavelength of 490nm (EJ-260) [3-2], although this has roughly 20% of the light yield of CsI(Tl) at 10000 ph/MeV compared to 52000 ph/MeV.

The SiPM tested here was packaged bare, that is, with no front covering and bonded by its back onto a brass T08 holder, as show here in Figure–3.2.



Figure-3.2: A photograph of a SensL 3035 SiPM set into a T08 can with a CsI(Tl) and a LSO crystal, both wrapped in PTFE.

Total Area	mm <sup>2</sup>	9
Active Area	mm <sup>2</sup>	8.1
Peak PDE	%	18.5
Noise Rate	MHz/mm <sup>2</sup>	1
Microcell side	nm	35
No. microcells		3640
Breakdown voltage	V	27.2

Table–3.1: Properties of the SensL 3035 SiPMs used in this study.

For the initial tests, it was decided to use LSO and CsI(Tl) crystals. This is because LSO and CsI(Tl) have very different scintillation characteristics in that CsI(Tl) is bright with a long pulse whilst LSO is dimmer with a fast pulse, so the interplay between photon number and pulse length can be explored. For example, LSO has half the light yield of CsI(Tl) but the pulse is 20 times shorter, leading to a greater photon intensity. These scintillators were also chosen as LSO is not hygroscopic at all whilst CsI(Tl) is only slightly so, to the point where it may be handled but will degrade slowly in air, removing the need for encapsulation which is impractical at this size. Table–3.2 shows the key properties of the scintillators used. Both crystals were wrapped in PTFE to achieve uniform diffuse reflectivity.

	<b>LSO</b>	<b>CsI(Tl)</b>
Yield (ph/MeV)	26000	52000
Time constant (ns)	40	1000
Peak (nm)	420	550
PDE at peak (%)	13	18
Density (g/cc)	7.4	4.5

Table-3.2: The key properties of LSO and CsI(Tl), the scintillators chosen for the initial evaluation of SiPMs.

A 9mm<sup>2</sup> SiPM was coupled to two crystals of 2x2x15mm, using silicone optical grease (BC-630). The cross section of 2x2mm was chosen to ensure that all photons fall on the 2.85x2.85mm active area of the SiPM. It was decided to use a long crystal to match those used in PET (see below) and for convenience when wrapping in PTFE.

SensL provided a preamplifier in the form of a trans-impedance amplifier (Type no. SPMA4) which provided bias and shaped the SiPM pulses into Gaussians of FWHM 250ns. In order to collect all charge, the preamp signal was passed to a simple integrator.

The integrator is an important component as it allows counting of the total number of photons captured over the entire scintillation pulse, instead of merely the peak number. During a CsI(Tl) pulse, which is longer than the SiPM microcell cycle time, the photons emitted by the scintillator will be spread over several microseconds. Thus, it is the area of the SiPM output pulse, not the peak height, which gives the number of photons captured. Therefore, an integrator is used to convert area into pulse height, and it is this pulse height that is binned into the spectrum.

In the case of LSO, the entire light flash will take place within the 250ns preamp shaping time so an integration time of 400ns was used to collect the entire pulse without collecting excessive noise. The decay of CsI(Tl) has two components with time constants 1 $\mu$ s and 3 $\mu$ s leading to a very long pulse so these pulses were integrated with an integration time constant of 2.2 $\mu$ s to collect all of each pulse.

A multichannel analyser (MCA) from AmpTek (an MCA800A) [3-3] was used to bin the pulse train into a pulse height spectrum.

### 3.1.2. Measurements Using CsI(Tl) and LSO

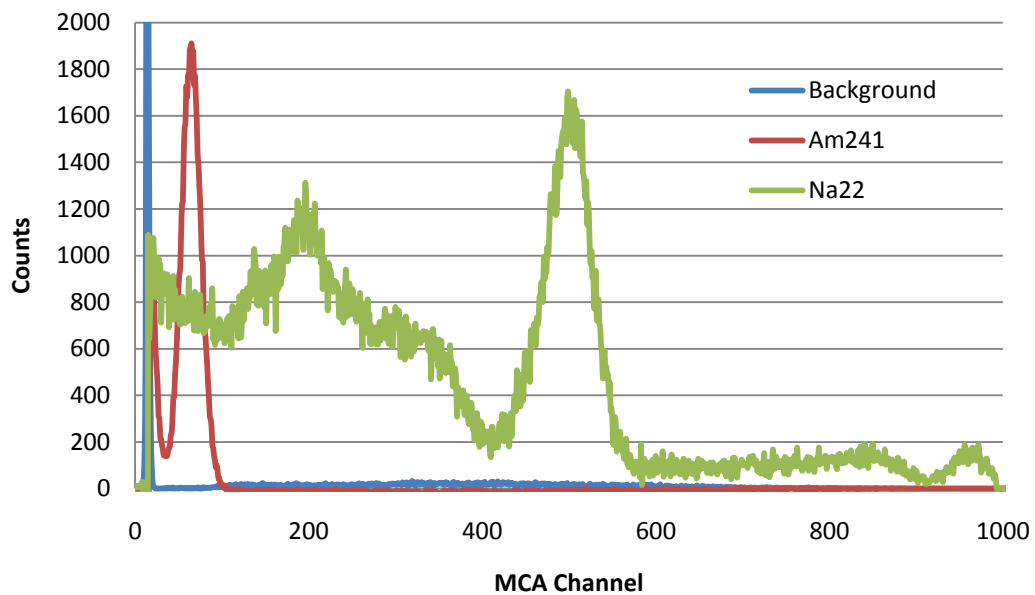
Performance was measured in terms of energy resolution and ‘noise floor’, defined as the channel where noise generated 1cps (taken from a background spectrum), expressed as the equivalent gamma-ray energy based on a known energy peak. That is:

$$NF = \frac{662keV}{PH} \times NL \quad (3.2)$$

Where  $NF$  is the noise floor in keV,  $PH$  is the pulse height of the 662keV photopeak in MCA channels, and  $NL$  is the noise level (at 1cps) in channels. Energy resolution was defined as the FWHM ( $2.35\sigma$ ) of a photopeak.

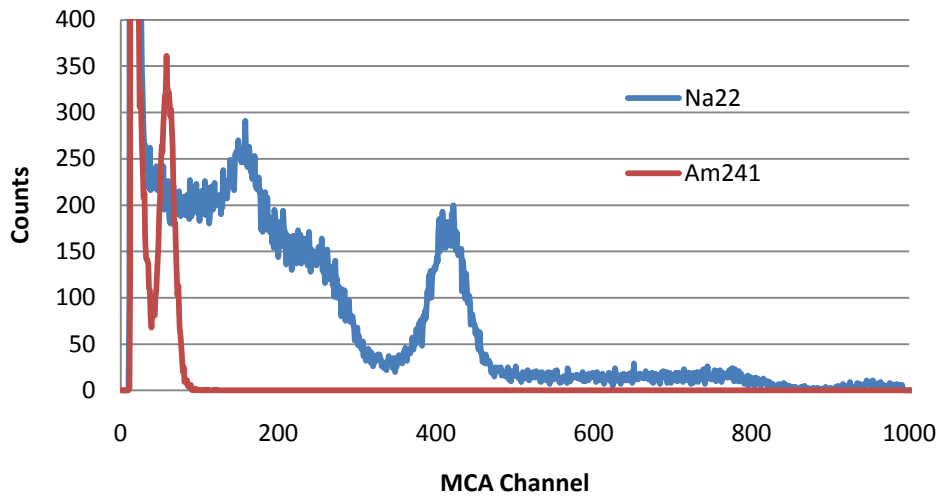
Figure–3.3 shows the spectra obtained using LSO in the upper panel and with CsI(Tl) in the lower panel. Table–3.3 shows the resolutions and noise floors achieved with the two scintillators. LSO contains a fraction of radioactive  $Lu^{176}$  and so a strong background continuum is observed which is removed from the spectra above by background subtraction [3-4].

#### LSO Crystal 2x2x15mm



Figure–3.3 (panel 1): Spectra obtained with a single SiPM with LSO and CsI(Tl). Note how the 511keV photopeak stands higher above the Compton continuum in the LSO spectrum, due to the higher atomic mass and density.

## CsI(Tl) Crystal 2x2x15mm



Figure–3.3 (panel 2): Spectra obtained with a single SiPM with LSO and CsI(Tl).

LSO:

Energy	Peak	FWHM	Noise Floor	
			ch	keV
keV	ch	%	ch	keV
32 (Cs <sup>137</sup> )	31	52	16	17
59 (Am <sup>241</sup> )	64	39	16	15
511 (Na <sup>22</sup> )	497	11	16	16
662 (Cs <sup>137</sup> )	634	9	16	17
1274 (Na <sup>22</sup> )	960	3	16	21

CsI(Tl):

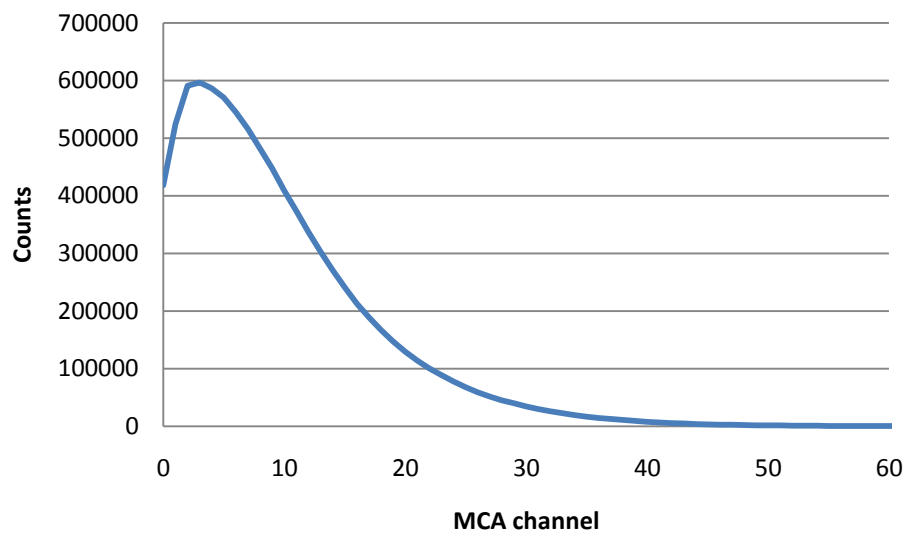
Energy	Peak	FWHM	Noise Floor	
			ch	keV
keV	ch	%	ch	keV
32 (Cs <sup>137</sup> )	31	35	23	24
59 (Am <sup>241</sup> )	58	29	23	23
511 (Na <sup>22</sup> )	416	9	23	28
662 (Cs <sup>137</sup> )	533	9	23	29
1274 (Na <sup>22</sup> )	958	4	23	31

Table–3.3: Noise floors and resolutions taken from the spectra above. The upper panel is LSO and the lower is CsI(Tl).

CsI(Tl) has the better resolution of the two, especially at low energy, whilst LSO has the better noise floor. CsI(Tl) has a more proportional response at low energies and so the intrinsic term is reduced at low energies relative to LSO. CsI(Tl) is also brighter than LSO and has a better spectral match, leading to improved photon statistics. The low noise floor achieved with LSO is due to it having a shorter pulse and so less noise is collected in the integrator.

LSO has an internal radiation source, so background subtraction is frequently needed to be able to clearly see the intended spectrum. However, due to the very small volume of the crystal used here (0.06cc), the internal background was so small that subtraction was not needed. Note the low, wide feature in the background spectrum in the LSO panel in Figure – 3.3 and how few counts it contains relative to the Na<sup>22</sup> spectrum taken over the same time interval.

LSO was expected to have a much lower noise floor than CsI(Tl) due to a shorter integration time constant of 400ns compared to 2200ns, and this is found to be true. Figure–3.4 shows the measured noise for a 2.2μs integration time window (used with CsI(Tl)). The noise peak is half a Gaussian curtailed by a threshold.



Figure–3.4: The measured dark noise continuum of a SensL 3035 with an integration time constant of 2.2μs.

The energy resolution achieved with each scintillator was predicted based on the data in Table–3.1 and Table–3.2, and Monte Carlo simulations of the scintillator’s optical behaviour. Note that the intrinsic term is omitted as it is difficult to estimate reliably, it is expected that the predictions will therefore be optimistic.

### **3.1.3. Notes on Geant4 Optical Monte Carlo**

Optical simulations are carried out several times throughout this thesis, so now is a good point to outline the technique in some detail. The software used was Geant 4.8.2, available from CERN, where it was developed. Geant 4 is a C++ implementation of Monte Carlo simulations of the interactions of radiation with matter. It has played a role in the development of portable radiation detectors, space-borne gamma-ray observatories and high-energy physics experiments.

Monte Carlo techniques use repeated sampling of the simulated processes to generate their results, using a series of random numbers. Monte Carlo techniques are especially useful where a result cannot be calculated analytically within a reasonable time frame. In radiation applications, there are a lot of random processes, such as the direction of 511keV annihilation photons, the energy deposit of a gamma-ray in Compton scattering, or the angle of reflection of photons off a roughened surface. Geant uses known processes and distributions to calculate a result, by taking a sum of the results of a large number of independent events.

For example, in these optical simulations we wish to build a detector, like the one shown in Figure – 1.8 (page 17), and determine the LCE, that is, the fraction of photons that reaches the photosensor. There are a great number of photons being reflected by a number of diffuse (Lambertian) reflecting surfaces, introducing random elements to the situation. Moreover, the photons themselves are emitted from the scintillation event isotropically. Geant handles this situation by considering each photon individually, randomly selecting an initial direction for it. Ray tracing is used to track the photon and determine what volume (if any) it will enter next, and the appropriate processes applied. For instance, if the next volume is also transparent, then the Fresnel equations can be used to calculate the angle of refraction. If the interface is an opaque reflecting material, then the photon is reflected. This process (tracking and calculating) is repeated until the photon is absorbed.

The processes of refraction and reflection are already contained within Geant, and have not been interfered with during this study. To define a detector, we must define the materials by stating key properties: the refractive index and attenuation length. We then define some volumes of these materials and then place them to build the detector. The key part is the

definition of “surfaces”, where the volumes meet. If the surface is reflective, then we must state its reflectivity (the fraction of photons reflected at the surface, not absorbed or transmitted) it is and what fraction of reflection is specular or diffuse (Lambertian). It is these numbers that are used by Geant when invoking the reflection processes when a photon is incident on a surface. If the surface is not, and the two volumes are transparent, then Geant uses the Fresnel equations to handle refraction and absorption.

#### 3.1.4. Simulations and Predictions of Energy Resolution

Optical Monte Carlo simulations, as described above, were carried out to predict the optical behaviour of the scintillation crystal. This is quantified as Light Collection Efficiency (LCE), the fraction of scintillation light that reaches the photosensor. LCE is needed to calculate  $N_{ph}$  and so  $R_{stat}$  and is essential to energy resolution. The second parameter to be simulated is the Variation in LCE (VLCE) which represents the uniformity of LCE over the volume of the crystal.

The quality of optical simulations is determined largely by how the reflecting surfaces are defined. In this case it was assumed that diffuse (Lambertian) reflection would dominate due to the use of PTFE as the wrapping material. Therefore, the detector was defined as a volume of scintillator (CsI(Tl) or LSO) of 2x2x15mm abutted at the end and side faces by a diffuse reflecting material with reflectivity  $\epsilon=98\%$ , that is, 98% of incident light from the crystal would undergo Lambertian reflection, and the remained 2% would be absorbed. The remaining face was coupled to a volume representing the photosensor, and it was assumed that all light incident on this face would be absorbed. During the simulation, it is the number of photons absorbed in this way that was counted. It was assumed that scintillation light is emitted isotropically from the interaction site, where the gamma-ray deposited its energy.

Gamma-rays interact all over the scintillator, and the LCE will vary with location. For example, fewer photons will escape the scintillator if they are emitted at the far end. The LCE of the scintillator as a whole will be an average of the LCE over the whole volume. VLCE is the standard deviation of the distribution of LCE with volume.

To calculate LCE and VLCE we must simulate how LCE varies with the location of this isotropic photon source. Therefore, the simulation was run multiple times with the photon source in a different location. It is important that each location represents an equal fraction of the total volume to ensure even weighting. This generated a distribution of LCE values, which was averaged to gain the LCE (and  $N_{ph}$ ) and the average deviation from the mean gave VLCE.

Simulating the LSO crystal described above predicted a LCE of  $46 \pm 13\%$ . This gave a VLCE of  $13/46 = 28\%$  (at  $1\sigma$ ).

Table–3.4 shows the predicted resolution at 662keV for both CsI(Tl) and LSO based on the data in Tables-3.1 and 3.2 and a simulated LCE of  $46 \pm 13\%$ . Each term is expressed in terms of photons collected by the SiPM and as a percentage of the number of photons collected in the entire scintillation event.

	$N_{ph}$	$R_{stat}$	$R_{DR}$	$R_{VLCE}$	$R_T$	<b>FWHM</b>
	Ph	ph	ph	ph	ph	%
CsI(Tl)	2534	50	7	716	718	67
LSO	1267	36	2	358	360	67

Table-3.4: The predicted resolution of a 2x2x15mm scintillator coupled to a 3035 SiPM, for both LSO and CsI(Tl)

The very poor predicted resolution of 67% is dominated by the VLCE term due to the strong predicted non-uniformity along the length of the crystals. Note that CsI(Tl) has a better  $R_{stat}$  term due to being a brighter scintillator. The total predicted resolution is very poor, and it is expected that measured values will be better.

Comparing this prediction to the data above, the total energy resolution was badly overestimated. In the predictions above, the VLCE term dominates the resolution, due to the roll-off along the length of these high aspect-ratio crystals. The reason for this big discrepancy is of interest and is believed to be the assumption in the simulation that all reflection is Lambertian in nature due to the use of PTFE. This would be true if the crystal surface were abraded and so randomly scratched, as is typical in shorter crystals. Abrading the surface encourages Lambertian reflection and prevents total internal reflection by randomising the surface. However, the surface of both crystals is polished so a significant portion of the light will undergo total internal reflection, so the VLCE is in fact reduced. To account for this, the optical Monte Carlo simulations were adjusted and repeated. The simulation was improved by introducing a thin (0.1mm) air gap between the scintillator and the PTFE. This allows for total internal reflection at the scintillator-air interface, and Lambertian reflection at the air-PTFE interface. The improved simulation of a CsI(Tl) scintillator gave an LCE of  $69 \pm 2\%$ , so a VLCE term of 4% ( $1\sigma$ ). Repeating the above calculations (Table–3.3) gives an energy resolution of 8% at 662keV, closer to the measured value. It is likely, therefore, that much of the reflection in a long polished crystal like these is due to total internal reflection and that this is the reason for the inaccuracy of the initial energy-resolution predictions. This lesson will be important when studying other crystal configurations.

### 3.1.5. Linearity and Scintillator Proportionality

Non-linearity in the energy response was measured for both scintillators by taking the ratio of the channel numbers of the 1274keV and 511keV peaks. The true ratio is 2.49. With LSO we get  $\frac{960}{497} = 1.93$  and with CsI(Tl) we get  $\frac{958}{416} = 2.30$ . A strong non-linearity can be observed with both scintillators, due to the small number of microcells compared to the number of photons collected by the SiPM and the non-proportionality of the scintillator itself.

The non-proportionality of CsI(Tl) is well explored [3-5], [3-6] and it has been found that the light yield in this range (100- 1000keV) falls slowly with increasing gamma-ray energy. Syntfeld-Kazuch [3-6] reports that the light output at 1200keV will be 97% that at 511keV. Therefore, the non-proportionality of CsI(Tl) is a minor contributor to the non-linearity observed, so the greater contributor must be the SiPM.

When using CsI(Tl) the 511keV photopeak will contain 3828 photons (including PDE) compared to 3640 microcells in the SensL 3035 SiPM. However, CsI(Tl) has a long decay time compared to the SiPM cycle time, so any given microcell may fire multiple times over the course of the pulse, reducing the number of photons lost to double counting.

In contrast, all of the LSO pulse occurs within one microcell cycle time, so all the photons must be collected at once so the photon flux is higher. This will give a LSO-SiPM detector a less linear response, though the non-proportionality of LSO must be considered [3-6]. Whilst LSO has poor proportionality in the range 10-100keV, where the light yield at 10keV is 55% that at 100keV, the response in the range 100-1000keV is better. The light yield at 1000keV is ~95% that at 511keV. Again, the contribution of the SiPM to total non-linearity must be greater.

Given that both scintillators are rather linear in this energy range, the measurements taken here demonstrate that the linearity of a SiPM-based spectrometer depends strongly on the decay time of the scintillator, as the LSO-SiPM detector was less linear than the CsI(Tl)-SiPM detector despite the fact that CsI(Tl) is brighter. The longer pulse and so lower rate of photon incidence on the SiPM reduced the probability of photons being lost. In terms of finding how SiPMs fit into the field of radiation sensing and what applications they may be suited for, this finding implies that SiPMs provide the best spectroscopic performance with CsI(Tl). This bias towards CsI(Tl) may become less significant as SiPMs increase in size, so that the number of microcells increases and linearity improves.

### **3.2. Potential Applications of Single SiPMs**

Single SiPMs coupled to small LSO and CsI(Tl) crystals have been measured for performance but in order to judge how useful they may be, they should be considered in the context of specific applications.

#### **3.2.1. Positron Emission Tomography**

PET (Positron Emission Tomography) is a medical imaging technique that exploits the emission of two colinear 511keV gamma-rays from positron annihilation to locate a positron source in the body. A ring of gamma-ray sensors around the body is used to detect the coincident 511keV gamma-rays and therefore locate the source. The spatial resolution of this location technique is ultimately limited by the range of a positron in the body (a few millimetres) but is also determined by the size of the detector elements. Therefore, many small elements a few millimetres across need to be densely packed and a great deal of effort has been expended to develop systems to carry light from scintillators to photodetectors such as position sensitive PMTs [3-7].

This application has specific requirements of the scintillators used and therefore the photodetectors used to read them out. To reduce the dose absorbed by the patient the detector ring should be as sensitive as possible, so elements should be long with minimal gaps between them. Popular choices are BGO and LSO for their high density and stopping power. As the system relies on the coincident detection of two 511keV gamma-rays to build up a source density map, background counts may be rejected if they do not occur in two elements at once.

The image may be blurred by one or both of the 511keV gamma-rays scattering within the body before reaching the detector ring. In this case, the true source position will not lie on the line defined by the two detector elements. Reasonably good energy resolution is required to overcome this problem by allowing the scattered gamma-ray to be rejected based on energy.

High density and high Z are also useful as a high stopping power decreases the probability of one of the 511keV pair being missed (passing through the detector without interacting) and a genuine count being rejected. LSO and BGO have this high stopping power, but their high Z also gives them a high photo-fraction, so many of the 511keV gamma-rays will deposit their full energy. This is useful, as only full-energy deposits are used in image reconstruction to prevent scattering from blurring the image (see above). High stopping power and high photo-fraction therefore reduce the dose given to the patient by making the PET technique more efficient.

Therefore, PET favours fast, bright and dense scintillators with popular choices being BGO and LSO, although brightness is sacrificed for density in BGO. The crystals should also be densely packed so readout must be achieved with very compact devices.

SiPMs have some natural advantages that make them interesting, such as their small size. Unlike PMT, very little space is required for the photodetector itself. PET systems clearly require large numbers of detector elements so the electronics for processing pulses from each element should be as simple, compact and as cheap as possible.

SiPMs are useful in this respect, compared to PIN diodes, as their high gain allows for cheap and simple electronics to be used; a key concern when many thousands of detectors are present in the system. As they may be manufactured *en masse* by CMOS techniques, they also have the potential to be cheaper than PS-PMTs. It has been demonstrated here that SiPMs may achieve good energy resolution with LSO at 11% at 511keV, comparable to what may be achieved with a PMT [3-8] [3-9], and roughly comparable to other studies of SiPMs in a PET system such as reference [3-10] which achieved 9% at 511keV, though with a 4x4x5 mm crystal, which can be expected to have a smaller VLCE along its length. It is, however, an improvement over earlier studies which used 1mm<sup>2</sup> SiPMs with a poor PDE of 2.5% at 420nm [3-11]; this reflects the rapid improvement in SiPMs over the last few years.

Timing resolution is also important in PET as it can be used to determine time-of-flight. This information can tell us where on the line the source is placed, improving resolution. Although it has not been studied here, it has been covered elsewhere and a study by Otte et al [3-12] achieved a timing resolution of 3ns using SiPM, sufficient for PET.

### **3.2.2. Personal Dosimetry**

Personal dosimeters are used in all radioactive industries and their design varies depending upon the expected dose. In applications where only weak sources (~100kBq) can be expected to be present, a simple piece of photographic paper encased in plastic is used, worn like a badge and familiar everywhere. The expected dose is so low that readings are taken every three months. In applications where a stronger dose can be expected in a shorter time period, such as the nuclear power industry, three-monthly reading will be too late, so a paging dosimeter is required.

Any sensor for a paging dosimeter needs to be compact, light and require little power. Low voltage operation is helpful from the perspectives of safety and complexity.

A small SiPM coupled to CsI(Tl) may be useful in a paging dosimeter for its size and undemanding power requirements (~30V). The energy resolution and noise floor achieved here is good enough to allow the received dose to be calculated more accurately for gamma-rays above 25keV. LSO is not so suitable for this role due to its non-linearity. This will require some means of analysing the spectrum of pulses coming from the SiPM so this accuracy will be traded off against complexity over a simple current mode measurement of a silicon diode, a common method of dosimetry.

### **3.2.3. Summary of Work on Single 3x3mm SiPMs**

Combining a single SiPM with a LSO crystal of 2x2x15mm wrapped in PTFE has provided a potentially useful PET element with an energy resolution of 11% at 511keV. Tiled arrays of SiPMs can be used to read out an array of crystals in a module which can easily be butted up to others to create a PET imager. The PET module described in [3-13] uses the Anger camera concept with a tiled array, in an alternative design capable of very good spatial resolution (~0.6mm), and exploits the SiPM advantages of size and, potentially, cost.

A single SiPM coupled to CsI(Tl) has also been shown to be useful in a small detector for use in a spectroscopic dosimeter, providing basic spectral information on the gamma-ray environment in order to adjust the absorbed dose. However, the sensitivity of the device is very limited and scaling is difficult without impinging on LCE and therefore spectral performance, without using tiled arrays of SiPMs to increase sensitive area.

Comparing LSO to CsI(Tl) gave useful insight into how a SiPM can be expected to behave depending upon the speed and brightness of the scintillator to which it is coupled. This understanding is useful to further detector design based on SiPMs and is worthy of further exploration with a greater range of scintillators.

### **3.3. Tiled Arrays of Silicon Photomultipliers**

Coupling a single SiPM to a small LSO crystal has demonstrated the potential use of SiPMs in PET. At the same time, a useful spectroscopic dosimeter using CsI(Tl) has been tested and found to have good energy resolution. The performance of these devices raises questions as to how well they may be scaled up into small spectrometers or imaging elements so there is interest in exploring what can be done with larger SiPMs. As no manufacturer produces larger monolithic SiPMs than 3x3mm at the time of print, the concept of tiled arrays was explored.

### 3.3.1. Construction of Tiled Arrays

SensL originally produced tiled arrays in two ways. Firstly, by bonding the front faces of the SiPMs, where the electrical contacts are, to a glass slide. This is done by depositing gold tracks and then bonding the SiPMs onto them. The slight gap between the SiPM face and the slide is filled with a low viscosity epoxy to provide the bond and a good optical connection. By this method, SiPMs can be densely packed and a pitch of 0.3mm is achieved in this way. This corresponds to a total area of 196mm<sup>2</sup> for an active area of 144mm<sup>2</sup>, and a fill factor of 73%. Therefore we can expect the PDE of a tiled array to be reduced by this factor.

This method had the advantage of speed to SensL as it did not require new SiPMs to be developed with electrical contacts on the back. However, light must pass through the glass slide and the introduction of an extra interface between the slide and the crystal will have implications for LCE.

When tiling SiPMs with a common bias, they must have the same breakdown voltage. Gain is strongly dependent on overvoltage so a variation in breakdown voltage between SiPMs in an array will degrade resolution in a manner analogous to photocathode non-uniformity in a PMT.

Tiled arrays may have either individual readout so each SiPM can be addressed, or summed readout where the array behaves as one monolithic device.

Tiled arrays of both types were used in these experiments. Array #1 was a 16-element array of 9mm<sup>2</sup> 3035X13 (SensL Array2) [3-14] constructed by bump bonding onto a glass slide. The total area including pitch was 196mm<sup>2</sup> with an active area of 144mm<sup>2</sup>. Array #1 had 16 identical preamplifiers on one board, giving the option of individual or summed readout. Each preamplifier operated in the trans-impedance mode and was identical to the preamplifier used with single SiPMs. This array was used to test the variation in SiPM characteristics within an array and how this may affect performance.

Array #2 had 9- elements of the same SiPMs, connected in parallel on the glass slide to permit summed readout only. This array was also constructed by bump bonding onto a glass slide with the same pitch as Array #1.

Finally, Array #3 possessed four SiPMs in an array (SensL SPMPlus [3-15]) and was unique in that the SiPMs were bonded into a ceramic well and coated in epoxy, not bonded to glass. Figure-3.5 shows the arrays used with CsI(Tl) crystals wrapped in PTFE matched to their respective areas.

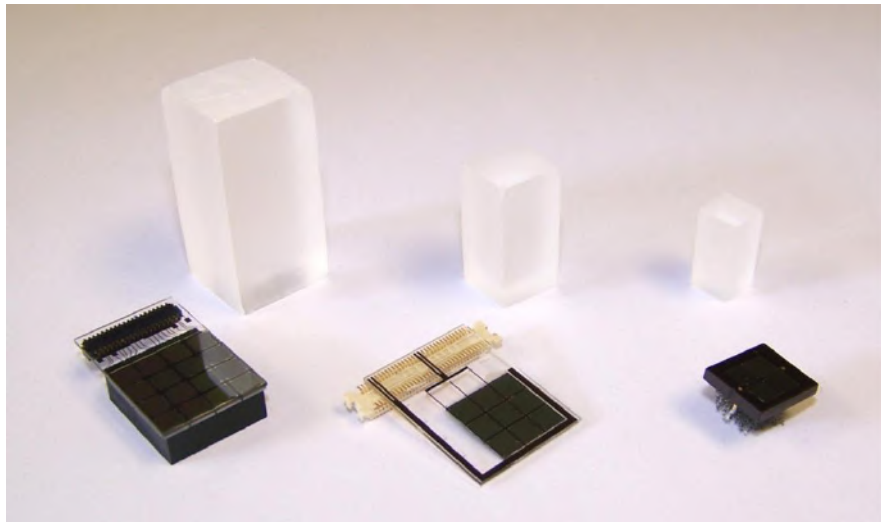


Figure-3.5: A photograph of three SiPM arrays obtained from SensL. From right to left, they have 16, 9 and 4 elements. Also shown are the CsI(Tl) crystals obtained from Hilger to test them. The 16- and 9-element arrays are constructed in the same manner, but are packaged differently. The 16-element and 4-element arrays are production models, whilst the 9-element array is an earlier prototype.

Tiled arrays were tested with a range of scintillators to establish which is best matched to SiPMs. Once a suitable scintillator was chosen, different array sizes were tested to understand how spectroscopic performance is determined by array size. It was possible to use a greater range of scintillators with tiled arrays as hygroscopic scintillators like NaI(Tl) and CsI(Na) require a hermetically sealed package which is not practical with a crystal of 2x2x15mm.

### 3.3.2. Measurement of Uniformity Across the Array

The uniformity of gain was measured across a SiPM array with individually addressed elements (Array #1). This was done using a 2x2x15mm crystal of CsI(Tl) wrapped in PTFE by placing it on each element in turn and taking a spectrum. By using the same crystal, the number of photons incident on the SiPM was kept consistent to allow the MCA channel number to accurately represent pulse height. No silicone grease was used to bond the crystal to the glass surface of the array to prevent it soaking into the PTFE and degrading LCE during the experiment. Individual elements were read out using the preamplifier channels on the board provided by SensL and the signals were passed to the same integrator as before with the shaping time constant of 2.2 $\mu$ s.

For each element Co<sup>57</sup> was used for its low energy peak at 122keV and the resolution and noise floor were recorded. There was found to be a pronounced variation in 122keV pulse

height with the average deviation from the mean being 11% and the greatest deviation being 28% (channel 5). In the case of channel 5, both the 122keV peak and 1cps noise level are lower, implying that the gain in this SiPM is lower, perhaps due to a higher breakdown voltage. This strong variation in pulse height indicates a strong variation in breakdown voltage and gain within the array. Figure-3.6 shows the measured noise level (1cps), 122keV channel and resolution for each element in the array. When taking spectra, it is anticipated that this non-uniformity will degrade performance somewhat by adding an extra term to the resolution formula.

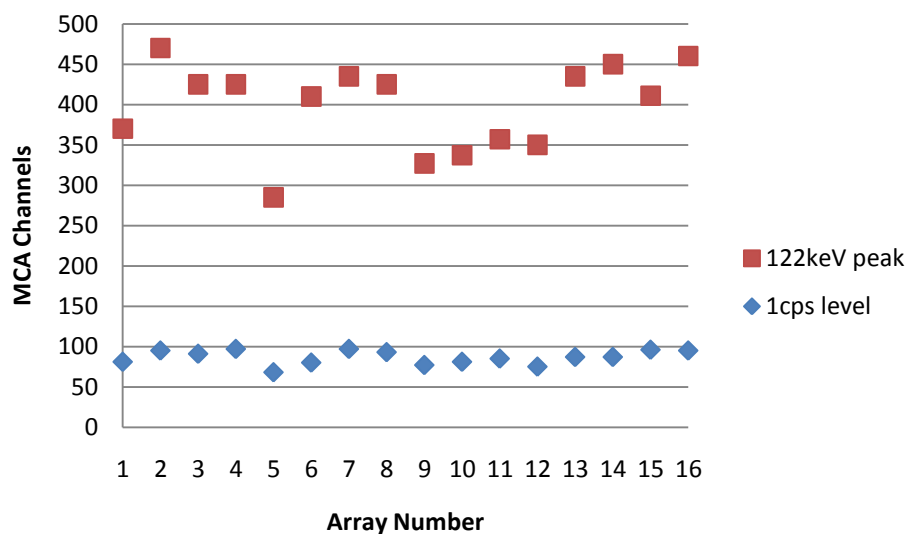


Figure-3.6: A plot of gain consistency over the 16-element array. The 2x2x15mm CsI(Tl) scintillator was used. For each element, the 1cps level and the 122keV photopeak are given.

### 3.3.3. Comparison of Different Scintillators with SiPMs

A range of scintillators exists and some are particularly suited to specific photodetectors or to specific applications. For example, LSO is chosen for use in PET for its high stopping power which reduces the necessary dose to the patient, and for its short decay time which improves timing resolution. However, it is unsuitable for spectroscopy due to its strong non-linearity. NaI(Tl) is the material of choice in spectroscopy as it is bright, fast and quite linear; it is also a good spectral match to PMT. CsI(Tl) is brighter and has a better stopping power, but is better suited to PIN diodes than PMTs due to emitting primarily green light.

This experiment also presented another opportunity to test our understanding of the performance of SiPMs by comparing the measured noise floor with predictions based on the findings at the end of Section 3.1.2. Data was compared with predictions of noise floor and

energy resolution to investigate in more detail the relationships between scintillator speed and noise, and brightness and resolution.

A range of scintillators were procured for comparison, as outline in Table–3.5 which shows the key properties of each scintillator. It is common to judge a scintillator by relative pulse height; typically relative to NaI(Tl) when coupled to a PMT, as this is a common configuration that produces good spectra. Such a comparison allows a convenient metric to judge relative performance. It is useful to perform a similar calculation to establish a metric for using a SiPM, in this case the 3035x13 from SensL. The number is generated as the product of light yield and peak PDE and scaled to CsI(Tl).

	<b>Density</b>	<b>Yield</b>	<b>Peak emission</b>	<b>Peak PDE</b>	<b>Time constant</b>	<b>Relative Pulse Height</b>
	g/cc	ph/MeV	nm	%	ns	
NaI(Tl)	3.7	38000	420	13	230	0.53
CsI(Tl)	4.5	52000	550	18	1000*	1.00
CsI(Na)	4.5	41000	415	13	600	0.57
LYSO	7.4	32000	420	13	40	0.44
BGO	7.1	8500	480	18	300	0.16

\*CsI(Tl) has a very long pulse with a two-component decay, though 1000ns is typically accepted as the principal decay time.

Table–3.5: A table of the key properties of the scintillator considered in this part of the study.

From the relative pulse height, it is possible to predict that CsI(Tl) will offer the best spectral performance, as the high light output and good spectral match will improve photon statistics. Noise floor is also a function of shaping time so faster scintillators like LYSO can be expected to have lower noise floor than their relative pulse height might suggest. For example, LYSO is expected to have a better noise floor than NaI(Tl) despite a lower pulse height, due to a faster pulse.

Figure – 3.7 demonstrates the matter of spectral match by plotting the PDE of the SiPM alongside the emission spectra of the scintillators. We can see that CsI(Tl) is the best matched as the majority of its emission falls within the sensitive range of the SiPM. The same is true of BGO, but its total light output is in fact much less (see table above). In contrast, LSO, NaI(Tl) and CsI(Na) all have peaks around 400nm, there the SiPM is much less sensitive. When calculating the relative pulse height and photon statistics for each scintillator-SiPM

combination, the emission spectrum must be convolved against the SiPM PDE spectrum to obtain an “effective PDE”, which takes into account the spectral match over the full range, not just the peak.

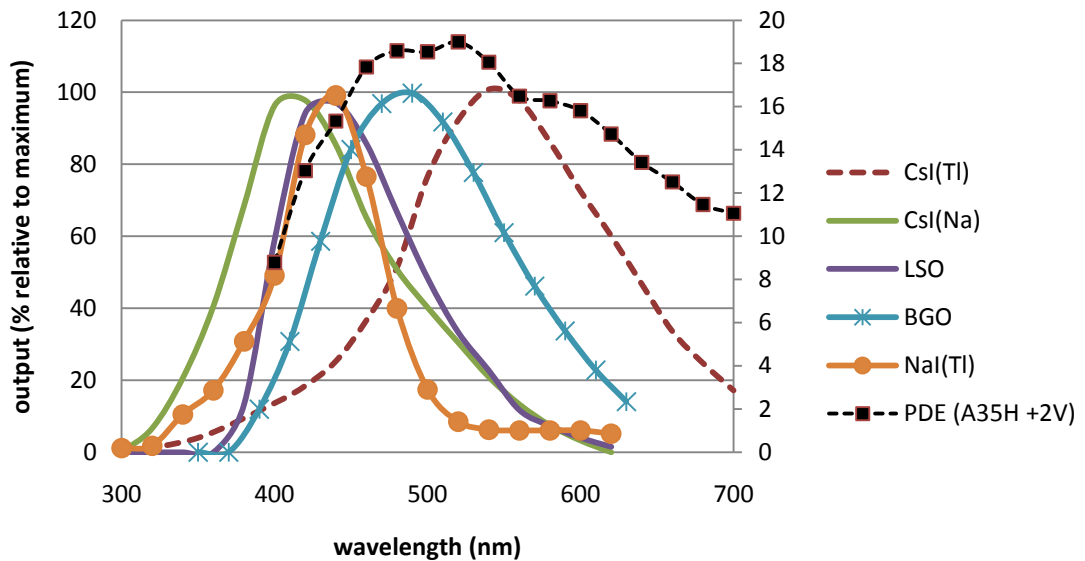


Figure – 3.7: The emission spectra of the scintillators tested. On the secondary axis we also show the SiPM PDE spectrum. The emission spectra were taken from Saint Gobain datasheets.

Array #1 was used in these tests. For consistent light collection efficiency (LCE), each crystal was the same size (a cube of side 1.2cm) and they were wrapped in PTFE. NaI(Tl) is hygroscopic and must be hermetically sealed. Therefore, each crystal was sealed inside an aluminium can and viewed through a 2mm thick glass window. It should be noted that not all of the bonds between crystal and glass were perfect, as the CsI(Tl) crystal was not well bonded leading to small air pockets creeping in from the edges and reducing LCE slightly.

In each case, the same integrator was used but with different shaping times to match the relevant pulse length and avoid collecting excessive noise. As outlined in Section 3.1.2., the microcell cycling time sets a lower limit on the integration time that may be used, so LSO, NaI(Tl) and BGO were all measured with a time constant of 400ns whilst the slower CsI(Na) and CsI(Tl) used integration time constants of 600ns and 2200ns, respectively. An Amptek 8000A (PMCA) was used to collect the spectrum and performance was measured in terms of energy resolution and noise floor (defined to be the 1cps level in the background spectrum, expressed in keV). As before, background subtraction had to be used with LYSO due to internal beta decays.

### 3.3.3.1. Measurements

The trend observed with single SiPMs was observed again here, with faster scintillators leading to a lower noise floor. Table-3.6 shows the measured performances of these scintillators.

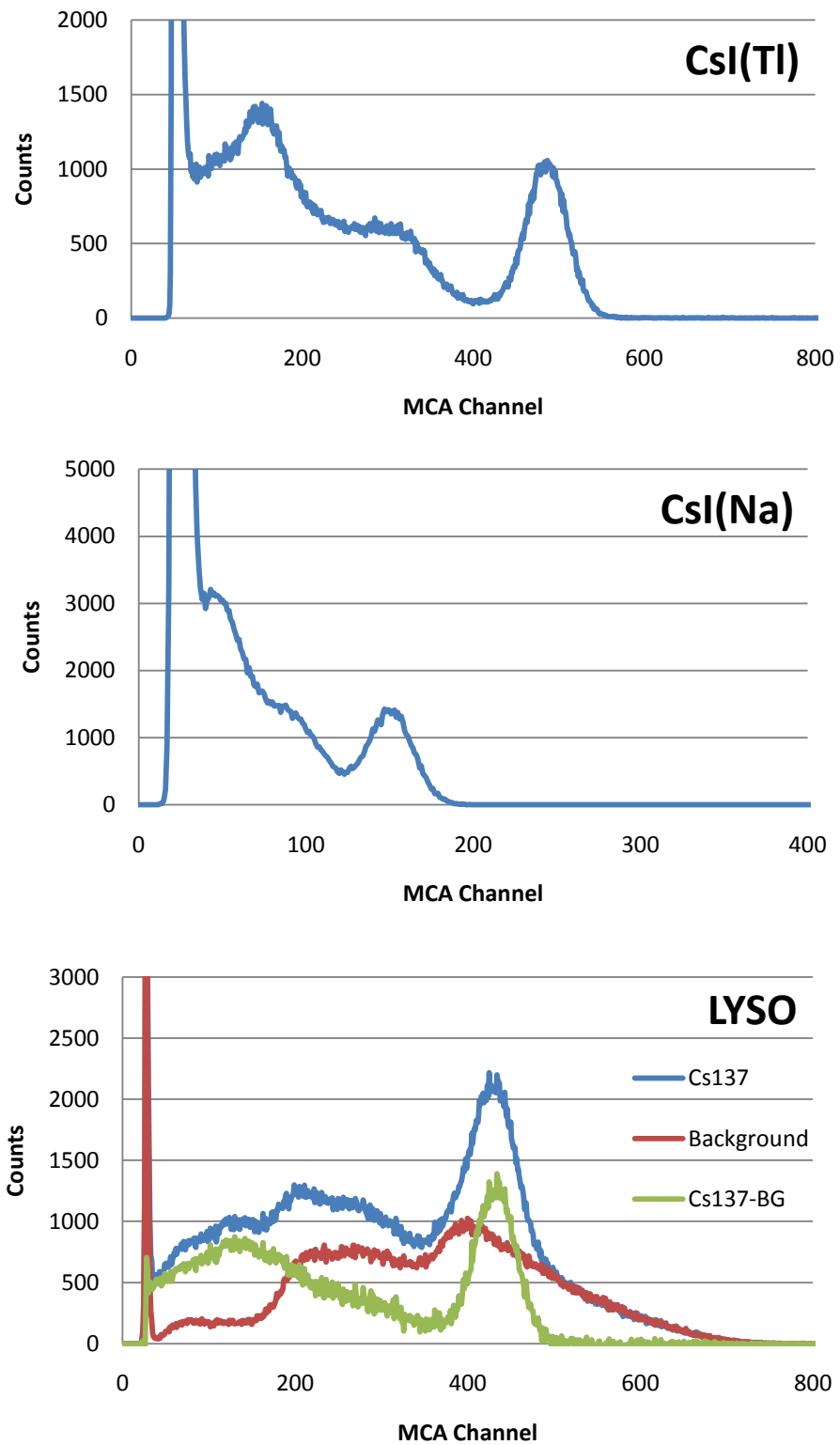
Figure – 3.7 shows  $^{137}\text{Cs}$  spectra achieved with these scintillators.

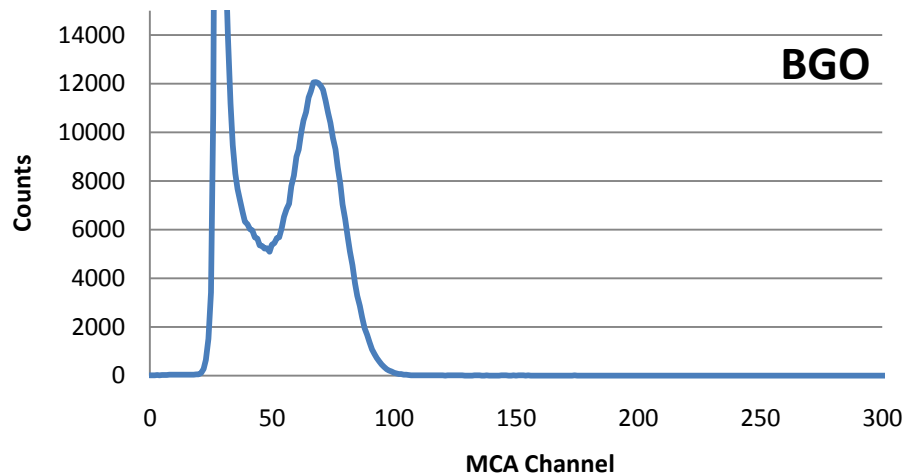
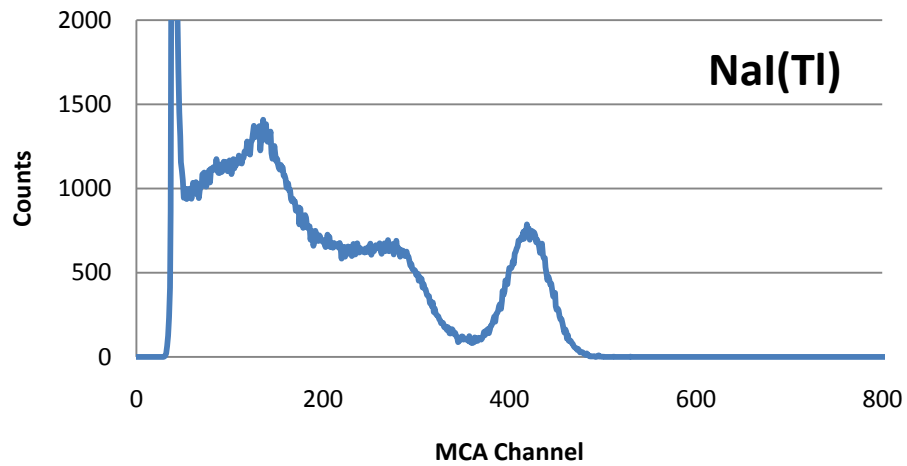
Scintillator	Nal(Tl)	CsI(Tl)	CsI(Na)	LYSO	BGO
FWHM at 662keV	11.40%	10.90%	17.80%	12%	28.60%
Noise Floor	72keV	79keV	157keV	55keV	340keV

Table-3.6: The measured energy resolution at 662keV and noise floor at the 1cps level of the scintillators considered here.

A good example of the effect of shaping time (and therefore pulse length) is a comparison between Nal(Tl) and CsI(Na) which have similar light output whilst CsI(Na) has roughly double the decay time and, as measured above, roughly double the noise floor. The trend is not absolute, however, as CsI(Tl) achieves a similar noise floor to Nal(Tl) through sheer brightness, evidenced by the improved energy resolution. At the same time, the energy resolution depends strongly on the scintillation yield and PDE as expected, with dimmer scintillators having more dominant statistical term to their resolution. BGO is roughly the same speed as Nal(Tl) but has a greatly reduced pulse height and so has a very high noise floor.

Figure – 3.8: The Cs<sup>137</sup> spectra taken with the five different scintillators. The absolute pulse heights should not be used as a judge of relative photon number, as the different shaping times in the amplifier caused different gains:





The spectrum taken with LYSO looks very different to the others due to internal radiation within the scintillator. Natural lutetium contains a beta-emitting isotope so background subtraction is necessary to be able to clearly see the  $\text{Cs}^{137}$  spectrum. Background subtraction in this case is simple as the internal count rate can be accurately known and so can be subtracted accurately. However, this process cannot be carried out in real time, as it were, and can only be done after a spectrum has been collected over a set time. This means that internal radiation can be subtracted to clean up a spectrum for isotope identification, but it cannot be removed from a process like PET. Internal radiation can be reduced by depleting the responsible isotope, but this is an expensive process.

We can see that the different scintillators have different photo-fractions, the fraction of counts that are full-energy deposits. A simple comparison is the height of the full-energy peak and the Compton edge. In NaI(Tl) they are almost level, whilst in CsI(Tl), the full-energy peak stands slightly higher. This is due to the higher average Z of the CsI(Tl). We would expect that CsI(Na) would have the same photo-fraction as CsI(Tl), but that does not appear to be the case

in the spectra above. This is due to CsI(Na) having such a poor energy resolution that the full-energy peak is spread over a wider number of channels and so the peak height is smaller. CsI(Tl) and NaI(Tl) have comparable resolution, so this simple comparison can still be made.

LYSO has a very high photo-fraction, due to its much higher average Z. This is always desirable, but especially so in PET where only coincident full-energy deposits of 511keV gamma-rays are used in image reconstruction. BGO also has a high photo-fraction, but this cannot be observed here due to the very high noise floor.

### **3.3.3.2. Discussion**

Based on this data, LYSO appears to be a very good scintillator for spectroscopy due to its low noise floor and decent resolution at 662keV, but it has some complicating factors such as a long afterglow which can distort peaks depending on count rate [3-16]. Again, LYSO demonstrates the limit on how fast a scintillator can be used as it is faster than the microcell cycle time. The resolution is also slightly worse than with the more traditional CsI(Tl) and NaI(Tl), due to a strong non-proportionality, which is more prominent at low energies. This non-proportionality limits the use of LYSO as a spectrometer. Finally, the lutetium is itself radioactive so a constant background subtraction will be required for use in a spectrometer.

NaI(Tl) gives the same resolution as CsI(Tl) and a slightly better noise floor with the brightness of CsI(Tl) being traded off against the speed of NaI(Tl). NaI(Tl) represents the limit of how fast a scintillator can be used as further speed advantages would be wasted with SiPMs. CsI(Tl) is preferred as it is only slightly hygroscopic and so is very convenient to use, whereas NaI(Tl) requires a hermetic seal, complicating manufacture and placing an extra optical interface between the crystal and the SiPMs. CsI(Tl) is also 22% denser, leading to greater stopping power for any given volume and energy.

### **3.3.4. Comparison of Different Array Sizes**

CsI(Tl) has been found to be a very useful scintillator, due to its high light output and a good spectral match. However, it has a very long pulse that increases the contribution of dark count noise to both noise floor and resolution. The dark count rate in SiPMs scales linearly with active area so smaller arrays coupled to smaller crystals can be expected to have a lower noise floor and better energy resolution. It is therefore interesting to experiment with this concept and compare the performances of different sizes of array.

In this experiment, SiPM arrays of 4-, 9-, and 16-elements were compared, with each element being a 3mm x 3mm 3035X13 SiPM from SensL. The 9- and 16-element arrays were

constructed in the same way, that is, the SiPMs were bonded onto gold tracks deposited on a glass slide. They were illuminated through the slide and optical epoxy was used to ensure a good contact between the slide and the SiPM faces. The 4-element array and single element were different in that the SiPMs were bonded by their backs into a ceramic well with their front faces covered by a thin layer of epoxy.

As the aim is to study how array size affects performance, it is important to ensure that the LCE of the crystal is the same in all cases. This was achieved by giving each crystal the same aspect ratio of 2:1 and surface treatment. The sides and ends of each crystal were abraded and wrapped with ~10 layers of PTFE tape, except the window that was polished and bonded to the SiPM array with silicone grease. Table–3.7 gives data on each array and their respective crystals.

The three detectors were tested in the same manner as before by exposing them to a range of gamma-ray energies and measuring the FWHM and SiPM noise to determine performance. The noise floor was defined to be level at which one count per second was observed in the background spectrum. This level was compared to the 662keV photopeak in order to express the noise floor as an energy, termed the Noise Equivalent Energy (NEE).

As CsI(Tl) is the scintillator in question, the output of the pre-amplifier was passed to an integrator with a time constant of 2.2 $\mu$ s and a low pass filter. The filter and long response time of the integrator served to reduce the response to SiPM noise. Integrated pulses were then passed to an AmpTek PMCA to generate a spectrum for analysis.

### 3.3.4.1. Measurements and Discussion

Table–3.7 shows, as well as the dimensions of the detectors, their performance in terms of noise floor and energy resolution.

No. SiPM	SiPM Area	Crystal size	59keV		662keV		Noise floor	
			ch	FWHM	ch	FWHM	ph	keV
16	144	14x14x28			435	10%	539	72keV
9	81	10x10x20	43	33%	439	8.6%	254	34keV
4	36	6x6x12	40	38%	407	9%	254	34keV

Table–3.7: The measured performance of the three arrays with their respective CsI(Tl) crystals, each sized to provide the same light collection efficiency in each case.

Figures - 3.9 and - 3.10 show spectra taken with the 16-element and 9-element SiPMs, respectively, to demonstrate visually the lower noise floor of the latter case.

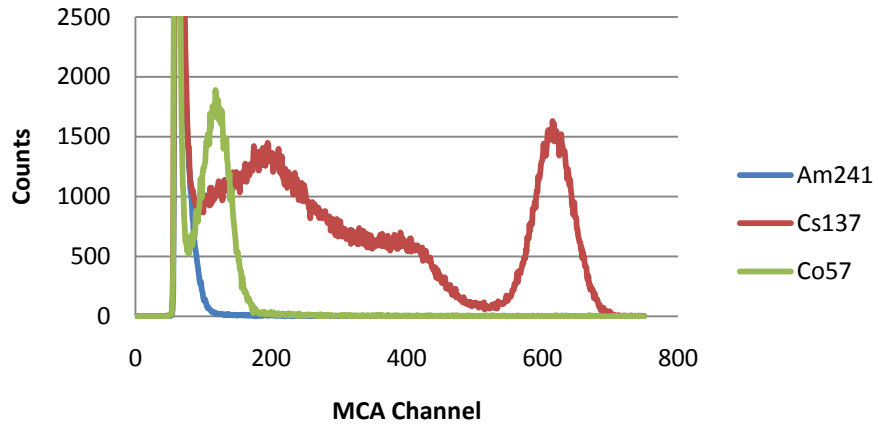


Figure-3.9: Some spectra taken with the 16-element array and the 14x14x28mm CsI(Tl) crystal.

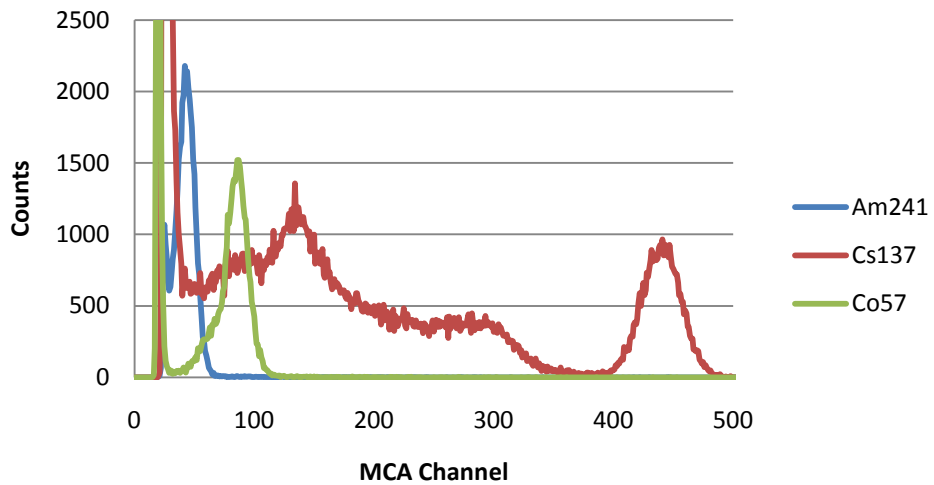


Figure-3.10: Spectra taken in the same manner using the 9-element array and the 10x10x20mm CsI(Tl) crystal. Note how the 59keV peak of Am<sup>241</sup> is visible due to the greatly reduced noise floor.

It was anticipated that the noise floor would scale linearly with sensitive area. That is, given that the 16-element array has a noise floor of 72keV, we expect the 9-element to have 40keV and the 4-element to have 18keV. However, the noise floor of the 4-element array matches that of the 9-element array, instead of having 44% the noise. This is unexpected as the SiPMs were employed as elements, and may be due to a higher noise rate in the SiPMs that make up

the 4-element array or a poor crystal with a lower light output than expected. This implies that the noise rate is a factor of  $81\text{mm}^2/36\text{mm}^2 = 2.25$  times higher per unit area, though it is difficult to understand why. The reason for this discrepancy is likely to be how the MCA triggers off noise pulses that form a wildly fluctuating level.

The full-energy peak channel number is found to be 7% lower with the 4-element array than the 9-element array, likely due to a small variation in breakdown voltage or SiPM temperature during the experiment.

The energy resolution using a 9-element array is better than with a 16-element array due to better VLCE in the much smaller crystal and a reduced noise contribution, assuming all other terms to be equal. As before, the energy resolutions are overestimated slightly but generally accurate. However, the trend of improving resolution with reducing area does not seem to be present in the predictions.

#### **3.3.4.2. Summary on Tiled Arrays**

A resolution of 9% at 662keV was achieved with 9-element array having area  $1\text{cm}^2$ . This compares unfavourably with the 7% regularly achieved with PIN diodes of  $1\text{cm}^2$  [3-17] with similar CsI(Tl) crystals wrapped in PTFE, but a number of improvements in SiPM design are available in the future. The energy resolution achieved with SiPMs is poorer than with PIN diodes due to poorer photon statistics due to lower PDE. It is interesting to note that despite the SiPMs used having roughly 25% the PDE of PIN diodes (QE=80-85%), equivalent performance in terms of noise floor is achieved. This is because SiPMs possess high gain so the contribution of electronic noise is negligible, whilst in PIN diode-based detectors it is a strong contributor to energy resolution and noise floor.

The noise floor achieved with SiPMs is already comparable to what has been achieved with PIN diodes [3-17] so, at present, a slight drop in energy resolution may be traded off against gain when choosing between SiPMs and PIN diodes for reading out compact CsI(Tl) scintillators. This is an important point in assessing the potential impact of SiPMs on radiation sensing, that equivalent performance can be achieved with well established devices like PIN diodes whilst possessing other advantages. These advantages include greatly reduced sensitivity to gamma-ray interactions or charged particle interactions in the photosensor, and high gain.

### 3.3.5. Potential Applications of Tiled Arrays with CsI(Tl)

#### 3.3.5.1. Gamma-Ray Spectroscopy for Security Purposes

Gamma-ray detectors have a significant role to play in security by detecting attempts to smuggle radioisotopes, or to be used by first responders at the scene of a radiological bomb attack. Spectroscopy is important in this field to allow rapid distinction between threat sources and normal sources. Simple non-spectroscopic detectors tend to lead to high false-alarm rates and unnecessary searches, which can impede the flow of normal commerce. Systems already deployed include portals for scanning trucks at ports or crossings, individuals at airports or public events, or baggage scanners. Such applications require large detectors for the sake of sensitivity and SiPMs may not be suitable at this stage. However, there is a requirement for hand portable gamma-ray spectrometers. Examples of uses include custom officers searching vehicles or vessels or first responders after an attack.

Application-specific requirements for small spectrometers should be outlined at this point. ANSI has specified [3-18] a list of isotopes that must be detected by handheld spectrometers, thus defining the energy range in which the spectrometer must operate. The low energy limit is 59keV from  $^{241}\text{Am}$ , set as this is the principal emission of the isotope. Detecting  $^{241}\text{Am}$  is important as it is typically found with plutonium and so is a suspicious source. In order to convincingly resolve a 59keV photopeak, the noise floor should be in the region of 30keV.

A good energy resolution is also required of a spectrometer to distinguish between incident gamma-rays to allow isotope identification. As SiPM arrays are available only in sizes similar to PIN diodes, a useful target resolution is 7% at 662keV, achieved with CsI(Tl) crystals of a few cubic centimetres on a  $1\text{cm}^2$  diode [3-19]. If both of these targets can be met with a SiPM and crystal of similar size, then SiPMs can be argued to be useful alternatives to PIN diodes as both spectrometers and imaging elements.

Large area SiPM arrays ( $\sim 1\text{cm}^2$ ) are of interest in this field as they are similar in size to PIN diodes and can be used to read out similar volumes of scintillator. They also have a high intrinsic gain that allows for cheap and compact electronics to process pulses, reducing the cost of small handheld instruments. If good performance can be achieved with a SiPM, then handheld instruments can be designed around them with lower cost than CZT-based systems. CZT is cadmium-zinc-telluride and it is the first room-temperature semiconductor spectrometer. It has therefore attracted a great deal of interest and has excellent energy resolution. CZT is also limited to small volumes as charge-trapping become problematic in volumes approaching 1cc, limiting sensitivity despite their high density (6.2g/cc) unless tiled in large arrays [3-20].

By tiling SiPMs in arrays, it has been possible to achieve the required noise floor of  $\sim 35\text{keV}$  with a crystal of  $9\times 9\times 18\text{mm}$  (1.5cc) and a SiPM of  $1\text{cm}^2$ , even though the energy resolution is worse than regularly achieved with PIN diodes at 9.5% at 662keV. However, PIN diodes are a mature technology whereas SiPMs have a number of improvements available over the SiPMs used here. Also, SiPMs have the advantage of high gain, allowing for low cost electronics to be used. In comparison, a PIN diode may achieve 6% at 662keV but only with an expensive low-noise amplifier. For these reasons, SiPMs are a viable alternative to PIN diodes in this field, especially when cost is a priority. Exploration of how SiPM-CsI(Tl) detectors could be used in gamma-ray spectroscopy makes up Chapter 4.

### 3.3.5.2. Gamma-ray Astronomy

SiPM-based detectors have a role in gamma-ray astronomy as imaging elements. Instruments in space have to endure a harsh radiation environment, principally energetic protons and electrons from the solar wind, van Allen belts and cosmic rays. This hard radiation damages scintillators, photosensors and electronics alike, with cosmic rays being a particular problem due to depositing large quantities of energy in crystals inducing a bright flash and long afterglow, overloading electronics and creating spurious counts. High-energy charged particles also interact with the photosensor by depositing energy directly into the photodiode in the form of a track of electron-hole pairs. This leads to a very large pulse and can damage the PIN diodes commonly used. The high background flux also leads to noisy electronics and difficulties in calibration.

An example is the imaging system of the INTEGRAL observatory, made up of an array of CsI(Tl) crystals of a few cc, each read out by a  $1\text{cm}^2$  PIN diode, combined with a coded aperture. Such a configuration can be expected to achieve an energy resolution of 6% at 662keV. Whilst the noise floor can be matched with  $1\text{cm}^2$  SiPMs viewing similar sized crystals, the resolution they provide is worse at 9% at 662keV, due to relatively poor optical photon statistics.

Nonetheless, such imaging elements are not required to work in a spectroscopic mode and are typically used for continuum measurements, so a drop in resolution from 6% to 9% is not significant.

SiPMs may be able to offer other advantages based on their gain as less sensitive preamplifiers may be used, improving resistance to radiation. Also, the direct interaction of gamma-rays and particles with the depletion region is highly unlikely, helping prevent spectral noise and damage. It is anticipated that a high-energy particle, such as a cosmic ray, would deposit its energy in the SiPM as a track of electron-hole pairs. This track would then trigger avalanches in a few microcells, leading to a pulse no bigger than a few photoelectrons.

### **3.3.6. Potential Improvements in Small SiPM-based Gamma Detectors**

SiPMs have already been shown to provide good spectral performance with CsI(Tl), but they are limited by high thermal noise and low PDE. However, SiPMs are a nascent technology with a number of improvements possible. Also, a range of recently developed scintillators have shown promising performance, such as lanthanum bromide, made by Saint Gobain.

#### **3.3.6.1. Improvements in SiPM Technology**

At present, SiPMs may be regarded as equivalent in performance to PIN diodes despite their immature nature. Good performance was achieved with 35 micron microcells giving a peak PDE of 18%. PDE may be improved by using larger microcells to improve fill-factor. SensL intend to produce SiPMs with 50 micron microcells and a 50% improvement in PDE. This will not lead to a direct improvement in noise floor as increasing the active area on the chip will also increase the dark count rate by the same factor. However, an improvement in optical photon statistics of 50% can be expected, so the energy resolution of the 662keV peak of the 16-element array coupled to a 14x14x28mm CsI(Tl) is predicted to improve from 9.5% to 7.6%, within the range expected of a PIN diode and CsI(Tl). This figure is reached by simply increasing photon statistics by 50%.

Given that dark counts in SiPMs are due to thermal excitation, improvements can be expected from cooling. Thermal noise in silicon photomultipliers typically falls by half for every 10K of cooling and the dependence of noise and gain on temperature in SiPMs has been explored in some detail [3-21]. If the 16-element array used above is cooled by 10K, then we can expect the noise floor to halve to ~35keV.

#### **3.3.6.2. Application of Recent High-Performance Scintillators**

It has been found that SiPMs favour fast and bright scintillators, in common with other photodetectors, and in the set of scintillators tested in this study, those properties do not appear to occur at the same time. Recently, cerium-doped lanthanum bromide (LaBr(Ce)) has offered superior performance over NaI(Tl) with PMTs, such as an energy resolution of 3% at 662keV [3-22]. Good performance may also be achieved by coupling a small crystal of LaBr(Ce) to an APD: Flamanc and Rozsa achieved a resolution of 2.8% at 662keV at room temperature with a noise floor of 17keV [3-23]. Figure – 3.11 shows a sample Cs<sup>137</sup> taken from ref [3-23] showing the good energy resolution and low noise. In this case, a blue-sensitive APD from Hamamatsu was used (S8664). This is due to LaBr(Ce) being both fast and bright, whilst also having good temperature stability and a low intrinsic resolution.

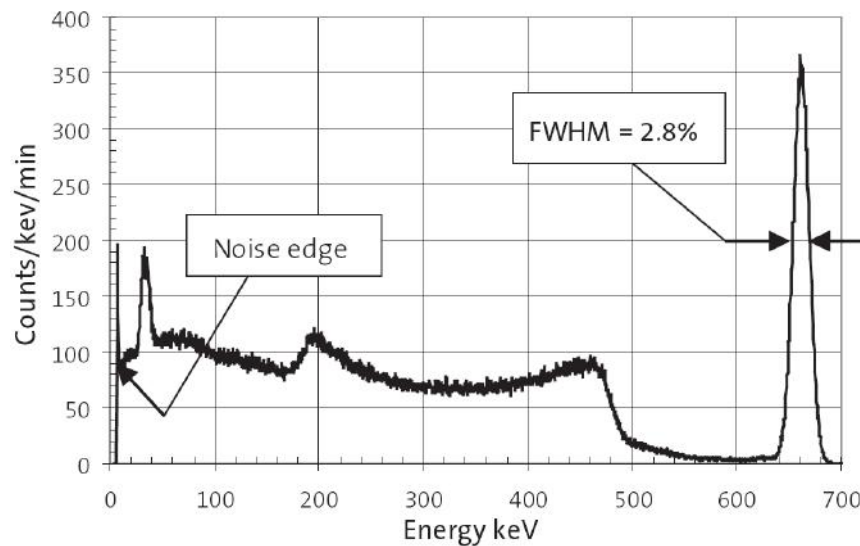


Figure – 3.11: A sample  $\text{Cs}^{137}$  spectrum taken from ref [3-23], showing the good performance attained by coupling LaBr(Ce) to an APD. Note that the 32keV peak is visible.

Similar performance cannot be expected of LaBr(Ce) when coupled to a SiPM as its emission peaks at 380nm, leading to a peak PDE of only 4%. The poor match of SiPM and LaBr may be addressed by making SiPMs more sensitive to shorter wavelengths. This approach exploits the dependence of Geiger probability on wavelength as discussed in Section 2.2.3. in that the structure of the diode is inverted from “n on p” to “p on n”. Blue photons will therefore interact closer to the p-junction, increasing the Geiger probability at low wavelengths. If the PDE at 380nm is increased to 15%, for example, then good performance is expected. Taking the numbers above as a baseline, we can expect the noise floor to improve to  $\sim 20\text{keV}$ , as the PDE has more than tripled. Resolution is predicted to improve to 12%, again anticipated to be an upper limit. If this performance can be achieved, then the expense of using LaBr(Ce) could perhaps be justified, even though energy resolution is still poor compared to that achieved with APD [3-23] or even a PIN diode with CsI(Tl).

As indicated by the predictions above, inverting SiPM structure to create blue sensitive SiPMs will be a useful step as it will make SiPMs less dependent on CsI(Tl) for good resolution so the speed of the blue and bright scintillators like LaBr or NaI(Tl) may be exploited.

Another, more immediate approach would be to use a wavelength shifter such as EJ-280 [3-24] as a light pipe between a LaBr or NaI(Tl) crystal. This will lead to a more favourable spectral match at the expense of efficiency, as an extra process is introduced. EJ-280 itself is more suited to NaI(Tl) in this case as the absorption efficiency is  $>90\%$  at 415nm, whilst it is only 15% at 380nm.

### 3.4. Conclusion of Evaluation of SiPMs in Radiation Sensing

Over the course of this chapter, SiPMs have been demonstrated to work well in a number of small scale applications using scintillator readout. It was found that the high noise and low PDE of SiPMs define how they may be used. They determine what scintillators they may be used with; the high noise means that fast scintillators like LYSO and LaBr(Ce) are favoured, though this may be overcome by sheer brightness, such as when CsI(Tl) is used.

In terms of specific applications, it was found that single SiPMs of  $9\text{mm}^2$  can be useful as PET elements, achieving an energy resolution of 11% at 511keV when coupled to LSO crystals. The small size of SiPMs allows for dense packing of these elements, especially if tiled in an array. Using CsI(Tl) instead will also produce a useful small dosimeter.

When all elements of a tiled array are read together, they have also been found to make useful gamma-ray sensors for either coded mask imaging or spectroscopy, although the noise floor must be traded off against sensitivity: 59keV gamma-rays can be resolved but only by 9-element arrays of  $1\text{cm}^2$ . This exploits the good match found between SiPMs and CsI(Tl) and are comparable to PIN diodes in terms of noise floor but not in terms of resolution. This is due to the poor PDE of SiPMs compared to PIN diodes whilst the high gain reduces the contribution of electronic noise to the noise floor.

Whilst a useful spectrometer can be built using SiPMs (9% at 662keV, and a noise floor of  $\sim 35\text{keV}$ ) it is noise that limits volume of 1.5cc, as a SiPM array larger than 9 elements generates too much noise for 59keV gamma-rays to be resolved. Therefore, SiPM-CsI(Tl) spectrometers are limited to paging spectroscopic dosimeters and is too small for handheld spectrometers, where sensitivity is required. With this in mind, the next chapter explores how SiPMs can be used in a wider range of gamma-ray spectroscopy applications by increasing sensitivity without increasing SiPM area.

## 4. Development of a Practical Portable Spectrometer

### Using SiPMs

#### 4.1. Introduction

In this chapter, tiled arrays of SiPMs will be investigated in the more specific context of portable gamma-ray spectroscopy for isotope identification. Results from the previous chapter indicated that a useful spectrometer could be constructed using SiPMs coupled to CsI(Tl) but the crystal geometry used limited the device to a few cubic centimetres, thereby severely limiting their sensitivity. In this chapter, the compact spectrometer concept is explored further by investigating how sensitivity can be improved by increasing crystal volume. There is a strong market for compact detectors for use in small handheld spectrometers, so this work was carried out in the context of developing such a device.

The development work was carried out in stages. Firstly, readout of a large (112cc) scintillator with a 16-element SiPM array was studied. It was found that LCE was too low, causing poor spectral quality. A range of smaller scintillators down to 21cc was tested with the same SiPM array to understand how LCE varied with size. The use of SiPM cooling and smaller 9-element arrays was also investigated.

##### 4.1.1. Requirements and Specification

Given the decision to investigate these instruments in terms of hand portable instruments, certain requirements become explicit. Firstly, ANSI has specified [4-1] a list of isotopes that must be detected, thus defining the energy range. The lowest energy gamma-ray from the listed isotopes is 59keV from Am<sup>241</sup>, which is typically found with plutonium and so is a 'suspicious' source. In order to clearly resolve a 59keV full-energy peak, the noise floor should be in the region of 30keV.

Sensitivity is particularly important in this field as it determines how long it takes to collect useful spectra. It is determined predominantly by the size and stopping power of the scintillator, so large crystals of dense material are preferred.

Finally, energy resolution is the key property of a gamma spectrometer. To provide a target resolution we must consider what is commonly used in the field. For example, a 2" cylinder of NaI(Tl) crystal coupled to a 2" PMT will have a resolution of 6% at 662keV [4-2], and a similar resolution can be expected of a PIN diode system with CsI(Tl) [4-3]. If a SiPM system is to compete in the security market, a similar energy resolution will need to be achieved, as

isotope identification is required to separate threat sources such as enriched uranium from background or medical sources. Isotope identification prevents false alarms and unnecessary searches being triggered by benign sources. As CsI(Tl) proved to be well matched to SiPMs in the previous chapter, it was decided that CsI(Tl) would be used in the further development described in this chapter. CsI(Tl) is also suitable for handheld systems as it is robust and more resistant to shattering than NaI(Tl) and so can survive rough handling and accidental damage more easily. This is advantageous as it reduces the total instrument volume and mass devoted to shock protection.

#### **4.1.2. Exploiting a Novel Scintillator Configuration**

As stated, the objective of this stage of development is to increase the volume of a SiPM-based spectrometer without sacrificing spectral performance using a large area SiPM array. From the results of the previous chapter it is clear that SiPMs cannot easily be scaled up to match a 2" crystal (103cc) due to the high noise rate per unit area. Therefore, in order to achieve the same sensitivity a method is needed that will couple a large crystal of roughly 100cc to a small photosensor. This can be achieved by simply extending the square section crystal out into a long bar, though this will lead to a strong roll-off of LCE along the length of the bar [4-4].

An alternative configuration explored in 2001 by Meng et al [4-5] used spherical crystals of CsI(Tl) packed in white powder (MgO in this case) and read out by a PIN diode, called a ScintiSphere. The concept relied on the high diffuse reflectivity of packed powder to reflect optical photons many times, integrating the scintillation flash to achieve good uniformity and unusually high LCE for such a large crystal and small photosensor. Good results were achieved using a 100cc sphere with a 1cm<sup>2</sup> PIN diode, such as an energy resolution of 7.7% at 662keV. It was found that, despite the apparent mismatch in size, a LCE of 40% was measured.

However, the performance in terms of noise floor was limited to around 200keV by a high leakage current and pre-amplifier noise. PIN diodes have no intrinsic gain, so amplifier noise has a strong effect on performance, contributing a great deal to energy resolution as well as noise floor. For example, at 662keV, electronic noise contributed to over half the energy resolution in a 100cc sphere read out by a 1cm<sup>2</sup> PIN diode. The high noise floor meant that spheres read out by PIN diodes could not be used as isotope identifiers so neutron activation analysis was proposed as an alternative application.

Using SiPMS in a spectrometer exploits the high intrinsic gain to reduce the relative influence of amplifier noise on spectral performance. Investigating ScintiSpheres seems to be a natural choice as it exploits the compatibility of SiPMs with CsI(Tl) and appears to be the most efficient

way of coupling a small photosensor to a large crystal to gain sensitivity. In the context of hand portable instruments, such a detector would be useful as it would be robust, cheap, compact, and insensitive to magnetic fields.

Therefore, work in this chapter focuses on the development of a useful gamma-ray spectrometer using the ScintiSphere concept and a SiPM array.

#### 4.2. Initial Testing of a Large Sphere for Handheld Spectrometers

A sphere of diameter 6cm and volume 112cc was manufactured by Hilger Crystals in order to closely match the volume of the original spheres and a 2"x2" cylinder (103cc). This allows an analysis of how well ScintiSpheres work with SiPM compared to PIN diodes. It also allows a measurement of the spectral performance of a sphere with comparable sensitivity to a standard 2" NaI(Tl) crystal, thereby establishing if SiPMs can be used in the large handheld market. Geant 4 simulations predict that a 112cc sphere of CsI(Tl) is 95% as sensitive at 662keV as a 2" cylinder of NaI(Tl).

The crystal was prepared in a similar manner as in the original ScintiSphere work, with the surface abraded until nearly opaque and then packaged in white alumina powder, to maximise reflectivity. Previous work estimated that a reflectivity of  $\epsilon \approx 99\%$  [4-6] was achieved in this way. An array of 16 SiPMs (3035X13 from SensL) was bonded using MeltMount (a reusable hot-melt glue from Cargille) onto a flat circular window of diameter 20mm machined into the surface of the sphere. The diameter of 20mm was selected to match the diagonal of the array so the whole array was in contact with the window. To prevent light escaping around the SiPM array, it was buried in the alumina powder. As before with small CsI(Tl) crystals, the preamplifier output was integrated with a time constant of 2.2 $\mu$ s and analysed by an Amptek PMCA in order to determine the noise floor and resolution. Figure – 4.1 shows a sketch of the experimental set-up.

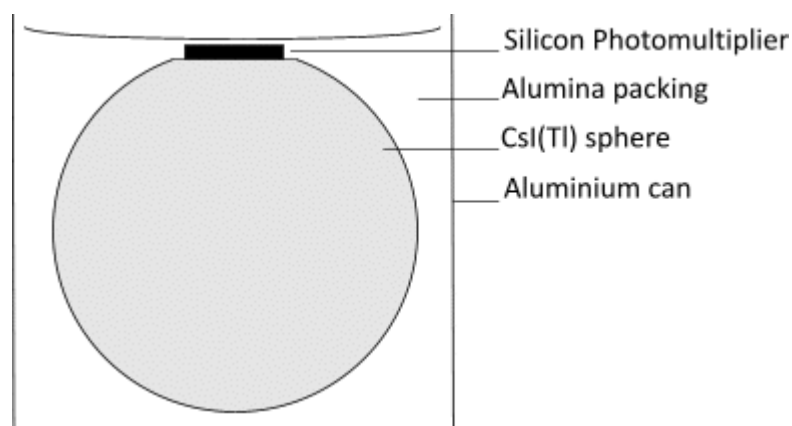


Figure – 4.1: A sketch of the scintillator configuration and packaging.

#### 4.2.1. Measurement of Energy Resolution

Spectra obtained from this detector are shown in Figure-4.2 in the form of a Cs<sup>137</sup> spectrum laid over the background. Compare to the spectra shown in Figure-3.7, taken with the same SiPM array, to see the effect of relatively poor LCE on resolution and noise floor.

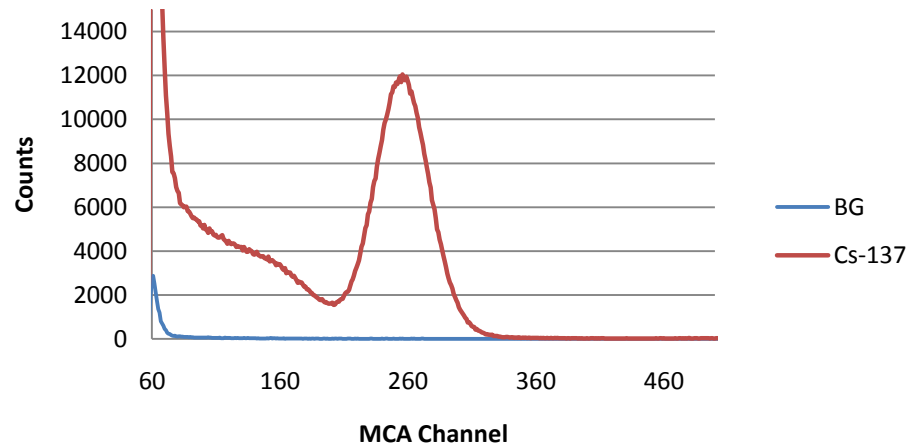


Figure-4.2: Spectra obtained with the first ScintiSphere, a 112cc volume of CsI(Tl) read out by a 16-element array of 3035 SiPMs.

The measured resolution at 662keV is poor at 18% but better than expected, Table-4.1 shows the breakdown of the individual contributions to energy resolution at 662keV. Optical Monte Carlo simulations were carried out to predict the light collection efficiency and its variation in order to predict energy resolution. A sphere of CsI(Tl) was defined and surrounded by a hollow sphere of white diffuse reflector with  $\epsilon = 98.5\%$ . Unlike in Section 3.1.3, the assumption of totally diffuse reflection was more valid as the crystal surface was abraded to encourage diffuse reflection. A window was left in the reflector and a volume defined that counted the photons that struck it. By moving an isotropic photon source about within the CsI(Tl) volume it was possible to simulate the uniformity in LCE. The flash was moved in a cubic grid so that each location represented an equal fraction of the volume. This simulation predicted a LCE of  $34 \pm 3\%$ . Using this and a PDE of 16% we can predict the energy resolution to compare against measurements.

The statistical term and VLCE term are based on a simulated LCE of 34% with a  $1\sigma$  variation of 3% absolute, corresponding to a 9% relative variation. This VLCE term dominates the predicted resolution. SiPM noise term is calculated based on a noise rate of  $0.77\text{MHz/mm}^2$  and an active area of  $144\text{mm}^2$ .

$N_{\text{photons}}$	$R_{\text{stat}}$	$R_{\text{VLCE}}$	$R_{\text{int}}$	$R_{\text{SiPM Noise}}$	FWHM (estimated)	FWHM (measured)
2100 photons	46 photons	186 photons	34 photons	27 photons	461 photons	
	2.2%	8.8%	1.6%	1.3%	21.9%	18%

$N_{\text{photons}}$	$R_{\text{stat}}$	$R_{\text{VLCE}}$	$R_{\text{intrinsic}}$	$R_{\text{Preamp}}$	FWHM (estimated)	FWHM (measured)
13240 photons	0.9%	0.6%	1.6%	2.7%	7.9%	7.7%

Table-4.1: A breakdown of the terms contributing to energy resolution at 662keV for the 112cc sphere (upper panel) and the 100cc sphere with PIN diode (lower panel). Each of the resolution components is given at  $1\sigma$  unless stated otherwise. The number of photons captured is calculated and given in each case. In the case of the lower panel Ref.[4-5] gives each term as a percentage at  $2.35\sigma$  (FWHM). These values have been converted to  $1\sigma$  for easy comparison.

The predicted resolution at 662keV is worse than the measured value and it is difficult to determine which term contributes to the inaccurate calculation of energy resolution. Photon statistics ( $R_{\text{stat}}$ ) is dependent upon LCE, which has been measured by comparing spectra with the small block (14mm x 14mm x 28mm) which is assumed to have a LCE in the region of 80%. By comparing the pulse height of the 662keV photopeak for the same SiPM bias voltage, the 112cc sphere was found to be 43% as efficient, giving a LCE of 34%, matching the Monte Carlo simulation, so we can assume that this is roughly correct.

The predicted VLCE term is likely to be incorrect, as previous work with PIN diodes indicated a uniformity term of 0.6% (at  $1\sigma$ ) [4-6]. Substituting in 0.6% (relative contribution) for the 8.8% above, this reduces the predicted energy resolution at 662keV to 6%, well below the measured value. It is strange that the measured value of 0.6% should result in a less accurate prediction than the simulated value of 8.8%. It is possible that the VLCE of this sphere is much worse than that of the first spheres, where the figure 0.6% came from, but such a difference is unreasonable. Another possibility is that the doping concentration is not uniform over the

volume of the sphere, causing the light yield to vary. This would cause broadening of the peak in the same way as the VLCE term, but would be difficult to separate.

This detector has somewhat poor spectral performance with the 662keV peak having a resolution of 18%, compared to the 7.7% achieved with PIN diodes, and this is due to the trade off between PDE and gain. It is certain that using a SiPM produces poorer photon statistics due to a lower PDE of 16% compared to 85%. At the same time the SiPM gain has greatly reduced the noise term by making any contribution of the preamp negligible, so noise is dominated by dark counts. The intrinsic uniformity term includes the variation in light output over the crystal and it is possible that the 112cc sphere has non-uniform doping concentration, though this cannot be measured or separated from the VLCE term.

#### **4.2.2. Noise Floor**

In terms of noise floor, SiPM readout of the 112cc sphere achieves comparable readout to that with a PIN diode, with the 1cps level in the background corresponding to 168keV. The combination of sphere and PIN diode was unable to resolve peaks below 200keV. The noise floor was predicted as in Chapter 3 using an integration time of  $2.2\mu\text{s}$  and a noise rate of  $0.77\text{MHz/mm}^2$ , and a figure of 250keV was reached. The noise floor is better than predicted, indicating some error in the calculation, again likely in how the MCA handles the dense population of random noise pulses.

#### **4.2.3. Conclusion**

In conclusion, it is clear that the concept of using SiPMs with ScintiSpheres is indeed sound, in principle, excepting the poor energy resolution achieved with SiPMs. SiPMs have a far lower PDE due to the fill factor which increases the statistical term of resolution. However, SiPMs retain the key advantage of gain, which removes the contribution of preamplifier noise to the noise floor. Spectral performance can be addressed by improving PDE, improving LCE or reducing noise. Improving PDE is a long term issue of SiPM design, and can be achieved by moving to larger microcells to improve fill-factor, though that is beyond the scope of this study. In the context of improving the performance of ScintiSpheres with current SiPMs in order to find the range of applications, effort has been expended to improve firstly LCE and then noise.

### 4.3. Improvement of LCE by Reducing Sphere Volume

It has been shown [4-6] that LCE increases with the fraction of the surface area in contact with the photosensor (termed percentage contact area). In this experiment, the percentage contact area has been increased by reducing the volume of the sphere, trading off sensitivity for LCE. The aim is to understand how LCE depends upon percentage contact area and how this relationship can be exploited to gain a useful spectrometer by increasing photon statistics.

With this in mind, a series of spheres were acquired from Hilger Crystals and Scionix with volumes 21cc, 47cc and 64cc. Each sphere had the surface abraded to the same opacity as the 112cc sphere and was packed in powdered alumina to achieve the same reflectivity. The 47cc sphere arrived with a square stalk of 7mm length protruding from the flat, and so may be expected to deviate slightly from the rest. For the sake of comparison, the small block of CsI(Tl) (14x14x28mm) wrapped in PTFE was also tested. An integrator was used to shape pulses from the pre-amplifier, the same as in the above tests. A 16-element array of 3035X13 SiPMs was used in all cases.

#### 4.3.1. Measurement and Discussion

In these data and spectra, the gain of the amplifiers and SiPM were kept constant so that the channel number of the 662keV peak reflects the number of optical photons collected. As all of the crystals were CsI(Tl) and the same SiPM was used in all cases, the relative positions of the peak represent the relative light collection efficiencies. The results of these tests are shown here in Table-4.2 along with a collection of  $^{137}\text{Cs}$  spectra from each size of sphere in Figure-4.3.

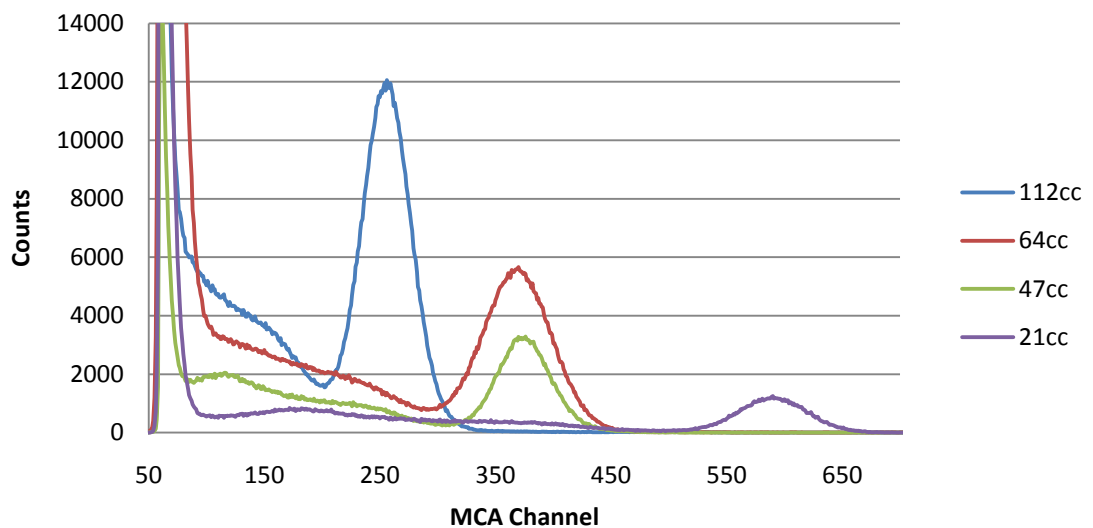


Figure-4.3: 662keV gamma-ray spectra taken with each size of sphere. Note how the 64cc and 47cc spheres appear to have the same LCE.

<b>Volume</b>	<b>Contact Area</b>	<b>Noise Floor</b>	<b>FWHM (662keV)</b>	<b>LCE (% of square block)</b>	<b>LCE (Simulated)</b>
cc	%	keV	%	%	%
112	1.7	168	18	42.5	35 ± 4
64	2.5	115	17	61.3	45 ± 3
47	3.2	110	14	65.0	47 ± 3
21	5	72	10	95.0	68 ± 3
5.5 (block)	10	72	9	100.0	80 ± 3

Table–4.2: The performance of a range of sphere sizes quantified as noise floor and energy resolution at 662keV. Also shown is the small block for comparison. The “measured” LCE is obtained by comparing the 662keV peak of each sphere with that of the small block. “Contact Area” refers to the percentage of the total crystal surface area in contact with the SiPM.

It is interesting to note that the 64cc sphere and 47cc sphere appear to have the same LCE in that the 662keV peaks are centred about the same channel and that this was predicted by optical Monte Carlo simulation (see LCE (simulated) in the table). The 47cc sphere has superior resolution however, at 14% compared to 18%. This may be due to the stalk on the 47cc sphere reducing LCE but perhaps improving uniformity. Alternatively, the 47cc sphere was sourced from a different manufacturer to the others, and so may have a slightly reduced doping concentration.

It is interesting to note that the 21cc sphere with a percentage contact area of 5% allows for noise floor and resolution at 662keV equivalent to the small block, implying a LCE of roughly 80%. The resolution at 662keV achieved with a LCE of 80% (9% at 662keV), whether that be a spherical or square crystal, is poorer than the ~7% achieved with a 10mmx10mm PIN diode [4-6] coupled to a 20cc sphere. The reason for this is again likely to be reduced photon statistics, stemming from the relatively poor PDE of SiPMs. However, a similar noise floor is achieved despite this due to the high SiPM gain, which reduces the contribution of preamp noise to the spectrum.

These results indicate that a ScintiSphere with a percentage contact area of 5% can combine the good spectral quality of a small block with superior sensitivity: the small block has a volume of 5.5cc whilst the sphere has a volume of 21cc. Table–4.3 shows the number of

counts in the 662keV photopeak when exposed to a 390kBq  $^{137}\text{Cs}$  source at 10cm for 300 seconds for each sphere and the small block.

Volume	Counts
cc	(thousands)
112	660
64	421
47	151
21	82
5.5 (block)	16

Table–4.3: The number of counts in the 662keV photopeak as measured by the range of ScintiSpheres, the small block (illuminated from the side).

#### 4.3.2. Summary

To summarise, increasing percentage contact area by reducing the size of the sphere did lead to an improvement in LCE and performance. However, even when the LCE was increased to equal that of a small square block, the goal of resolving 59keV gamma-rays could not be achieved, indicating that a reduction in SiPM noise was required to improve performance further. Whilst a 21cc sphere is more sensitive than a small block whilst achieving the same LCE, this has come at the expense of sensitivity relative to the 112cc sphere and a standard 2" NaI(Tl) detector. Also, the target noise floor of 35keV was not achieved preventing 59keV gamma-rays from being resolved. This implies that SiPMs and scintispheres are not suitable to use in the same role, but they could be useful in smaller spectrometers, where size is considered more important than sensitivity.

Comparisons with the work in section 3.3.4.1 may be drawn suggesting that a smaller SiPM array could be used to do this, as the 9-element array (10mm x 10mm) was able to resolve 59keV gammas when coupled to a 10x10x20mm crystal with LCE ~80%.

#### 4.4. Reducing Noise by Reducing SiPM Area

Given that SiPM noise scales with area, it is worth investigating whether a smaller array coupled to the same size crystal could provide an improvement in noise floor. For this test, the 21cc sphere was selected and coupled to both a 16-element array and a 9-element array of 3035x13 SiPMs. Aluminium oxide packaging was used in both cases. Noise floor was measured using 662keV gamma-rays. The results are shown in Table-4.4 along with similar data taken using square blocks.

SiPM	Crystal	Contact Area (of total crystal surface)	FWHM (662keV)	Noise floor
9-element (9x9mm)	10x10x20mm block	10%	8%	32keV
16-element (14x14mm)	14x14x28mm block	10%	9%	73keV
9-element (9x9mm)	21cc sphere	2.20%	16%	78keV
16-element (14x14mm)	21cc sphere	4.70%	10%	72keV

Table-4.4: The performance of a range of spheres and square blocks demonstrating the differences of the 9-element at 16-element array.

The noise floor of a 21cc sphere is not greatly changed by using a smaller SiPM array. This is due to the relationship between percentage contact area and LCE. Reducing the percentage contact area to 2.2% has reduced the LCE by a factor of 0.66. In contrast, the noise has been reduced by a factor of  $9/16 = 0.56$ , leading to a net increase in noise floor.

Given that there is no notable change in performance, 9-element arrays remain an alternative and may be used to reduce costs. However, it is clear that a 9-element array may only be used with a ScintiSphere of sufficiently small volume to maintain good LCE. To that end, a smaller ScintiSphere was procured.

#### 4.5. Combination of a 9-Element Array and Small ScintiSphere

In this test, a very small ScintiSphere was read out by a 9-element array. It has already been shown that 59keV gamma-rays can be resolved using a 9-element array on a square CsI(Tl) crystal of 10x10x20mm. It has also been shown that a sphere with percentage contact area 5% has comparable LCE to such a square crystal. By combining these findings, one can predict that a sphere of surface area 20cm<sup>2</sup>, a radius of 1.26cm and a volume of 8cc, when coupled to a 9-element SiPM array having an area 1cm<sup>2</sup> should provide a noise floor of ~35keV.

The intention of this test is to determine whether an appropriate noise floor and resolution for a handheld spectrometer may be achieved using a small crystal, if the array size is reduced to lower the total noise in the detector.

##### 4.5.1. Measurements

The crystal was prepared by abrading the surface until made opaque by dense scratches and then machining a circular flat of diameter 14mm into it. The flat was polished and a square glass slide of side 10mm was fitted onto the centre of this flat and bonded with MeltMount. The slide was required to provide some space between the crystal surface outside of the flat and the SiPM array. The 9-element array is built onto the same glass slide as the 16-element array and so is surrounded by a large area of empty glass, so a spacer was required to allow reflecting powder to be packed underneath it to prevent light leaks. Meltmount was also used to bond the SiPM array and the entire assembly was packed in powdered alumina as before, as shown below.

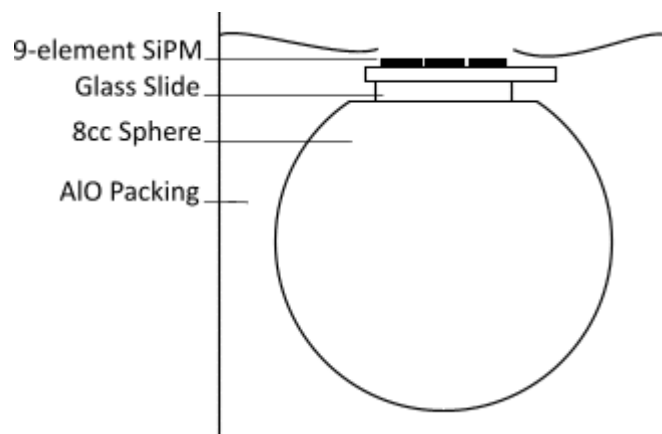


Figure-4.4: The configuration of the 8cc ScintiSphere packed in AIO and viewed through a glass slide. The glass-slide spacer was necessary due to the array being built onto an oversized glass slide.

In a parallel to previous tests, the performance of this sphere was compared to a small (10x10x20mm) block of CsI(Tl) wrapped in PTFE and coupled to the same SiPM array. Monte Carlo simulations were carried out on this sphere design and predicted a LCE of  $65 \pm 4\%$ , slightly lower than the matched block. This experiment used identical electronics for handling pulses and Figure-4.5 shows the spectra obtained using this detector. Table – 4.5 gives the energy resolutions measured over the range.

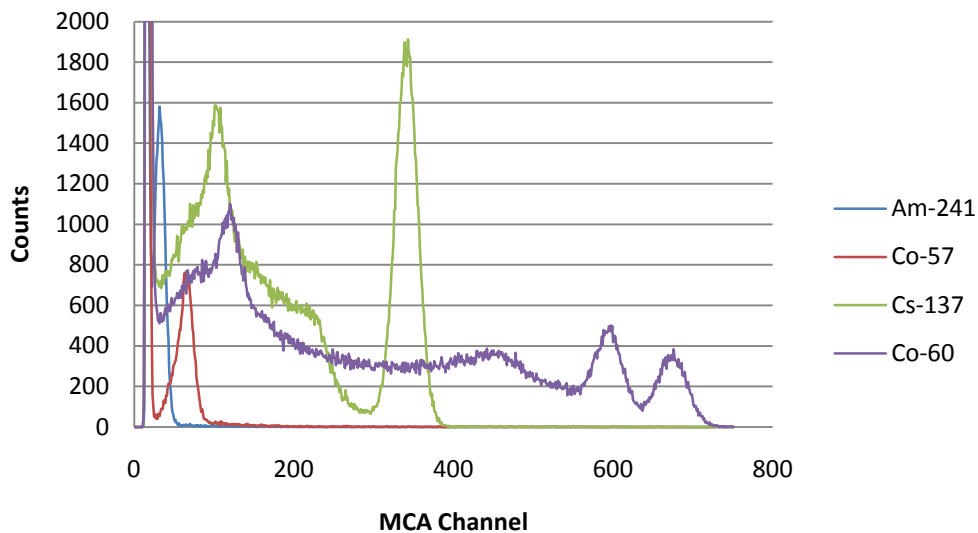


Figure-4.5: Gamma-ray spectra in the range 59keV to 1330keV obtained with an 8cc sphere and a 9-element SiPM array.

	Energy	FWHM
Am <sup>241</sup>	59keV	40.6%
Cs <sup>137</sup>	662keV	9.4%
Co <sup>60</sup>	1330keV	4.9%

Table-4.5: The energy resolutions obtained using the 8cc sphere coupled to a 9-element SiPM array.

As shown above, Am<sup>241</sup> can be resolved from SiPM noise, albeit at poor resolution. A noise floor of 38keV was achieved, as anticipated, indicating that the relationship between percentage contact area and LCE remains true for this size of array and sphere.

Energy resolution is also good, equivalent to the 21cc sphere and 16-element array at 9.5% at 662keV but slightly poorer than the 10x10x20mm block, despite the similarity in LCE. This may be attributed to poorer uniformity or perhaps experimental error. Table-4.6 shows a breakdown of the resolution terms in this detector and the total resolution compared to measurement.

$N_{\text{photons}}$	$R_{\text{stat}}$	$R_{\text{VLCE}}$	$R_{\text{intrinsic}}$	$R_{\text{SiPM Noise}}$	FWHM (estimated)	FWHM (measured)
4400	155	129	352	35	427	
	3.5%	2.9%	8%	0.8%	9.3%	9.5%

Table-4.6: The breakdown of the predicted resolution of the 8cc ScintiSphere at 662keV. Each term is expressed in the photons at the  $1\sigma$  level, except the FWHM.

The LCE and VLCE used in this calculation are those predicted by Monte Carlo simulations, and it is interesting to note that the intrinsic term dominates resolution.

The resolution achieved is good in that it matches the best achieved with the simple 10x10x20mm crystal but is still above the ~7% achieved with a 5mm x 5mm PIN diode with an 8cc sphere [4-6]. As before, reduced photon statistics will contribute, though there is also a difference in noise as the 5mm x 5mm PIN diode has 30% the area of the 9-element SiPM array.

As previously stated, LCE has been bought at the cost of sensitivity and this has been quantified by comparing the number of counts in the 662keV photopeak when exposed to a 390kBq Cs<sup>137</sup> source at 10cm for 300s to be comparable previous data taken in the same way with the larger spheres (Section 4.3.1). Table-4.7 shows the comparison between the 8cc sphere, 21cc sphere and a square block (10x10x20mm).

Volume	Counts
	(thousands)
21cc	82
8cc	21
2cc (block)	4

Table-4.7: The comparative sensitivity of two ScintiSpheres and the 10x10x20mm block, expressed as the number of counts in the 662keV photopeak of Cs<sup>137</sup>.

The 8cc sphere tested here does indeed have greater sensitivity than the small block attached to the same SiPM array (9x9mm) whilst having a very similar spectral performance. This indicates that the ScintiSphere concept has potential in the small handheld market by allowing much larger crystals than could otherwise be coupled to small photodetectors.

An ideal spectrometer has a linear response to gamma-rays so that calibration is simple and easy to stabilise against gain changes. The energy response function was measured in the range 60keV to 1330keV and linearity defined to be the deviation from a linear line taken to be a straight line passing through the origin and the lowest energy point (59keV). The linear line represents a hypothetical SiPM with an infinite number of microcells. It was found to be a curve, as expected with SiPMs, which deviated from linear by up to 5%. Table-4.8 shows the response, line of best fit and deviations. The deviation is the difference between the measured channel number and the linear line. Figure-4.6 shows a plot of that data. The linear line is defined as the line connecting the 59keV photopeak and the origin.

<b>Energy</b>	<b>Measured Peak</b>	<b>Linear Peak</b>	<b>Deviation</b>
keV	MCA Ch	MCA Ch	%
59	32	32	0.0
122	64	66	3.3
662	340	359	5.3
1330	674	705	4.4

Table-4.8: The linearity of the 8cc ScintiSphere measured as the channel number of a range of gamma-ray energies, and expressed as the deviation from a linear response. The linear response is defined as a line connecting the 59keV channel number and the origin.

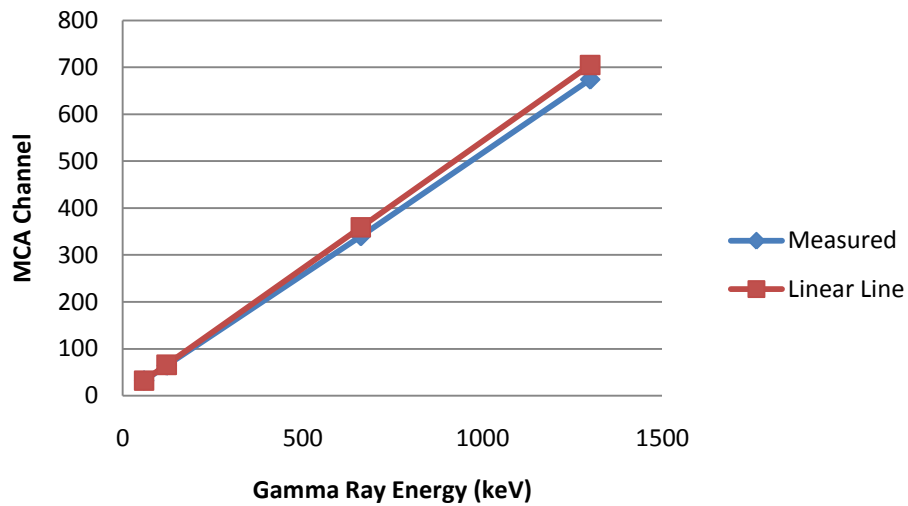


Figure-4.6: Plots of the data above. The deviation even at 1330keV is small, indicating a reasonably linear response. The linear line is defined as passing through the origin and the 59keV datum.

The response above is reasonably linear with only little deviation that can be easily described in a multiple-point calibration. The non-linearity effects inherent in SiPMs, as described in Section-2.2.5, is only slight here, likely due to the long pulse of CsI(Tl).

#### 4.5.2. Summary on Small Volume ScintiSpheres

In conclusion, using a small SiPM array (area  $1\text{cm}^2$ ) in a spectrometer is possible but only if the sphere is sufficiently small to allow high LCE. As spheres are being investigated here in the context of handheld identifiers, it is useful to compare them to 2" cylindrical crystals of NaI(Tl), prevalent in this field. An 8cc sphere has relatively poor sensitivity due to size, and this can only be improved at the expense of LCE. They may be useful in very small "pocket-sized" detectors where the advantages of SiPMs may be properly exploited: SiPMs have high gain, and it has been demonstrated that simple and cheap electronics are sufficient to allow useful energy resolution and noise floor comparable to PIN diodes of the same area. They are also robust and compact, ideal for pocket-sized detectors. Using small spheres and SiPMs in a pocket-sized device can also offer an advantage in terms of cost. Many such detectors use CZT semiconductor diodes [4-7] for their good performance at room temperature, but at the disadvantage of cost: CsI(Tl) is an established material and typically costs  $\sim \$5$  per cc, whilst prices for CZT are yet to settle down. Also, CZT may only be used in very small crystals such as  $7\times 7\times 3.5\text{mm}$  in Ref.[4-8] which limits sensitivity despite the higher density of  $5.76\text{g/cc}$  [4-9]. Small handheld systems using CsI(Tl) also exist [4-10], and they also have a noise floor around 35keV, but resolution can be expected to be worse than CZT-based systems.

#### 4.6. Use of Cooling to Improve Noise Floor

Reducing the crystal volume has increased percentage contact area and therefore improved performance, but the 59keV line of  $\text{Am}^{241}$  may only be resolved with a very small detector with low sensitivity. The reduction of noise by cooling the SiPM presents an alternative to simply using a smaller array. Therefore, the aim of this experiment was to investigate how cooling could be used to improve the performance of the 16-element array, allowing for larger spheres to be used. Larger spheres may have applications outside of pocket-sized spectrometers or dosimeters.

Thermally excited avalanches make up the bulk of SiPM noise, and an exponential reduction in dark current can be expected as the SiPM is cooled, leading to strong improvements in performance. However, the light output of CsI(Tl) peaks at 30°C [4-11] and falls off at a rate of 0.5%/°C as it is cooled below that. Therefore, only the SiPM was cooled and the crystal left at room temperature to not reduce light output.

This work was done in two stages, firstly, the measurement of how dark current varies with SiPM temperature and, secondly, the measurement of spectral performance with temperature. Spectral performance is quantified by resolution and noise floor and it is expected that the latter will scale linearly with dark current.

##### 4.6.1. Dark Current with Temperature

A 21cc CsI(Tl) sphere was read out by a 16-element SiPM array, as in Section 4.3.1. This SiPM and sphere were chosen as they offered the best performance of the detectors unable to resolve  $\text{Am}^{241}$  and would require the least cooling. A Peltier cooler was coupled to the SiPM and an aluminium heat sink. The temperature was measured by a sensor coupled to the back of the SiPM. Figure-4.7 shows the equipment used in this experiment.

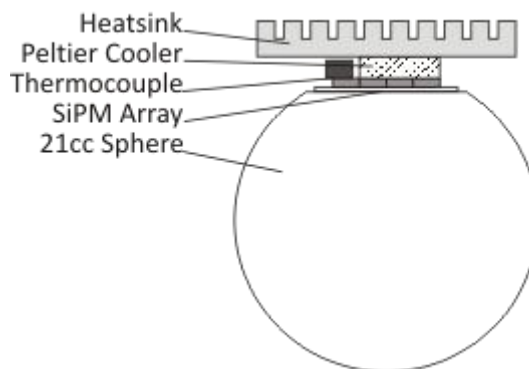


Figure-4.7: A sketch of the 21cc ScintiSphere with the cooling apparatus required to cool the 16-element array. The sphere is again packed in a can with alumina powder (not shown here)

When a SiPM is cooled, the breakdown voltage decreases, so for a set bias the overvoltage and therefore gain will increase. It is also known that the Geiger probability increases with overvoltage, and so the PDE can also be expected to increase. However, the mechanism behind the Geiger probability, that an accelerated electron will excite another electron hole pair to begin an avalanche, also applies to thermally excited electrons. Therefore, the dark current will depend on temperature for two reasons: the probability of an electron being thermally excited, and the probability of an excited electron initiating an avalanche. As the former is under investigation, it was necessary to keep the overvoltage constant by varying the bias. Doing so also maintained a constant gain.

As the SiPM was cooled, Cs<sup>137</sup> spectra were taken and the position of the 662keV photopeak was maintained in each by adjusting the bias voltage once the SiPM had thermalised. Once the overvoltage was set, the source was removed and the dark current measured. This process was repeated every 2°C between 28°C and 18°C and an overvoltage of 2.8V was maintained.

It was found that the dark current fell with temperature, halving over an interval of 5°C, as shown below in Table-4.9.

<b>Temperature</b>	<b>Bias</b>	<b>Dark Current</b>
°C	V	µA
27.3	30.07	48.9
25.3	30	42.4
22	29.87	26.2
20	29.78	18.9
18	29.66	12.9

Table-4.9: The recorded dark current as a function of SiPM temperature, taken with a 16-element array of 3035 SiPMs. The bias voltage changes also shown were required to maintain the same gain.

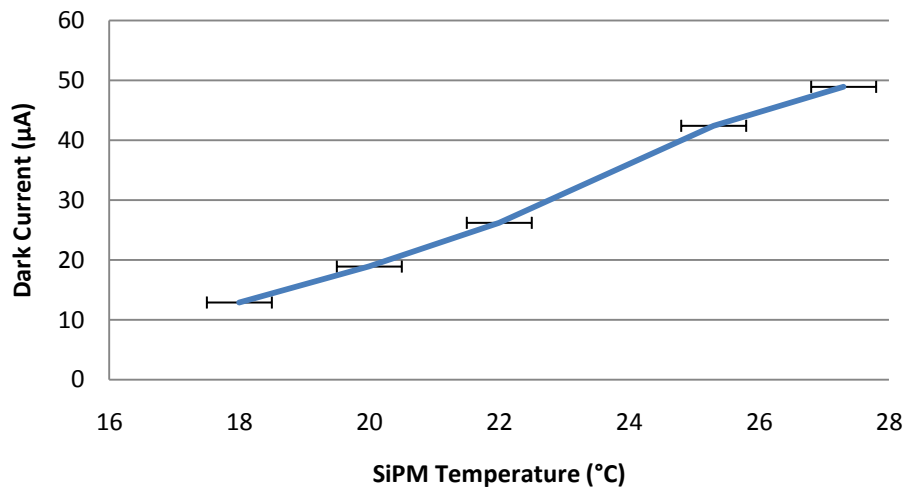


Figure-4.8: A plot of the above data, how dark current varied with temperature. The horizontal error bars are the accuracy of the temperature sensor.

Such a reduction is to be expected from a silicon device, and implies that the noise floor in a ScintiSphere will reduce at the same rate. For example, the 21cc sphere gave a noise floor of 72keV and a factor of two would bring it down to 36keV, low enough for the 59keV photopeak to be resolved.

#### 4.6.2. Measurements of How Spectral Performance is Improved by Cooling

The implication that noise floor could be halved by cooling the SiPM by 5°C was tested directly using the same equipment. In this case, however, the bias voltage was held constant and the gain was allowed to vary. The reason for this is that the gain mechanism applies equally to both noise counts and signal counts, so the noise floor will be determined solely by the relative numbers of microcells fired by noise or photoelectrons, after integration. By keeping a constant bias and allowing the overvoltage to increase, the PDE was expected to improve with cooling. Whilst this was not expected to help improve the noise floor, as thermally excited electrons will be equally likely to cause dark counts, it was expected to improve the energy resolution by improving photon statistics.

As before, the SiPM was cooled in stages and spectra taken once it had thermalised. At each stage, a background was also taken and noise floor calculated. Table-4.10 shows how noise floor and gain change with temperature.

Temperature	Peak (59keV)	Peak (122keV)	Peak (662keV)	Gain Change	Noise Floor
°C	MCA Ch	MCA Ch	MCA Ch	%	keV
27.3		24	142	0	75
22.6		29	155	9	51
21		30	174	23	49
18	14	31	183	29	36
15.2	18	35	205	44	29

Table-4.10: The peak channel numbers of a range of gamma-ray energies taken at different temperatures. The gain change is calculated based on the 662keV photopeak.

Firstly, the noise floor does indeed fall by a factor of 2.1 from 28°C to 18°C, and when cooled further to 15°C is low enough to allow 59keV gamma-rays to be resolved with a FWHM of 30%. Figure-4.9 shows Am<sup>241</sup>, Co<sup>57</sup>, and Cs<sup>137</sup> spectra laid over the background at 15°C.

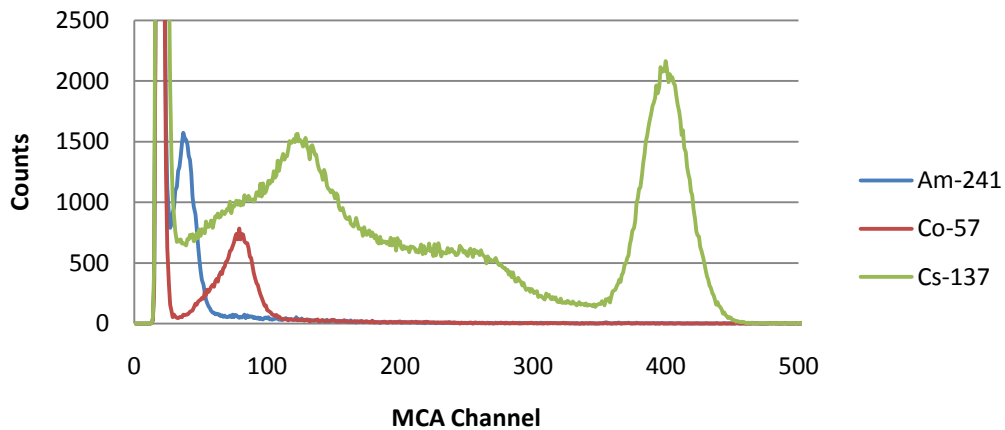


Figure-4.9: Gamma-ray spectra taken with a 21cc sphere and a SiPM cooled by 10K to 15°C.

Energy resolution improved with temperature from 13% (at 662keV) at 27°C to 10% at 15°C. This is believed to be due to the improved photon statistics from the effect of cooling on PDE, and due to the reduced dark count.

Secondly, the pulse height of the 662keV photopeak has increased to 144% over the same range, indicating a gain change of the same proportion. This change is non-linear and quite strong, an average of 4.4%/°C, which implies that a mechanism to stabilise gain against temperature changes will be needed in practical instruments based on SiPMs. A possible method is described in ref. [4-12] where an active control loop was used based on a temperature sensor and a controllable bias supply.

#### 4.6.3. Conclusion on Cooling

In conclusion, a good result has been achieved with the 21cc sphere with only moderate cooling indicating that the concept of cooling the SiPM allows for larger arrays and therefore larger crystals, possibly expanding the usefulness of SiPMs in gamma-ray spectroscopy. Based on this result, it is possible to explore how the idea can be extended to larger spheres with poorer LCE.

If greater sensitivity is desired, more cooling will be required, pushing up the power use of the detector. The 64cc sphere offers triple the volume and five times the sensitivity of the 21cc sphere (at 662keV) but has a lower LCE at 45% and a noise floor of 115keV. This means that a factor of four reduction in dark count rate is required, which may be achieved by cooling the SiPM by 20°C.

It is desirable that only the SiPM is cooled and the crystal maintained at ambient temperature for two reasons. Firstly, CsI(Tl) outputs more light when it is warm so cooling it will impair performance. Secondly, cooling the crystal will greatly increase the thermal mass maintained at 20K below ambient and the surface area through which heat can flow, greatly increasing the power required. However, an additional problem arises when cooling just the SiPM in that a thermal gradient can be set up over the volume of the crystal as heat flows from the surface to the flat where the SiPM is bonded. A thermal gradient will cause a non-uniformity of light output which will degrade energy resolution.

All of these problems can be avoided if the SiPM is thermally insulated to some degree from the sphere by a light pipe. Acrylic has a very low thermal conductivity of 0.189W/K/m and it is possible to calculate the power required to maintain a temperature gradient of 20K over a light pipe. Using the equation  $U = \frac{k \cdot A \cdot \Delta T}{x}$  where  $A$  is the cross-sectional area and  $x$  the length and assuming a cross section of 1.96cm<sup>2</sup> (equal to a 16-element array) and a length of 0.5cm, we get a power of 150mW. This is quite low, and reasonable for handheld instruments, although power is always critical in such applications.

#### **4.7. Conclusions on SiPMs in Practical Spectroscopy**

The conclusions of this study of SiPMs in the context of gamma-ray spectroscopy are somewhat mixed. It has been demonstrated that the ScintiSphere concept is essential for allowing a small photodetector to read out a much larger scintillator and that SiPMs are a viable alternative to PIN diodes in that case. Whilst SiPMs ultimately perform no better than PIN diodes in terms of noise floor and resolution due to their reduced PDE (16% to 80%), their high gain compensates for this by reducing the contribution of pre-amplifier noise. Removing the need for expensive low-noise amplifiers brings useful cost and simplicity benefits.

Efforts to develop an acceptable spectrometer with a large volume have been successful. However, it has been shown that due to the high noise of SiPMs, this may be achieved by either using small arrays (9x9mm) with small spheres (8cc) or by cooling larger arrays (14x14mm) with 21cc spheres. In the first case, spectral performance is achieved at the expense of sensitivity and in the latter, power use and complexity. Both cases place limitations on where ScintiSpheres can be useful and it is clear that if current SiPMs are to be used, then it is in only the smallest of instruments. Such instruments include personal dosimeters that use the spectral information to calculate accurate dose in real time and provide alerts to the wearer. A more advanced application would be a personal spectrometer, carried in the hand in a package little larger than a big mobile phone by first responders or security personnel. In both cases, cooling is not the preferred choice due to the power required.

#### **4.8. Potential for Future Improvement**

Ultimately, the limitations encountered are due to the immature nature of current SiPMs and can be removed by improvements in both PDE and dark count rate. Improvements in both regards are predicted to occur in the short term (at the time of writing) and higher PDE is the most important. As discussed in Section 3.2.6, improving PDE will lead to better energy resolution by increasing the number of optical photons collected. For example, increasing the PDE by 50% can be expected to improve the energy resolution of the 21cc sphere coupled to the 16-element array from 9.5% to 7.5% at 662keV.

An alternative is a S10931-50 SiPM from Hamamatsu. It possesses a stated PDE of 40% at 550nm [4-13]. This compares favourably to 18% at 550nm with a SensL 3035X13 SiPM. Array packaging is not as mature leading to a 55% packing factor, reducing the effective PDE at 550nm to 21%. Dark count rate is broadly similar at 8MHz per 9mm<sup>2</sup> SiPM.

It should also be noted that Hamamatsu do not reject afterpulses and crosstalk when measuring PDE. A study by Ward and Vacheret [4-14] found that these effects increase the PDE by 30% (relative) so that the PDE at 550nm can be taken to be 16%. Bonanno et al [4-15] found different results with a S10362 with 100micron microcells, where the PDE at 550nm was found to be 16%. Including a 53% packing factor reduces this to 8.5%. Therefore, Hamamatsu SiPMs are not well suited to viewing CsI(Tl).

Further improvement is likely to require a reduction in the dark current and could allow spheres of up to ~100cc to be used, to the point where sensitivity and resolution can be compared to 2" NaI(Tl) crystals. Predictions of this nature should be made with caution, however, as it will be difficult for SiPMs to become an alternative to PMTs due to the very low noise of the latter.

As a final conclusion, it is true that current SiPMs are found to be useful alternatives to PIN diodes with further advantages and that useful gamma-ray detectors may be built using them by exploiting the ScintiSphere concept. Whilst the range of applications of such instruments is limited by the immaturity of current SiPMs, improvements can be expected in the short term that will allow them to move into applications that require greater sensitivity, although it is not anticipated that using SiPMs with ScintiSpheres will allow them to be an alternative to PMTs.

## 5. Neutron Detection Using SiPMs

### 5.1. Introduction

Neutron detectors are used in fundamental physics, the nuclear power industry, and defence. The defence field includes nuclear non-proliferation, counter smuggling and first response. Each field places different demands on the detectors used. For example, reactor instrumentation is exposed to fluxes of the order of  $10^{11}$  n/cm<sup>2</sup>/s [5-1], requiring a very fast or current mode response to prevent dead times from reducing the count rate in the detector. In contrast, sensors in security applications can expect to encounter very few neutrons so sensitivity is paramount. Handheld detectors for security applications require high sensitivity and must be designed within strict size and weight constraints so high efficiency is essential. In security applications, neutron detectors are useful for detection of Special Nuclear Materials (SNM) such as enriched uranium, californium and plutonium. In the case of uranium, the principal gamma-ray emission is at 180keV, which can be easily shielded. Fast neutrons from fission decays are not easily shielded, and so neutrons are a key indicator of SNM. In this chapter, the use of SiPMs in a small neutron detector for use in handheld sensors is explored.

Gamma-ray rejection is essential in all cases as neutrons are almost always accompanied by gamma-rays. In reactor instrumentation, gamma-rays would give false neutron count rates and in security applications, cause unnecessary searches for neutron sources such as fissile material.

Spontaneous fission sources are commonly used in the laboratory, typically Cf<sup>252</sup> due to its high spontaneous fission probability. Spontaneous fission is also responsible for a small fraction of the neutron background, specifically U<sup>235</sup> in rock and concrete. Fission decays involve multiple bodies, so neutrons are emitted with a broad spectrum of energies. For example, the Cf<sup>252</sup> spectrum shown below in Figure-5.1.

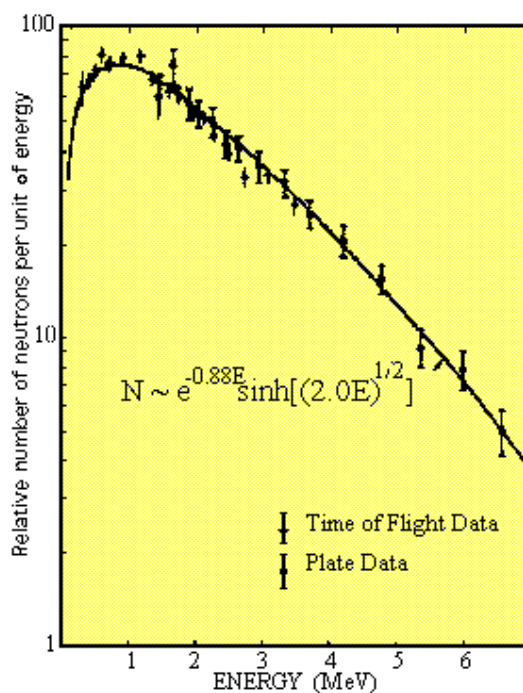


Figure - 5.1: The energy spectrum of  $\text{Cf}^{252}$  fission neutrons. Taken from [5-2].

Other lab sources exploit  $(\alpha, n)$  reactions by exposing a target, usually beryllium due to its good yield, to an alpha source, usually  $\text{Am}^{241}$ . The resultant carbon nucleus and neutron share the Q-value of 5.71 MeV along with the energy of the incident alpha, giving rise to a spectrum of neutron energies. The spectrum may be adjusted to some degree by changing the alpha source.

Cosmic rays account for the majority of the neutron background with a neutron flux of 0.015 neutrons/s/cm<sup>2</sup> [5-3]. Highly energetic particles, primarily protons above 300 MeV, collide with nuclei in the atmosphere and neutrons are present in the cascade of secondary particles along with a large part of the particle menagerie.

Cosmic rays also interact with the detectors surroundings in what is referred to as the “ship effect” [5-4], where the presence a massive body near the detector appears to increase the neutron background. Neutrons from cosmic ray showers incident on a large mass will produce further neutrons through spallation and nuclear evaporation. The quantity of extra neutrons increases with atomic number and an example of how important this effect can be is seen in Haggard where 500lbs of lead produced as many neutrons above background as 1.87g of  $\text{Pu}^{239}$  [5-5]. This effect may therefore be the source of many false alarms in the presence of buildings or large vehicles and should be taken into account when setting alarm thresholds.

The neutron background is highly variable, being determined by such factors as solar activity, diurnal position and simple weather, so care must be taken in measuring backgrounds for setting detector thresholds and also when measuring the efficiency of a neutron detector.

#### **5.1.1. Using SiPMs in Neutron Detection**

In neutron detection, SiPMs are attractive as they are not susceptible to direct gamma-ray interactions. Using PIN diodes in neutron detection is complicated by direct interaction of gamma-rays with the diodes themselves, causing large pulses which can be mistaken for neutron interactions in the scintillator. Such counts are very fast, so pulse shape discrimination may be used to separate them from genuine neutron counts, though this method introduces complication. SiPM diodes have a relatively thin depletion layer of a few microns so direct gamma-ray interactions are vanishingly likely, giving a native immunity to gamma-rays.

Given the small size, low voltage and power requirements, and robustness of SiPMs, they are well suited to portable applications. Therefore, this neutron counter shall be considered in the context of hand-portable instruments, where sensitivity must be achieved within strict volume and weight limits.

The use of a SiPM dictates that the process of converting reaction products into an electronic signal must include a scintillator. A neutron carries no charge and so will interact with matter via nuclear forces only, so the dominant interactions are nuclear capture and inelastic scattering. Therefore, all neutron detection methods rely on these reactions, principally capture.

#### **5.1.2. A Practical Specification**

A real world specification has been selected in order to test whether a neutron counter based on SiPMs can be competitive with He<sup>3</sup> tubes, which dominate this market. This specification was issued by the United States of America Domestic Nuclear Detection Office (DNDO) for a handheld isotope identifier with a neutron counter to assist in detecting enriched uranium.

DNDO specify [5-6] that a neutron counter in a handheld isotope identifier must be able to detect neutron radiation based on a  $4 \times 10^4$  n/s Cf<sup>252</sup> source located at a distance of 25cm normal to the shield surface on centreline with the source, with a detection integration time of 30 seconds or less, for the following configurations:

1. An unshielded source
2. A shielded source surrounded by 5.0cm of polyethylene

A false positive probability of 0.1% and a true positive probability of 93.5% must be achieved in the presence of a gamma-ray background. For a meaningful test of gamma-ray rejection, a gamma-ray flux must be specified and in this case DNDO specify that a handheld gamma spectrometer must work up to 100kcps. Therefore, a  $\text{Co}^{60}$  source was placed so that the flux will cause 100kcps in a 2"x2" NaI(Tl) detector, the spectrometer commonly used in such instruments.  $\text{Co}^{60}$  was chosen due to the high energy of its emissions (1.1 MeV and 1.3MeV).

Such a neutron detector must be light and small so effort should go into developing an efficient, compact design which makes the best use of its volume. The above specification should be met with the neutron detector in any orientation as a neutron source will not always be directly on axis with the detector. Therefore, it is preferable that the detector is directionally uniform.

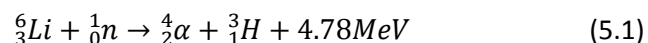
## 5.2. An Evaluation Detector

In this section, the physical principles by which the neutron counter will work are outlined and basic design decisions are made, such as which scintillator to use, how best to collect scintillation light and how to optimise sensitivity.

### 5.2.1. Choice of Scintillator

Neutron scintillators rely on a dopant or constituent element to capture neutrons and then decay, leading to heavy charged particles which then induce scintillation.  $\text{Li}^6$  and  $\text{B}^{10}$  are dominant in this field, as they possess large thermal neutron capture cross sections of 940 barns and 3840 barns, respectively [5-7], and energetic decays. A greater capture cross section is exhibited by  $\text{He}^3$  at 5330 barns but this may only be exploited in a proportional tube and so is outside of this study.

Natural lithium contains only 7.5%  $\text{Li}^6$  [5-8], so it must be enriched in order to achieve a useful macroscopic cross-section, which can be an expensive process. Lithium is used in neutron counting as it can be easily incorporated into scintillators, and can even form a metal halide scintillator using europium as an activator: lithium iodide or  $\text{LiI}(\text{Eu})$ .  $\text{Li}^6$  has a single, highly energetic reaction for thermal neutrons:



The Q-value is the total kinetic energy of the alpha and tritium shared based upon mass, and they are emitted in opposite directions so that:

$$E_H + E_\alpha = 4.78\text{MeV} \quad (5.2)$$

$$m_H v_H = m_\alpha v_\alpha \quad (5.3)$$

$$\sqrt{2m_H E_H} = \sqrt{2m_\alpha E_\alpha} \quad (5.4)$$

$$E_H = 2.73 \text{ MeV}, E_\alpha = 2.05 \text{ MeV} \quad (5.5)$$

The high Q-value of this single peak aids gamma-ray rejection, as the peak stands well above the common gamma-ray energy range (typically up to 3MeV). The light yield of LiI(Eu) is lower for heavy charged particles than for electrons: the 4.8MeV lithium decay outputs light equivalent to a 3MeV electron [5-9]. This is known as the alpha/beta ratio of the scintillator, quantifying the different light yields for the two particles. In the case of LiI(EU) it is  $\frac{3}{4.8} = 0.63$ . This is still sufficiently high for effective gamma-ray rejection. LiI(Eu) has a light yield of 11000ph/MeV [5-10] for gamma-rays; whilst this is low compared to NaI(Tl) or CsI(Tl) it is only necessary to resolve a single peak so light yield is not a critical concern.

In a more practical sense, using lithium iodide is complicated by the fact that it is difficult to grow and is highly hygroscopic, so it must be hermetically sealed and viewed through a glass window.

Lithium can also be used as a dopant in glass in the form of an oxide with a cerium activator to create an alternative scintillator with similar sensitivity to thermal neutrons. Lithium glass is widely used in neutron counters where durability is desired, being resistant to high temperatures, relatively robust and not hygroscopic. It is used as a fast neutron detector and for oil well logging. It is available in a large range of shapes and sizes, including long fibres. It is also available with differing concentrations of lithium-6 in the lithium oxide, natural (7.5%), enriched (95%) and depleted (0.1%), depending upon application. As the intention is to count thermal neutrons, only enriched lithium will be considered. Lithium glass is roughly half as bright as LiI(Eu) and it is better matched to PMT readout than SiPM readout due to a peak emission at 395nm.

The alternative to  $\text{Li}^6$  in scintillators is  $\text{B}^{10}$ , made attractive by its greater cross-section of 3840 barns and higher abundance in natural boron. It is not necessary to enrich boron for those reasons, avoiding an expensive process. Whilst  $\text{B}^{10}$  is typically used in proportional tubes, it can also be used as a dopant in existing scintillators. Boron oxide may be mixed with zinc sulphide to exploit the high light output of the latter. However, zinc sulphide is only available as a powder and so is opaque to its own light and can only be used in screens no more than a millimetre thick. The attenuation of scintillation light does not allow for a distinct peak so neutron counts can be lost amongst gamma-rays and photodetector noise. Decay fragments

are attenuated in the grains of boron oxide resulting in a range of energies if they reach the zinc sulphide scintillator, compounding the optical attenuation problem.

Table-5.1 shows the scintillation characteristics and thermal neutron attenuation length for the neutron scintillators described. Also shown is the PDE of an 3035X13 SiPM at the peak emission wavelength. For the sake of easy comparison, the number of photoelectrons collected during a thermal neutron capture by an 3035X13 SiPM is calculated for each scintillator on the assumption of 50% light collection efficiency.

		<b>Lithium Iodide (LiI(Eu))</b>	<b>Lithium Glass (GS20)</b>
<b>Q-value</b>	MeV	4.8	4.8
<b>Attenuation length (1/e)</b>	cm <sup>-1</sup>	0.06	0.16
<b>Light Output (Neutron)</b>	ph	6875	1250
<b>Light Output (Gamma)</b>	ph/MeV	11000	4000
<b>Alpha/Beta Ratio</b>		0.63	0.31
<b>Emission Peak</b>	nm	470	395
<b>Decay Time Constant</b>	ns	1400	50 - 70
<b>PDE at peak</b>	%	18	9
<b>Photons Detected</b>	ph	2970	270

Table-5.1: The key properties of the two lithium-based scintillators useful in thermal neutron detection. [5-11], [5-10], [5-12], [5-13],

Lithium iodide gives the greatest number of photoelectrons and therefore potentially the best energy resolution, useful for distinguishing gamma-rays and neutron captures. It is also the most sensitive to thermal neutrons, required for good sensitivity, in that a few millimetres of LiI(Eu) is fully attenuating. However, it is also by far the slowest scintillator, so more dark noise counts can be expected. LiI(Eu) is highly hygroscopic and so must be encapsulated.

Lithium iodide was chosen for this neutron counter on the grounds that it would provide a well resolved thermal neutron peak, well separated from gamma-ray background and SiPM noise background by the large Q-value of the reaction, requiring no sophisticated discrimination technique. A very clean spectrum and simple gamma-ray rejection method are helpful at this stage to assist in understanding the characteristics of the detector in question.

Lithium glass was rejected initially for its poor spectral match with SiPMs and low light output. Lithium glass shares many good characteristics with lithium iodide, such as a high Q-value, and a short attenuation length only a few millimetres of glass is required for total attenuation of thermal neutrons. It is also not hygroscopic, so no detector volume is lost to a can and window. It is for this reason that its use is explored later in Section 5.5.1.

### 5.2.2. Neutron Moderation

Sensitivity is critically dependent upon neutron capture so it is necessary to increase the capture cross section to improve sensitivity. Capture cross sections are always greater at lower neutron energies, falling off proportionally to the reciprocal of neutron velocity [5-14]. A typical neutron source such as  $\text{Cf}^{252}$  emits neutrons in the range of a few MeV, so a neutron moderator is required to slow them down. Moderation is achieved using the elastic scattering of incident neutrons off nuclei in a solid material, causing them to deposit energy. Neutrons scattering off nuclei may transfer energy in the following distribution:

$$E_R = \frac{4A}{(1+A)^2} (\cos^2 \theta) E_n \quad [5-15] \quad (5.6)$$

Where  $E_n$  is the incident neutron energy,  $A$  the atomic number of the scattering nucleus, and  $\theta$  the angle through which the neutron is scattered. This collision is shown in Figure-5.2.

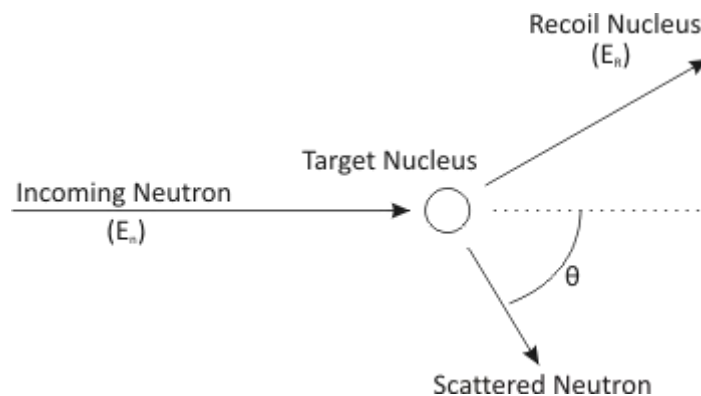


Figure-5.2: The inelastic collision of a neutron with a nucleus.

$E_R$  is minimised in grazing incidence cases, where the incident neutron is only slightly deflected and the proton recoils almost perpendicularly to it. In such cases  $\theta \approx 90^\circ$  and  $E_R \approx 0$ . On the other hand, when  $\theta \approx 0^\circ$  a 'head on' collision occurs and the recoil energy is greatest:

$$E_{(R|max)} = \frac{4A}{(1+A)^2} E_n \quad (5.7)$$

From this we see that if the target nucleus is hydrogen, then  $E_{R|_{\max}} = E_n$ : half of the neutron's energy may be imparted to the nucleus. It is for this reason that materials rich in hydrogen are used as moderators, popular choices being water (in nuclear power), paraffin and high density polyethylene (HDPE), depending upon application.

HDPE was chosen for this study on the grounds that it is easier to handle and machine than paraffin wax whilst still being very cheap.

Ideally, neutrons will undergo numerous collisions until they are reduced to thermal equilibrium with the moderator itself. Assuming that the moderator is at 300K, the thermal energy and so the mean neutron energy is:

$$\frac{1.38 \times 10^{-23} \text{ J/K} \times 300 \text{ K}}{1.6 \times 10^{-19} \text{ J/eV}} = 0.026 \text{ eV} \quad (5.8)$$

Thermal neutrons have such low energy that once captured by lithium-6, the Q-value will dominate the kinetic energy of the decay particles. Therefore, a pulse height spectrum from lithium iodide will show a single peak at 4.8MeV and represent no spectral information about the source.

A moderated neutron has also lost its incident direction, unlike a gamma-ray, so the neutron counter must have non-uniform sensitivity with direction in order to locate a source. This has a strong influence on the counter design, as some form of neutron shield would be required to collimate the detector.

It is by inelastic scattering that neutron counting can be complicated by the laboratory surrounding the counter. Low-Z materials such as wood or plastic will scatter neutrons and so contribute to the total neutron count by acting as radiators on low energy neutrons when in the presence of a source. Therefore, the amount of such materials immediately around the detector should be minimised to ensure accurate counting.

### 5.2.3. Summary

Based on the choices made above, this detector concept uses HDPE to thermalise neutrons so that they may be captured by lithium-6 in a disk of LiI(Eu) scintillator. Scintillation light is to be collected by a SiPM to explore whether they offer any advantages over other photosensors.

### 5.3. Detector Design

Before an initial design of neutron counter can be finalised, effort must be spent on two design tasks: the optimisation of LCE and the arrangement of HDPE moderator around the scintillator. Once the first task is complete, the scintillator, light guide and SiPM will form a neutron counting core around which moderator can be arranged. The design of this core is independent of the moderator configuration, as it is driven by the need to efficiently transmit scintillation light to the SiPM, thus it should be designed first.

#### 5.3.1. Optical Design Constraints

A LiI(Eu) scintillator was sourced from Scionix (Netherlands) in the largest size available: a 22mm diameter disk of thickness 3mm. It is packed into an aluminium can with a white reflecting powder and hermetically sealed with a glass window. The total package is 29mm in diameter and 8mm thick and the glass window extends mostly across the front face. A cross-section of the package is shown in Figure-5.3.

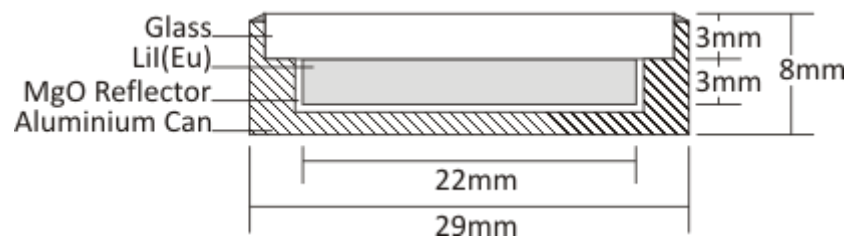


Figure-5.3: A cross-section of the scintillator package from Scionix. Though not shown in the figure for clarity, the base of the can is 2mm thick and the reflector is 1mm thick.

No SiPM arrays of this size exist, so a light guide was required to couple a circle of  $707\text{mm}^2$  to a square of  $196\text{mm}^2$ . This output area is the area of a 16-element array of  $3035 \times 13$  SiPMs, chosen to maximise the ratio of output area to input area. Any light pipe with a reducing cross section along its length will not be perfectly efficient since the number of photons per unit area per solid angle cannot be greater at any point than at the input. Therefore, LCE is typically limited by the ratio of input area to output area. Any light guide must interface with the entire glass window in order to collect a satisfactory fraction of the scintillation light.

Unlike a prismatic light guide, we cannot rely on total internal reflection to carry the light to the SiPM so the light guide must be packaged in a reflective material. In a tapered light guide, a specular reflector will reflect light away from the SiPM. Diffuse reflection is therefore

preferred and may be achieved with densely packed white powder or PTFE tape. Results from testing ScintiSpheres indicate that aluminium oxide powder is a superior reflective material to PTFE tape but was deemed unsuitable since the required container would waste volume and raise handling difficulties.

### 5.3.2. Optical Simulations

Since the monoenergetic 4.8MeV peak needs to be resolved from SiPM noise and gamma-rays, a good LCE and uniformity are required. Therefore, the optical characteristics of the light guide and crystal assembly were simulated using an optical Monte Carlo simulation to predict how these properties vary with light guide length.

It was assumed that the light guide was wrapped in PTFE having reflectivity 95% and that the crystal was packaged in diffuse reflecting powder having reflectivity 98%.

Simulations were carried out in a similar manner as with ScintiSpheres in that an isotropic flash of optical photons was placed at a range of different locations within the scintillator and the number of photons reaching the SiPM surface was recorded. Because the crystal was so thin, the flash was only moved in two dimensions. The mean of this range of numbers is the LCE and the one sigma deviation the non-uniformity (or VLCE).

In this simulation, the scintillator packaging and light guide were defined as shown in Figure-5.3. The light guide is intended to couple a circle to a square, a complicated shape not readily available in Geant4, so it was approximated by a truncated cone with an output surface area of  $196\text{mm}^2$  to preserve the ratio of input area to output area. A hollow cone was defined around the light guide to represent the reflector.

Table-5.2 shows the simulated LCE and VLCE for a range of light guide lengths. Also shown are the statistical term and VLCE (at  $1\sigma$ ) term predicted for each length, to provide a metric for choosing one above the others. Figure – 5.4 shows a plot of the VLCE and LCE for the range of light guide lengths considered.

Light guide length	5mm	10mm	15mm	20mm	25mm	30mm
LCE (%)	55.52	48.80	43.26	39.17	35.22	31.67
VLCE ( $1\sigma$ ) (%)	1.42	0.64	0.68	0.37	0.53	0.41
$N_{ph}$	4506	3961	3512	3180	2859	2570
$R_{stat}$ (%)	1.5	1.6	1.7	1.8	1.9	2.0
$R_{VLCE}$ (%)	2.6	1.3	1.6	0.9	1.5	1.3
$R_T$ ( $1\sigma$ ) (%)	3.0	2.1	2.3	2.0	2.4	2.4

Table-5.2: The results of optical simulations of the scintillator shown in Figure-5.3 and a light guide. For each length of the light guide, the light collection efficiency (LCE) and its uniformity (VLCE ( $1\sigma$ )) are given.  $N_{ph}$  is the number of photons predicted to be collected by the SiPMs. The contributions of photon statistics and uniformity to energy resolution at 4.8MeV are given.

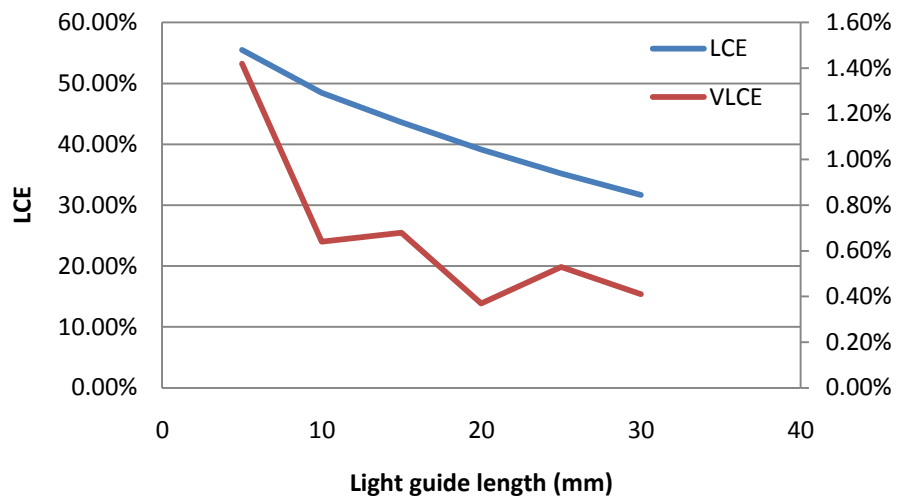


Figure – 5.4: Plots of the LCE and VLCE with increasing light guide length.

Light collection efficiency improves for shorter light guides, as expected, since the SiPM subtends a greater solid angle as viewed from the scintillator, so fewer photons are reflected randomly about the light guide. However, the uniformity (VLCE) is far worse for the same reason: reflecting the light multiple times integrates it and leads to good uniformity, much like a ScintiSphere. In a short light guide, the poor uniformity dominates resolution whilst in a long light guide, the poor LCE does and an optimum point exists between the two, though it is a

shallow trough. This implies that the energy resolution will not depend strongly on light guide length, unless it is very short.

Based on these simulation results, a 15mm long acrylic light guide was chosen as it sits in the middle of the shallow minimum and allows a compact detector to be made. The light guide was formed by turning a cone of PMMA and then cutting flat surfaces onto it to produce a square section at the narrow end of 196mm<sup>2</sup>.

Based on this simulated LCE and VLCE and the known dark count rate of the 16-element SiPM array, it is possible to predict whether the optical performance of the detector and the separation of the neutron peak (4.8MeV) from gamma-rays at 1.3MeV. The intrinsic term ( $R_{int}$ ) was taken from reference [5-11] which covers gamma-ray spectroscopy with LiI(Eu). This paper reports the intrinsic term to be quite small and decreasing with energy. Figure-5.5 shows the plots of energy resolution,  $R_{stat}$  and  $R_{int}$  for LiI(Eu) for a range of gamma-ray energies.

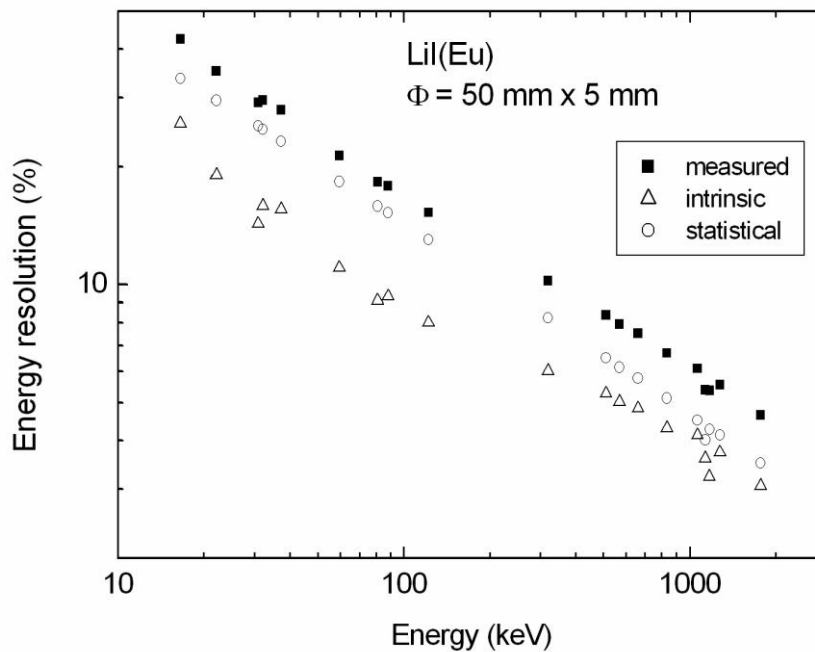


Figure-5.5: Plots of energy resolution terms for LiI(Eu) up to 1.1MeV. (Taken from [5-11]).

Note how the intrinsic term decreases with energy and will need to be extrapolated for 1330keV Co<sup>60</sup> gamma-rays. Taking the linear line along this plot above indicates an intrinsic term at 1330keV of 0.5%. No data is available for the intrinsic term for the thermal neutron peak, so the term is omitted when the resolution of that peak is predicted.

The resolution of both peaks was calculated and compared to the number photons collected in each to determine the resolution, the results are shown below in Table-5.3.

	Peak	R <sub>stat</sub>	R <sub>VLCE</sub>	R <sub>int</sub>	R <sub>DR</sub>	R <sub>T</sub> (1s)	FWHM
	ph	ph	ph	ph	ph	ph	%
Thermal neutrons	2575	51	47	0	18	72	6.5
Gamma rays	1107	33	20	6	18	43	9.1

Table-5.3: The breakdown of energy resolution for both the 4.8MeV neutron capture peak and 1330keV Co<sup>60</sup> gamma-ray photopeak in LiI(Eu). The LCE was assumed to be 43.3% with a VLCE of 0.68%.

In reference [5-11] a resolution of 3.9% is achieved for the thermal neutron peak by coupling a 30mm x 3mm LiI(Eu) crystal from Scionix to a PMT through a glass window. Such good resolution was achieved by a good LCE, likely to be ~70-80%, compared to 43%. It is anticipated that even if the energy resolution of this detector is worse than predicted, good gamma-ray discrimination should be achieved.

### 5.3.3. Moderator Design Considerations

#### 5.3.3.1. Efficiency

The chosen scintillator is totally black to thermal neutrons so the moderator design must be efficient in that it should carry as large a fraction of the incident neutron flux to the scintillator as possible whilst being small and light.

Counting neutrons by moderation and capture is inefficient, despite the high capture cross section of lithium-6 at thermal energies. Many neutrons simply do not interact with the moderator as moderation relies on collisions with nuclei [5-16] and many are scattered once or twice without being thermalised. Once a neutron is thermalised, it has lost all directional information and wanders at random until captured or it escapes. Therefore, there will be a thermal neutron flux within the moderator volume and a scintillator that is black to thermal neutrons will capture whatever fraction of that flux enters its volume. For this reason, the design of the moderator is important to the sensitivity of a neutron counter.

Firstly, a moderator is typically much larger than the scintillator within and so acts as an “antenna”, where incident neutrons that would otherwise miss the scintillator scatter off nuclei in the moderator and these neutrons, once thermalised, may wander into the

scintillator. The larger the moderator, the more likely a neutron is to collide with a nucleus as it passes through and the more sensitive the counter will be. Also, the mean number of collisions a neutron will have is increased so the mean energy is decreased, leading to a higher capture cross section. By this mechanism, increasing the size of the moderator can increase sensitivity.

However, simply increasing the moderator thickness is not without complications. Two mechanisms exist causing losses in the thermal neutron flux: hydrogen activation and geometric losses. The former case is where hydrogen nuclei capture thermal neutrons to create deuterium and a 2.2MeV gamma-ray. The latter case is more involved. As a moderator is enlarged, more neutrons will be thermalised farther away from the scintillator which will occupy a smaller fraction of the total volume. Therefore, it is less likely that a neutron thermalised at some far-flung point in the moderator will ever reach the scintillator, leading to decreasing returns.

Therefore, for any given neutron energy there is an optimum moderator thickness, below which too few neutrons are moderated to thermal energies and above which too many thermal neutrons are absorbed or simply lost. Figure-5.6 shows the three loss mechanisms in a large spherical moderator around a spherical scintillator.

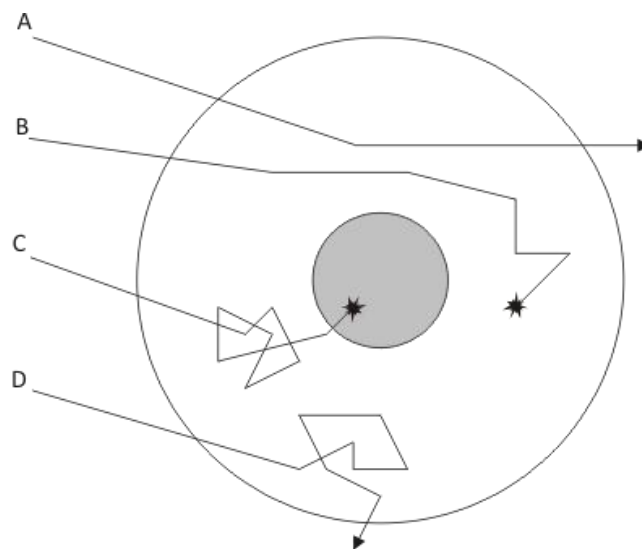


Figure-5.6: A scintillator shown in grey within a white HPDE moderator with four possible neutron paths. Neutron A scatters once in the moderator and leaves without reaching thermal equilibrium. Neutron B scatters until it is thermalised and then is captured by hydrogen in the moderator. Neutron C also thermalises and then wanders into the detector and is counted.

Neutron D also thermalises but wanders out of the moderator and is lost.

From the above discussion, we can draw some conclusions about moderator design. To reduce geometric losses (path D above), the scintillator should occupy a considerable fraction of the counter volume and as much of the moderator should be as close to the scintillator as possible, so efficient use of volume is essential. Path A may be avoided by having a large moderator volume, though this will come at the expense of path B and path D becoming more common. Attention should be paid toward the size of the moderator, where the trade-off between fast neutron attenuation and losses to hydrogen activation and geometry takes place within strict volume and weight restrictions.

### **5.3.3.2. Directional Uniformity**

A directionally uniform neutron counter is desired so that the sensitivity requirements in the specification are met for any orientation of the detector axis relative to the source.

For an efficient detector, that is, one that contains no wasted volume and air gaps, the sensitivity is determined loosely by the area presented to the source and the depth. Once moderated, neutrons lose their directional information, so the orientation of the lithium iodide crystal within the moderator is less relevant.

Therefore, a useful rule of thumb to design a directionally uniform neutron detector is to ensure that the area presented to the source and the moderator depth are roughly constant regardless of orientation. A spherical moderator presents itself, much like a Bonner sphere [5-17], but it can be difficult to machine and presents complication. An approximation may be achieved with a cylindrical moderator, if the cross-sectional area is set to be equal to the side area. That is:  $\pi r^2 = 2rl$ , where  $r$  is the radius and  $l$  the length.

### 5.3.4. Moderator Design for an Evaluation Device

Based upon the above discussion, a simple moderator configuration around the scintillator package was simulated and tested. Figure-5.7 shows the moderator design. Other properties are given, including the volume of the crystal expressed as a fraction of the total detector volume.

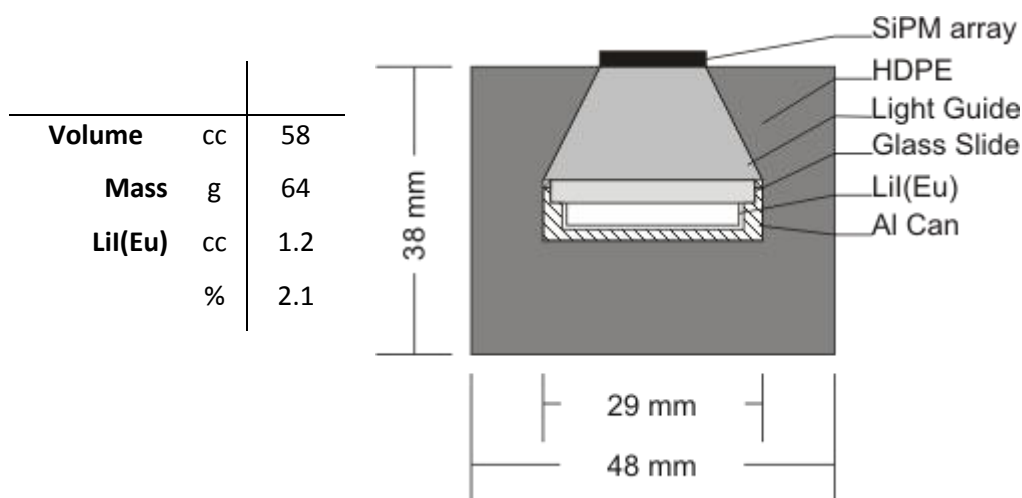


Figure-5.7: A sketch of the neutron detector tested here. On the left are some properties including the volume fraction of the Lil(Eu) scintillator itself.

A moderator depth of 15mm was chosen to match the length of the light guide so that the SiPM array could be fitted onto the rear surface of the detector. This is because the SiPM array has a broad border of glass and a Molex connector which would not allow close fitting of the moderator around the light guide. As the light guide is acrylic it may also be used as a moderator and by doing so, the total moderator thickness is more uniform around the crystal and gaps are minimised.

The width of the moderator has been set to improve uniformity based on the argument in Section 5.3.3.2, giving a total volume of 58cc.

### 5.3.5. Sensitivity Simulations

Simulating the response to a broad continuum of neutron energies is more complicated than monoenergetic gamma-rays. In this simulation, the  $\text{Cf}^{252}$  spectrum (shown in Figure-5.1) is divided into slices of width 100keV. For each slice, the mid-point energy (50keV, 150keV, etc.) is given to neutrons emitted from a point source and the detector response recorded. The process is iterated up to neutron energies of 4MeV and the detector responses are folded with the  $\text{Cf}^{252}$  spectrum.

It is important to accurately describe the detector in the model to ensure results that can be compared to real data. As all material near the crystal will scatter neutrons to some degree every component was included in the simulation. The packaging around the crystal was defined as in Figure-5.3 with the reflector assumed to be MgO powder. The moderator configuration was defined as shown in Figure-5.7. The HDPE shield was also defined as a cube of side 10cm centred on the source to match the physical shield used in the laboratory. The source was placed at 25cm from the centre of the crystal on axis with the detector.

The response of the detector was simulated both with and without the shield and the predicted performance is shown here in Table-5.4. These simulations indicate that the detector will be far more sensitive to a shielded source, implying that too little moderator is used.

Shielded	Bare
5.28 n/s $\pm$ 0.13 n/s	0.41 n/s $\pm$ 0.04 n/s

Table-5.4: The predicted performance of the neutron detector for a shielded and unshielded  $4 \times 10^4$  n/s  $\text{Cf}^{252}$  source. The errors are at the  $1\sigma$  level and are calculated as the statistics error in the number of neutron counts over 300s.

## 5.4. Evaluation Detector Testing

### 5.4.1. Measurement of Optical Performance and the Pulse Height Spectrum

Good optical performance is essential for gamma-ray rejection as the thermal neutron peak should be distinct from any gamma-ray counts. To test the optical performance, and gamma-ray rejection the detector was exposed to neutrons from  $\text{Cf}^{252}$  and gamma-rays from  $\text{Co}^{60}$ .

The scintillator package was bonded to the light guide with silicone grease and then wrapped in  $\sim 16$  layers of PTFE to provide reflection. PTFE was chosen for its high reflectivity and convenient handling properties. Silicone grease (BC-430) was also used to bond the SiPM, light guide and scintillator together. The SiPM array used was 16 elements of 3035X13 SiPMs from SensL.

To produce a pulse height spectrum, the same preamp as used in Chapter 4 was used and the pulses passed to the same integrator, as  $\text{LiI}(\text{Eu})$  has a similar length pulse to  $\text{CsI}(\text{Tl})$ . The shaping time was set to  $2.2\mu\text{s}$  to ensure good charge collection and attenuation of noise pulses. To shield from electronic noise, the counter and amplifiers were kept within an

aluminium case. Figure-5.8 shows pulse height spectra obtained from the LiI(Eu) crystal when exposed to  $\text{Co}^{60}$  or  $\text{Cf}^{252}$ .

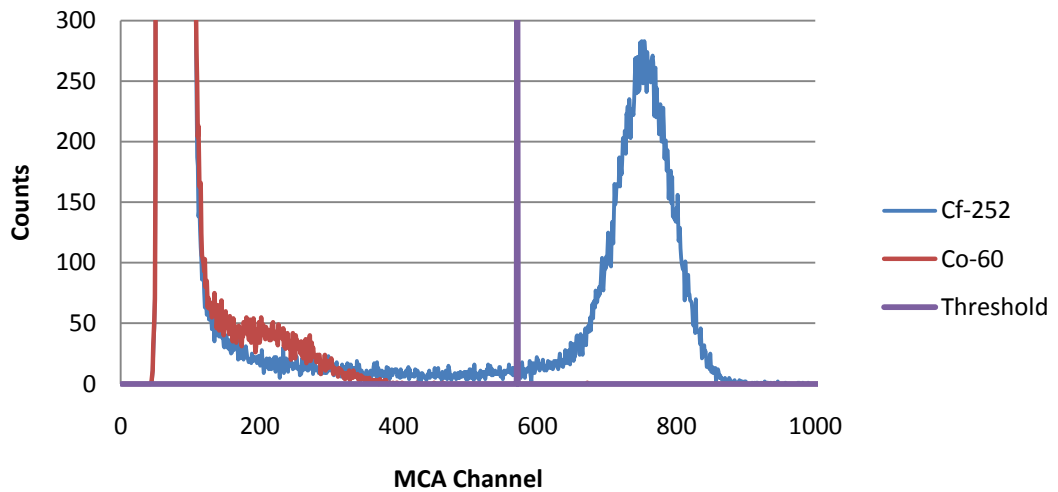


Figure-5.8: Pulse height spectra of thermal neutron captures and  $\text{Co}^{60}$  gamma-rays. Also shown is the energy threshold, above which all counts are considered neutrons, a simple rejection method made possible by the high Q-value of  $\text{Li}^6$ .

Due to the poor scintillation performance of LiI(Eu) relative to CsI(Tl), particularly in terms of light yield and intrinsic resolution, the two peaks of  $\text{Co}^{60}$  could not be resolved and only the 1330keV peak partially stands above the noise.

The thermal neutron peak is clearly separated from the gamma-ray spectrum and SiPM noise and is well resolved at 11% FWHM. This resolution is somewhat worse than predicted, indicating either that the intrinsic term is a strong contributor to resolution or that the optical Monte Carlo simulation underestimated the VLCE. If we take the VLCE term to be correctly simulated, then the intrinsic term can be calculated to be 9.1% at  $2.35\sigma$ , or 3.9% at the  $1\sigma$  level.

Exploiting this clear separation, neutrons may be counted and gamma-rays rejected by setting a threshold above which all counts are accepted. A threshold of  $6\sigma$  below the neutron peak was selected to encompass the entire peak and the number of counts above the threshold in gamma-ray spectra was compared to background spectra.

The specification calls for effective gamma-ray rejection in a gamma-ray field sufficient to cause 100kcps in a 2" NaI(Tl) detector. This flux was achieved by placing a  $10\mu\text{Ci}$  source at

6cm. A 2.3cm diameter LiI(Eu) crystal of thickness 0.3mm would have a surface area of  $4.2\text{cm}^2$  and an interaction efficiency of 5.9%, leading to a gamma-ray count rate of 200cps at 1300keV

A “false neutron” count rate of 0.04cps was measured both with and without the gamma-ray source, indicating excellent gamma-ray rejection in this flux. This allows neutron counting to be performed by very simple electronics, merely counting pulses above a threshold, which keeps cost and signal processing overheads low.

In conclusion, the optical performance of the light guide and SiPM is more than sufficient to allow effective gamma-ray rejection up to a count rate of 200cps, and it is expected that the gamma-ray flux could be increased further without any detrimental effect.

#### **5.4.2. ROC Curve Analysis as a Tool for Judging Sensitivity**

The specification stipulates a true positive probability of 93.5% and a false positive probability of 0.1% within 30s. Before the sensitivity is measured, it is necessary to understand how the background count rate and the source count rate relate to these probabilities and how alarms are generated. This is done using ROC (Receiver Operating Characteristic) curve analysis which is outlined briefly here.

An alarm is generated when the number of counts in the detector as collected over a time window exceeds a threshold. This threshold must be high enough to minimise the probability that a statistical variation in background will exceed it. Poisson statistics can be used to calculate the probability of  $n$  background counts in the time window given the background count rate. Therefore, the false positive probability can be calculated for a threshold of  $n$  by summing the probability of  $>n$  counts.

The true positive probability can be calculated in the same manner, but using the count rate when the specified source is present. ROC curve analysis gets its name from the curve generated by plotting the true positive probability and false positive probability for each threshold  $n$  against each other, demonstrating the trade-off between them. The true positive probability may be increased by lowering the threshold but at the cost of increasing the false positive threshold.

Figure-5.9 shows a ROC curve generated by plotting the true positive probability against the false positive probability. Each point on the curve corresponds to a threshold. In this curve, the source count rate is twice the background count rate.

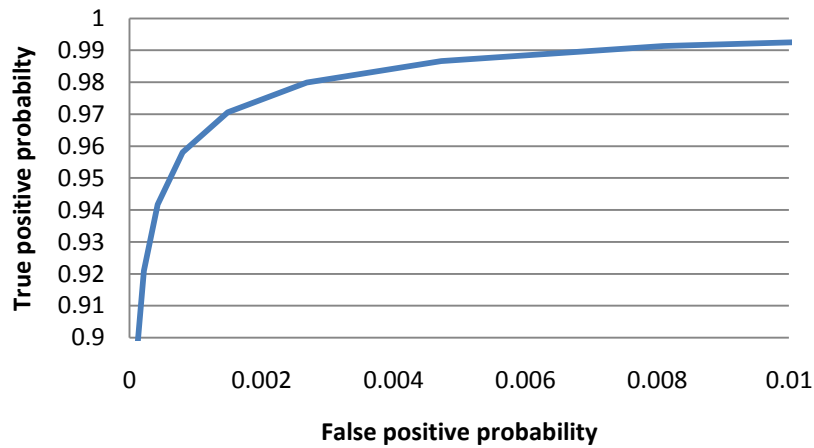


Figure-5.9: An example ROC curve describing how the false positive probability and true positive probability are both linked for a given alarm threshold and count rate.

If a point on this curve has true positive probability >0.935 and false positive probability <0.001, then the specification is met. The true and false positive probabilities depend on the number of counts collected, so performance may be improved by increasing the time window up to the specified limit of 30s. The required integration time is determined by the ratio of the source count rate to the background count rate, so the more sensitive the detector, the quicker it may alarm with confidence. Therefore, it is possible to test if the detector meets the specification by measuring the background and source count rates, generating the curve and finding if a 30s time window is sufficient.

#### 5.4.3. Sensitivity Measurements

The sensitivity of the compact neutron counter was tested against the DNDO specification using a  $Cf^{252}$  source at a distance of 25cm both with and without a 5cm deep HDPE shield. At the time of the measurements, the source activity was  $0.94 \times 10^4$  n/s so a scaling factor of 4.25 was applied. The shield was a cube of HDPE of side 10cm with the source placed at the centre, aligned with the detector's central axis. To reduce the contribution of the laboratory to the neutron count through scattering the detector and source were kept at least a metre away from any wooden lab furniture. Figure-5.10 shows the basic configuration of these tests and Table-5.5 shows the measured count rates.

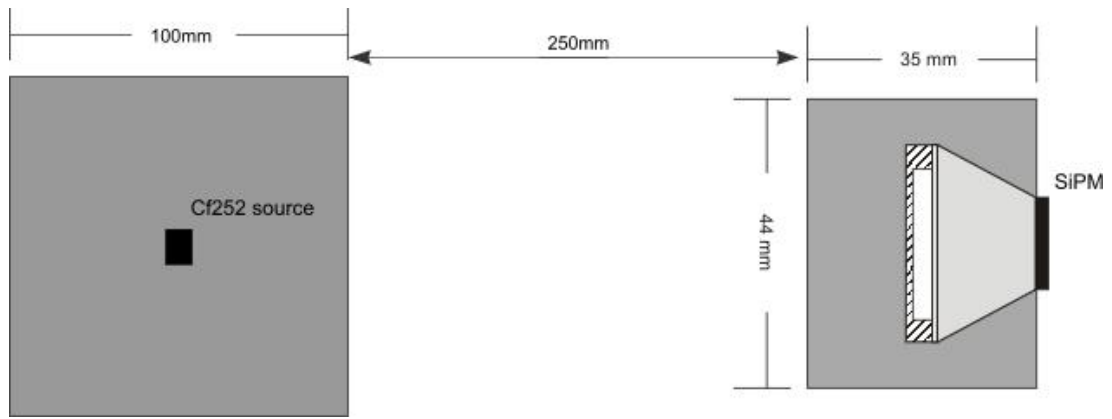


Figure-5.10: The basic configuration of the sensitivity measurements, showing the detector within its moderator and the HDPE shield surrounding the source.

The predicted sensitivity matches the measurements well when the source is unshielded, as shown in Table-5.5. However, the count rate for a shielded source is overestimated by 80%.

	<b>Shielded</b>	<b>Bare</b>
Simulated	5.28 ±	0.46 ±
	0.1 n/s	0.04 n/s
Measured	2.95 ±	0.44 ±
	0.1 n/s	0.04 n/s

Table-5.5: A comparison of the simulated and measured count rates of the LiI(Eu) neutron counter in a 38x48mm HDPE moderator.

This discrepancy may be due to Geant 4 overestimating the scattering cross section of the moderator so that the neutrons have a lower energy, or it is underestimating the capture cross section of the moderator, so that the thermal neutron flux is too high.

For the sake of comparison, a He<sup>3</sup> proportional tube was procured. The tube (LND part number SK01226) was 76mm in length and 13mm in diameter (3" by 0.5") [5-<sup>18</sup>]. This tube had a contained He<sup>3</sup> at a pressure of 15 atmospheres and had a sensitivity to thermal neutron of 9 cps/nv. Moderation was provided by 16mm of HDPE surrounding the sides of the tube, creating an efficient moderator configuration of similar thickness. It should be noted that this detector is highly directional and in this case has been illuminated from the side.

Efficiency is calculated as the percentage of neutrons incident on the detector face that are counted. The number of neutrons incident is simply the neutron flux (expressed per steradian) multiplied by the solid angle subtended by the detector as viewed from the source.

Table-5.6 overleaf shows the count rates as measured in the test and the count rates as scaled for a  $4 \times 10^4$  n/s source. Also shown are the efficiency and specific sensitivity. The “capture volume” is the volume of the He<sup>3</sup> tube and LiI(Eu) crystal themselves.

	unit	<b>LiI(Eu)</b> <b>23x3mm</b>	<b>He<sup>3</sup></b> <b>76x13mm</b>
<b>Count Rate: Shielded Source</b>	cps	2.95	5.3
<b>Count Rate: Bare Source</b>	cps	0.44	1.3
<b>Background</b>	cps	0.04	0.07
<b>Integration time</b>	s	23	6.0
<b>Volume</b>	cc	58	121
<b>mass</b>	g	64	165
<b>Capture volume</b>	cc	1.2	9.6
<b>Capture volume fraction</b>	%	2.1	8.0
<b>Specific sensitivity (shielded)</b>	cps/100cc	7.4	4.4
<b>Specific sensitivity (bare)</b>	cps/100cc	1.1	1.1
<b>Efficiency (Shielded)</b>	%	5.6	3.0
<b>Efficiency (Bare)</b>	%	0.8	0.7

Table-5.6: The measured performance of the neutron detector tested here, compared against a common He<sup>3</sup>-based detector used in a similar role. Key parameters are the count rates and the integration time required to meet the alarm specification.

Taking the count rate when exposed to a bare source as the worst case, ROC curve analysis predicts an integration time of 23 seconds for the SiPM neutron counter, well within the specified 30 seconds. Figure – 5.11 shows the ROC curve for this detector using a 23-second integration time. The curve compares the count rate to an unshielded source (the worst case) to the background.

The difference in sensitivity to bare and shielded sources in detectors is striking and implies that the shield largely moderates the neutrons. In that case, the mean neutron energy is reduced so the fraction of incident neutrons brought down to thermal energies is increased.

In spite of the likely capture of a number of neutrons in the shield, it actually improves sensitivity. This implies that a greater moderator depth than 15mm would be beneficial.

The SiPM neutron counter is less sensitive than the He<sup>3</sup> tube and this is to be expected from it being smaller, so the specific sensitivity and efficiency become useful here. In this respect, the SiPM neutron counter may be considered superior in that it is more efficient at collecting slower neutrons than the He<sup>3</sup> tube. As the moderator thickness is nearly the same in both cases, and the LiI(Eu) crystal has a smaller volume fraction, this is likely to be due to the high efficiency of LiI(Eu).

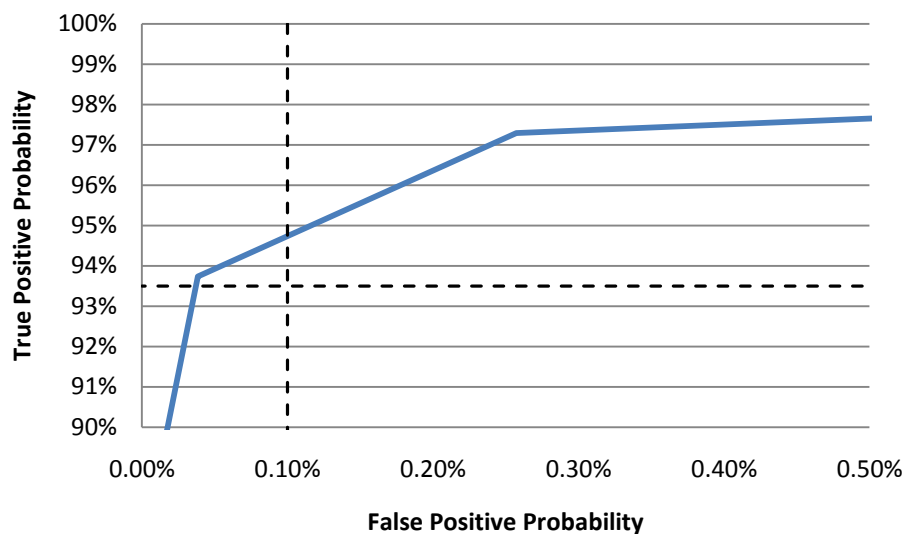


Figure – 5.11: The ROC curve for the neutron detector when exposed to an unshielded neutron source. The black lines are the specified true positive and false positive probabilities.

An integration time of 23 seconds is just sufficient for both specifications to be met

#### 5.4.4. Directional Uniformity

Directional uniformity was measured by repeating the sensitivity measurement at a range of detector orientations. The orientation was defined with respect to the source being on axis with the detector (as shown in Figure-5.10). Directional uniformity is useful in a neutron detector where the dose rate needs to be measured, as a non-uniform detector would give different measurements depending on the location of the source. The source was moved in a plane around the detector in 45° steps and the count rate measured and is given here in Table-5.7 and Figure-5.12.

Angle off boresight	Count rate	Error ( $1\sigma$ )	Uniformity
degrees	n/s	n/s	%
0	2.60	0.07	100
45	2.48	0.06	95
90	2.48	0.06	95
135	2.54	0.07	98
180	2.52	0.06	97

Table-5.7: The directional uniformity of the compact detector when exposed to a shielded source. Uniformity is expressed by giving the count rate at each position relative to the count rate at 0°.

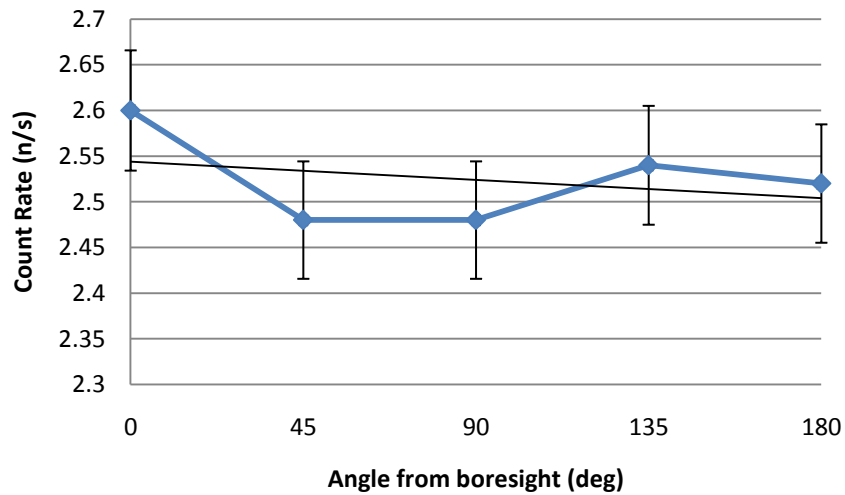


Figure-5.12: A plot of the above data with error bars set at  $1\sigma$ . The solid black line is a linear line of best fit.

The directional response was found to be uniform with all points remaining within  $1\sigma$  of each other. Uniformity is sufficiently good that rotating the detector will not cause a significant change in sensitivity, evidenced by the overlapping error bars above.

From this data, we can conclude that directional uniformity can be achieved by shaping the moderator such that the cross-sectional area presented to the source is irrespective of angle. The reduced sensitivity when illuminated from the side (90°) can be attributed to the moderator being cylindrical so the moderator depth is not equal over the area, despite the cross-section area being constant.

#### 5.4.5. Analysis of Spectral Artefacts

The LiI(Eu) spectrum is not simple in that it contains both the expected thermal neutron peak and a continuum: the origin of this continuum is of interest (see Figure – 5.7). Direct gamma-ray and neutron interactions in the SiPM are very unlikely due to the thin depletion region. Non-uniformity in the light guide can be discounted based on the distinct and well-resolved peak. It is likely to be an interaction in the crystal producing scintillation light. Several possibilities were considered:

- Excitement of iodine by inelastic scattering of neutrons resulting in gamma-ray emission
- Activation of the iodine by neutron absorption
- A competing nuclear reaction:  ${}^6_3\text{Li} + {}^1_0\text{n} \rightarrow {}^2_1\text{H} + {}^4_2\alpha + {}^1_0\text{n}$
- Gamma-rays from  $\text{Cf}^{252}$

The first and last candidates are unlikely since the observed continuum does not follow the same shape as the gamma-ray continuum and  $\text{Cf}^{252}$  only produces gamma-rays up to 900keV, which is lower than  $\text{Co}^{60}$  emissions. Iodine decays by a  $\beta$ -emission which has a cut-off energy of 2.2MeV. The competing nuclear reaction will produce a continuum since it is a three body reaction. The reaction in question is a fast-neutron reaction and becomes dominant at neutron energies above 2.2MeV and has a Q-value of -1.47MeV [5-19] In this case, 1.47MeV of the incident neutron energy is used to separate the lithium nucleus. If this is correct then one would expect the count-rate in the continuum to be greater for an unshielded source than one shielded by 5cm HDPE, as the incident neutrons will have greater energy.

For the purpose of this experiment, the continuum was defined to be the region between the SiPM noise floor (1cps) and the  $6\sigma$  energy threshold. The detector was exposed to the  $\text{Cf}^{252}$  source both with and without a HDPE shield 5cm deep and without the detectors moderator. Table-5.8 and Figure-5.13 show the resultant data.

	Peak	Continuum
Shielded Source with Moderated Detector	11.5 n/s	3.0 n/s
Bare Source with Moderated Detector	7.6 n/s	32.7 n/s
Bare Source with <i>Unmoderated</i> Detector	1.3 n/s	22.6 n/s

Table-5.8: Peak and Continuum Count-rates with Varying Moderator Configuration.

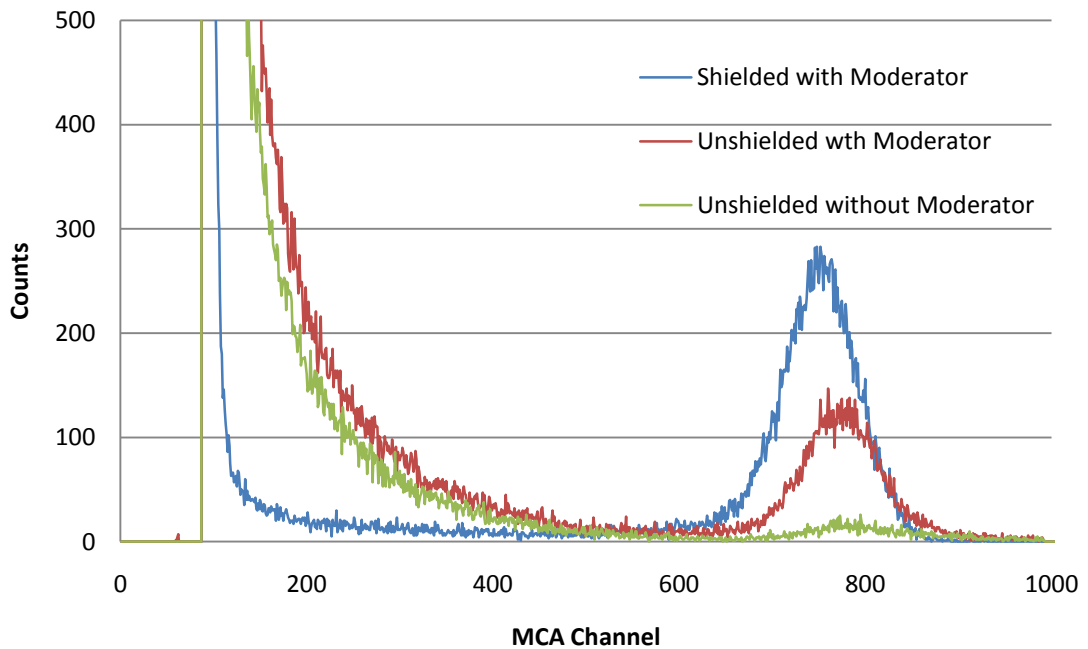


Figure-5.13: Three neutron spectra showing the thermal peak and continuum with varying moderator configurations. Note how the continuum is much stronger when the source is unshielded. The small peak shift observed here is believed to be due to temperature variations.

Given that the continuum becomes strongest when no moderating material is present, especially when the source is unshielded, the reaction is likely to be due to fast neutrons. In the case where the moderator is removed, the 4.8MeV peak is still present due to neutrons moderated in the light guide scattering back into the crystal.

The continuum extends at least up to the thermal neutron peak at 4.8MeV, too high for  $\beta$ -particles from iodine. Also, neutron activation is more likely for thermal neutrons and so the continuum should get stronger when more moderation is introduced which is observed to not be the case.

In conclusion, the continuum is most likely to be due to fast neutrons scattering off lithium nuclei causing them to decay in a three body reaction.

#### 5.4.6. The Temperature Response of the SiPM-LiI(Eu) Combination

A handheld radiation sensor can be expected to operate in the range +50°C to -20°C. Both the SiPM gain and LiI(Eu) light output are dependent upon temperature, so the temperature response of the detector was measured. The range +20 to 0°C was explored in order to establish the magnitude of the effect.

Temperature cycling was performed using a programmable environmental chamber set to dwell at 10°C increments for 2 hours with the intervening steps taking 15 minutes. The time required for the SiPM and crystal to reach equilibrium was 1.5 hours. Temperatures were taken every minute by two sensors, one in contact with the SiPM and one outside the detectors light box in the chamber. Spectra were taken when the SiPM had reached the desired temperature. A shielded source was placed close to the detector in order to maximise counts in the peak for good resolution. The pulse height spectra were recorded and are shown below in Figure – 5.14.

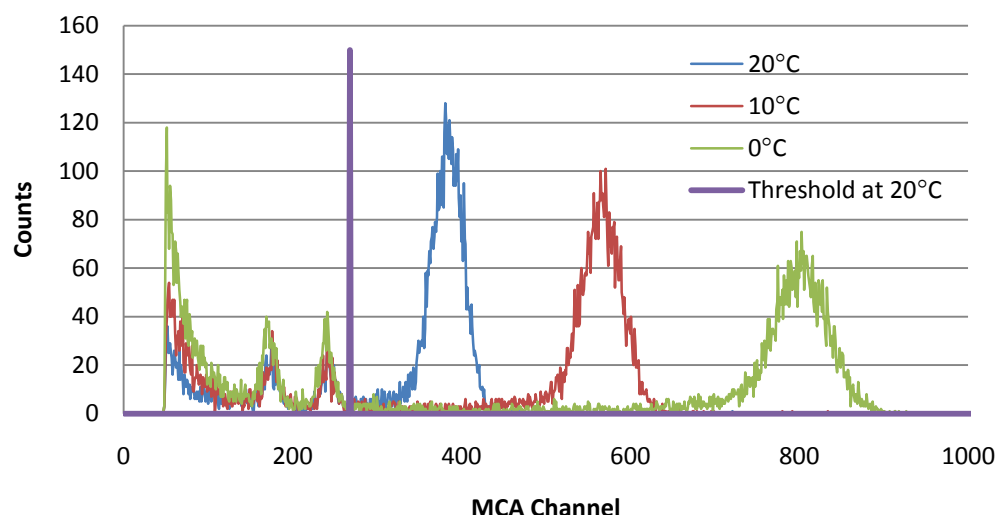


Figure-5.14: The neutron spectra taken at three temperature intervals. Also shown (in purple) is the energy threshold as set at 20°C. The twin peaks just below the threshold are attributed to electronic noise from the digital temperature sensors.

The temperature response of the detector was strong and the thermal neutron peak moved at a rate of  $-3.8\%/^{\circ}\text{C}$ . The strong movement of the peak allows the background count rate to increase by 75% over  $20^{\circ}\text{C}$ , as a greater fraction of the spectrum moves above the threshold. This effect is very pronounced when the  $\text{Co}^{60}$  source is present with an increase of 210%. Therefore, some mechanism is required to stabilise the detector against temperature changes to prevent an increase in false alarms when the detector is cold.

Since this instrument does not require a spectrum to measure neutron count-rates, merely a count-rate above a threshold, a solution with simple electronics is desirable, such as varying the SiPM bias to compensate for temperature induced changes. Digitally controllable bias supplies and resistors are commercially available which can be programmed to vary the SiPM bias supply by  $25\text{mV}/^{\circ}\text{C}$ . This means that the neutron peak can be measured once and an energy threshold set in hardware allowing for simple readout electronics. Should a temperature change occur, the SiPM bias will be reduced to ensure that the threshold remains six standard deviations from the peak.

#### **5.4.7. Summary of the Evaluation Device**

In conclusion, this first exploration of using a SiPM in neutron detection has been mostly successful in that a practical specification was met with a compact detector of 58cc.

Combining a SiPM with  $\text{LiI}(\text{Eu})$  gave good performance by exploiting the good spectral match between them. Excellent gamma-ray rejection was achieved by not allowing direct interactions in the silicon and by exploiting the high Q-value of lithium. Bias requirements are also low (30V) and the detector is likely to be robust, though no shock testing was done, as expected from the characteristics of SiPMs. Importantly, it was demonstrated that comparable performance (per unit volume) to a  $\text{He}^3$  tube can be achieved, implying that such devices can compete, useful when  $\text{He}^3$  supplies become increasingly limited [5-20]. This achievement is important as using  $\text{LiI}(\text{Eu})$  avoids the attendant problems of  $\text{He}^3$ , such as handling problems due to the pressurised tube and high voltage power supply.

The moderator configuration used here was adequate to the task but not ideal in that the detector was less sensitive to fast neutrons coming from a bare source, increasing the required integration time. A thicker moderator would improve sensitivity though at the expense of specific sensitivity, through increased volume and mass. Considerations of solutions to these technical problems form the remainder of this chapter.

## 5.5. Potential Improvements

### 5.5.1. Removing Inefficient Use of Volume

$\text{LiI}(\text{Eu})$  delivers good performance, but it is hygroscopic and the hermetic packaging wastes volume. Of the total 29mm by 8mm package with a volume of 5.3cc, only 1.3cc is  $\text{LiI}(\text{Eu})$  and the remaining 78% of the volume is wasted. It is also expensive and of limited availability, limiting its utility in mass-produced instruments.

Lithium glass may be an alternative to  $\text{LiI}(\text{Eu})$  as it is not hygroscopic so no aluminium and glass package is required, avoiding the 78% wastage of volume. In this study, only  $\text{Li}^6$  enriched glass is of interest. Such glass is marketed under the name GS20 by most manufacturers.

Monte Carlo simulations like those in section 5.3.5 were carried out assuming a GS20 scintillator. In order to determine the advantage gained from using GS20, the moderator configuration was not changed from that in Figure-5.7. The GS20 was set to be 29mm in diameter and 5mm thick (5.3cc), matching the outer dimensions of the  $\text{LiI}(\text{Eu})$  can; as no can is required a greater volume of GS20 than  $\text{LiI}(\text{Eu})$  may be used for the same total volume. These models predict high sensitivity, with a count rate of 0.92 n/s when exposed to a bare source, giving an integration time of 9 seconds. This improvement can be attributed to the greater volume of the GS20 disk. Therefore, GS20 may be a superior choice if good gamma-ray rejection can be achieved.

Unlike  $\text{LiI}(\text{Eu})$ , GS20 has a lower light yield when excited by heavy particles than gamma-rays. The typical light output is 6000 photons for a neutron and 4000 ph/MeV for gamma-rays [5-13]. The alpha/beta ratio is therefore calculated to be 0.31, compared to 0.63 for  $\text{LiI}(\text{Eu})$ . Therefore, 5200 photons can be expected for a 1.3MeV gamma-ray, indicating that a resolution of 1.7% ( $1\sigma$ ) is required for a good separation between neutrons and gammas. Such a resolution is unrealistic so the thermal neutron peak and 1.3MeV gamma-rays will overlap. Poor gamma-ray rejection relative to the  $\text{LiI}(\text{Eu})$  used here is evident in this spectrum from GS20 datasheet from Applied Scintillation Technologies [5-12] (Figure – 5.15).

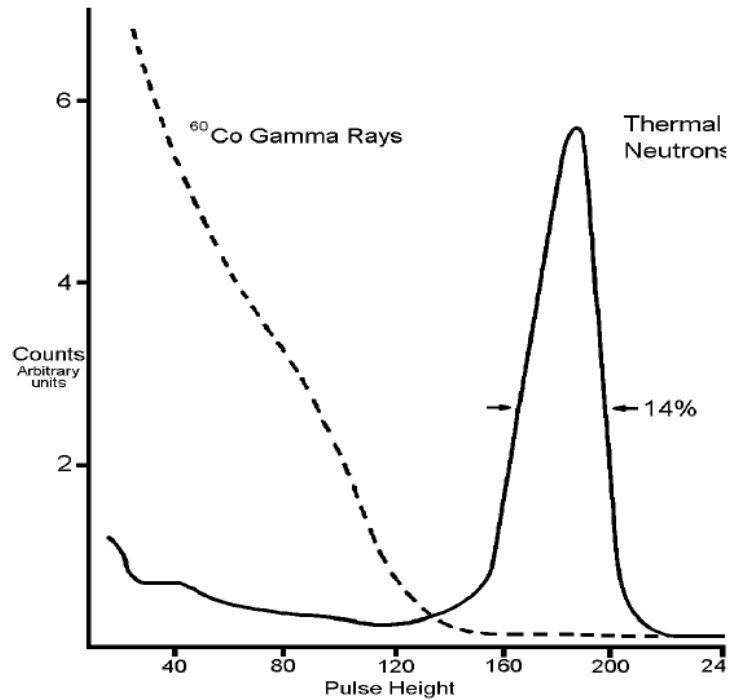


Figure-5.15: A thermal neutron spectrum compared to a  $\text{Co}^{60}$  spectrum from the AST datasheet for GS20. Note the clear overlap which would prevent the use of pulse height discrimination without rejecting genuine neutrons.

From this, we conclude that whilst GS20 offers potentially good sensitivity, the separation of the neutron peak and 1.3MeV gamma-ray photopeak is too poor so either gamma-ray rejection will be poor or the energy threshold will need to be set so high that many neutrons are rejected, negating the increased sensitivity.

### 5.5.2. Exploiting the Operator as Extra Neutron Moderator

An alternative to increasing efficiency is to use a much larger moderator to increase the collecting volume at the expense of geometric thermal neutron losses. However, increasing the depth of moderator around the scintillator reaches a limit as the detector becomes unacceptably large and heavy.

This limit may be side-stepped if the neutron detector is placed within the grip of a handheld detector, so that the operator's hand acts as the moderator. Therefore, less moderator is required in the instrument itself, saving volume and mass. Human tissue is predominantly light elements, with hydrogen being common, so it is potentially a useful neutron moderator.

To assess how effective this may be, the neutron detector was tested against the same DNDO specification as before, but with the addition of a human hand gripping the moderator.

Measured count rates were compared against control measurements taken with the detectors supported away from the lab benches as before and no operator present. The detectors were held 30cm in front of the body to simulate a handheld instrument being held in a rest position.

The LiI(Eu)-based detector was vulnerable to light leaks and the electronics had to be shielded against noise, so it was kept within an aluminium box of dimensions 10x10x15cm, making it difficult to hold fully. Instead, the detector was placed in the corner of the box and the hand folded closely around that edge. The data is shown in Table-5.9.

<b>Bare Source</b>		
<b>Position</b>	<b>Moderator</b>	<b>Hand + Moderator</b>
control	0.44 ± 0.03	1.02 ± 0.04

<b>Shielded Source</b>		
<b>Position</b>	<b>Moderator</b>	<b>Hand + Moderator</b>
control	2.95 ± 0.07	4.11 ± 0.08

Table-5.9: Data taken using the LiI(Eu) scintillator. Again, the count rates are scaled to a  $4 \times 10^4$  n/s source and the errors are one standard deviation.

Gripping the detector increased sensitivity to a bare source by 131%. When the source was shielded an increase of 39% was observed. In the bare source case, the extra moderator gave a big increase in count rate as detector alone is under moderated for the incident neutron energy spectrum.

In the shielded source case, a small increase was observed because the mean incident neutron energy is lower so losses due to hydrogen capture and geometry are stronger.

The integration time is improved by the greater sensitivity, falling from 23 seconds to 8 seconds, more convincingly within the specified time of 30 seconds.

The conclusion from this experiment is that the compact LiI(Eu) based detector benefits from exploiting its operator as a neutron moderator. This has implications for instrument design, as lighter and smaller neutron detectors can be used. For example, the compact LiI(Eu) detector is sufficiently sensitive to meet the specification when gripped by the hand.

## 5.6. Conclusion on SiPMs in Neutron Detection

The work in this chapter has demonstrated that a viable and competitive neutron detector for use in compact applications can be built using SiPMs and LiI(Eu), with very simple and effective gamma-ray discrimination by pulse height. As SiPMs are immune to direct gamma-ray interactions, they are a useful alternative to PIN diodes in this field.

Whilst the design is successful, it cannot be scaled well to increase sensitivity due to limitations on the size of readily available LiI(Eu) crystals. Simulations and calculations predict that lithium doped glass (GS20) cannot be used in the same way with a light guide due to low light output and a poor match with current SiPMs. It is anticipated that blue-sensitive SiPMs or better LCE will help mitigate this problem. Sensitivity may be otherwise improved by using the operator as a moderator.

The “core” of this design (the SiPM and LiI(Eu)) may also be used as the active element in a Bonner sphere with a collection of appropriate moderators. It is suitable due to being compact, sensitive and immune to gamma-rays.

## 6. Preliminary Study of a Directional Spectrometer

Most current portable gamma-ray spectrometers present the user with no information on the location of the source, obliging operators to search, based on the count-rate measured by the detector. Directional information could reduce the time required to make a search and providing this ability is likely to become a key requirement in future instruments.

This study considers how the advantages of SiPMs as explored over the course of this thesis can be exploited to create a simple and effective directional spectrometer. SiPMs are compact and light and so are more suited to this role than PMTs as multiple detector elements can be more conveniently used.

### 6.1. Key Requirements

As this device is intended to be used as a spectrometer it must compete with existing systems, so the same spectral performance targets as in Chapter 4 are considered here, namely an energy resolution of 7% at 662keV and the ability to resolve 59keV gamma-rays from  $\text{Am}^{241}$  above SiPM noise. To usefully replace current spectrometers, no functionality should be lost so a similar sensitivity to a 2" NaI(Tl) or a 1.5" LaBr(Ce) crystal should be achieved for a similar mass (380g and 220g, respectively). A target for directional performance is derived from the notional search of a 4m square room. A directional resolution of 17° FWHM is desired when observing a  $\text{Cs}^{137}$  source of 1mC at 2m. Such a resolution will give a circle of 0.6m radius on a wall 2m away, within which 70% of the "locations" must lie.

### 6.2. Existing Directional Spectrometer Systems

Various groups have worked on the directional spectrometer concept and the question has prompted a range of solutions.

A directional spectrometer described in [6-1] splits the tasks of spectroscopy and direction finding between two systems. A single lanthanum bromide detector was used to provide the sensitivity required to detect sources and collect spectra for identification. Directional information was provided by a 2x2 array of Geiger counters arranged with their axes vertical and separated by lead shields. By comparing the count rates in the four counters, it was possible to determine the direction towards the source as those in front of the shields would have a greater count rate than those behind the lead shields. This two-detector system added complexity and bulk whilst the use of lead shields increased the unit's weight.

Seifert et al [6-2] [6-3] made use of the room-temperature semiconductor CZT in a compact Compton imager. Compton imaging relies on multiple interactions of a single gamma-ray with a position sensitive detector. The energy transfer in a Compton scatter interaction is a function of scattering angle (see Equation 1.2) so it is possible to calculate the direction of an incident gamma-ray based on the locations and energy deposits of two interactions. Phillips in [6-4] gives a good introduction to Compton imaging. As CZT is only presently available in small diodes (>1cc) it lends itself well to this application, as large numbers of small pixels are required and the good energy resolution (1% at 662keV) of CZT can be exploited. This system proved effective in simulation as it derives directional information from each gamma-ray, so an image may be constructed instead of simply indicating a direction. Drawbacks include complexity and low sensitivity due to the low probability of a gamma-ray interacting twice in such a small detector.

The detector described in [6-5] exploits how the energy loss spectrum obtained using CZT depends on where in the diode the energy is deposited. Low energy gamma-rays (60keV in this case) do not penetrate far and so will interact in different parts of the diode depending on angle of incidence, such that the angle may be determined from the shape of the spectrum. This is a simple concept and may be implemented with a single detector, but it is limited to low energy gamma-rays with short attenuation lengths in CZT.

### **6.3. Detector Concept and Operating Principle**

The detector under consideration here is made up of four equal elements with individual readout stacked in a 2x2 array. The array is aligned so that the long axis of each detector element is pointing horizontally (forwards in a handheld instrument). Readout is achieved by a SiPM array in contact with the entire area of one end of the element, to ensure good LCE. Directional information is obtained by comparing counts in these mutually shielding detector elements. Figure–6.1 shows the four detector elements with the line to the source and boresight line defined.

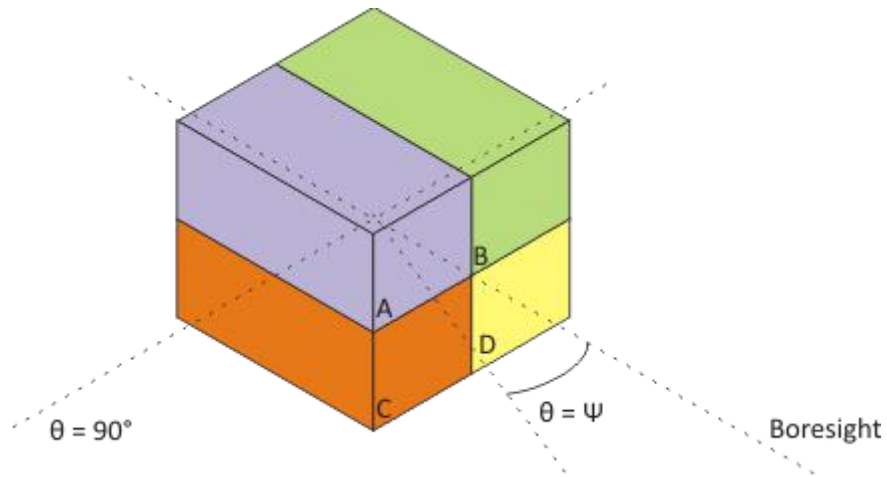


Figure-6.1: A sketch of the four detector elements and the definition of coordinates

A source aligned with the axis of the detector (at “boresight”) will cause an equal number of counts in each element. When a source is at  $90^\circ$  from boresight, to the side of the detector, two detector elements (A and C) will shield the other two (B and D) and a transfer function exists between these two extremes. Therefore, by comparing the four count rates, it is possible to determine the direction towards the source in 3-dimensional space.

During operation, it is intended that locating the source will rely on a cycle of operations. Counts will be collected in the four detectors over an integration period and the direction and angle from boresight presented to the user. The operator will then rotate the device in that direction and collect counts over another integration time. If the four count rates are equal, then the source is on boresight. A torch or laser can then be shone forward to show the region in which the source is believed to be located as a circle projected onto the surroundings, defined by the directional resolution.

The operator will then move in that direction, toward the source, and repeat the cycle with the volume of the cone reducing each time. The operator therefore makes up part of the feedback loop for locating the source. Direction and angular distance may be expressed visually for a more intuitive interface, perhaps as a grid of four squares, the area of each corresponding to the count rate in each element. Finding the source then becomes an exercise in making the areas equal, so that the source is at boresight.

Essentially, this concept uses the combined directional response of the four elements to guide the user towards the source instead of attempting to generate an image, unlike the Compton imager in [6-2]. It is assumed that imaging is not required in the circumstances where a

handheld instrument would be used, where the objective is to rapidly search for a source, rather build up a two-dimensional map of gamma-ray sources in the field of view.

The concept as outlined here has one principal limitation in that it may be confused by multiple sources in different locations or diffuse sources of large area. It may be a reasonable assumption that smuggled material will be in a single location, though this can only be tested by experience. It will also not be suitable for waste or environmental assay where these situations can be expected.

It is possible to avoid this problem to some degree by setting energy bands in the spectrum and seeking the source based on the counts within those bands. Bands may be set based upon the results of an identification of the sources present, being set around full-energy peaks in the spectrum. The directional information for each full-energy peak (in the form of the four squares) may then be compared by the operator to determine if they are co-located or separate, by cycling through the full-energy peaks found in the spectra. Each isotope may then be located individually or, if they are together, the whole spectrum may be used to improve counting statistics. A further advantage of setting energy bands would be the reduction in the background count-rate, as the majority of the gamma-ray background is below 200keV.

#### 6.4. Calculating the Transfer Function

To simplify simulation, the problem is reduced here to two dimensions and the transfer function  $F$  is the difference between the counts  $A'$  and  $B'$  in detector elements A and B as a function of angle ( $\theta$ ). That is:

$$F(\theta) = A'(\theta) - B'(\theta) \quad (6.1)$$

The directional resolution ( $\Psi$ ) is defined to be the angular distance from boresight where  $F(\Psi)$  can confidently be resolved from  $F(0^\circ) = 0$ , that is, at boresight. Figure-6.2 shows this visually. Each number of counts  $A'(\theta)$  will have a statistical error of  $\Delta A'(\theta) = \sqrt{A'(\theta)}$  so the error in  $F(\theta)$  is given by:

$$\Delta F(\theta) = \sqrt{\Delta A'^2 + \Delta B'^2} \quad (6.2)$$

The condition for  $\theta = \Psi$  (resolved) is:

$$F(\Psi) - F(0^\circ) > 1.175 \times \Delta F(0^\circ) + 1.175 \times \Delta F(\Psi) \quad (6.3)$$

That is, for the numbers to be resolved, they must be separated by their FWHM.

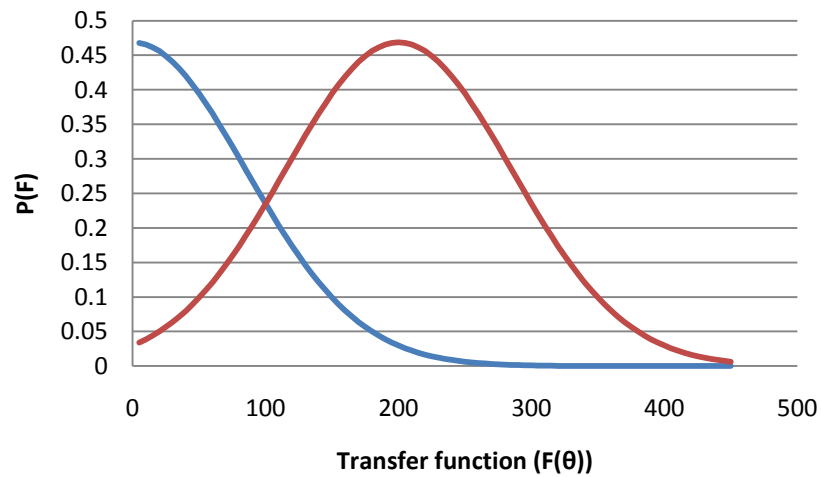


Figure-6.2:  $F(0)$  (in blue) and  $F(\psi)$  (in red) and their resolutions shown as notional peaks. In the case depicted here,  $\theta = \psi$  so the position of the source may be confidently stated in terms of an angular distance from boresight.

Directional resolution depends upon the number of counts in each detector element ( $A'$ ,  $B'$ ) and may be improved by using a long integration time window. Longer integration time windows will give better resolution but will require the operator to hold the unit still and will slow searches.

Directional resolution is also dependant on the gradient of the transfer function, determined by gamma-ray energy and the detector element stopping-power and volume. That is, larger crystals can be expected to give a steeper transfer function, as they shield each other more effectively. Similarly, the transfer function can be expected to be better for lower energy gamma-rays. For these reasons, it is believed that larger detector elements are favourable but this must be traded off against weight and optical performance.

## 6.5. Trial Design and Predicted Performance

The validity of the detector concept was tested using Monte Carlo simulations of a trial design. It was assumed that four elements each of 2x2x4cm would be used. Lanthanum bromide [6-6] was chosen for use in this design over CsI(Tl) for its higher density of 5.08g/cc (compared to 4.5g/cc) so that the attenuation length of incident gamma-rays is as short as possible. This has the dual benefits of increasing sensitivity and giving a steep directional response. Simulations were carried out in two stages: firstly, optical simulations to predict the spectral quality, secondly, gamma-ray simulations to predict the directional response. The source used in the simulations was 1mCi at a distance of 2m.

### 6.5.1. Optical Performance

In terms of optical properties, LaBr(Ce) benefits from a good scintillation efficiency and high speed. It is also a blue scintillator so a good PDE at 380nm is required to exploit it properly; for the sake of this argument the S10931-50 SiPM from Hamamatsu was chosen. It possesses a stated PDE of 40% at 380nm [6-7]. This compares favourably to 3% at 380nm with a SensL 3035X13 SiPM. Table-6.1 gives the key properties of LaBr(Ce) used in these predictions

Yield	63,000 ph/MeV
Peak	380nm
Density	5.08g/cc
Decay	16ns

Table-6.1: The scintillation properties of LaBr(Ce). Taken from the Brilliance380 product datasheet [6-6].

As in Chapter 3, it should also be noted that Hamamatsu do not reject afterpulses and crosstalk when measuring PDE. Bonanno et al [6-8] found different results with a S10362 with 100micron microcells, where the PDE at 380nm was found to be 22%. The packing factor, describing how efficiently the SiPM elements are tiled, must be included. In the case of the S10931, a 53% packing factor reduces the PDE to 12%. For a conservative estimate, 12% is taken to be the PDE at 380nm, superior to the 3% expected of a SensL 3035x13.

A single detector element of 2x2x4cm of LaBr(Ce) viewed by an array of 25 such SiPMs was simulated. An array of S10931 SiPMs would have dimensions 19.25mm x 21.75mm due to the packaging allowing a close fit to the crystal without any tapered light guides.

Optical Monte Carlo simulations were carried out as in Chapter 3, and the predicted LCE and VLCE was used to calculate a noise floor and energy resolution. As before, an isotropic flash of optical photons was moved about within the scintillator volume to generate a range of data, the mean taken to be the LCE and the standard deviation taken to be the VLCE. Simulations were carried out assuming a diffuse reflector of  $\epsilon = 98\%$  (MgO). This gave an LCE of  $75 \pm 6\%$  giving a VLCE term of 8% (at  $1\sigma$ ).

Table–6.2 shows the breakdown of the predicted energy resolution at 662keV. This resolution is sufficient in that it is better than 7% normally achieved with a PMT and CsI(Tl) or NaI(Tl). However, it is worse than the 3% to 4% expected of LaBr(Ce) with a PMT. Note that this is a minimum resolution as no intrinsic term has been included.

$R_{\text{stat}}$	$R_{\text{VLCE}}$	$R_{\text{DR}}$	$R_{\text{T}} (1\sigma)$	FWHM (662keV)
ph	ph	ph	ph	
55	37	7	67	5.2%

Table–6.2: A breakdown of the predicted energy resolution at 662keV.

It is possible to predict the noise floor by scaling from that achieved with LYSO, based on scintillation yield and SiPM array area. Both LaBr(Ce) and LYSO are faster than the SiPM recovery time, so integrating their signals will give the same noise characteristics and same noise floor in terms of photons. It is then a simple matter to scale the number of photons in the 662keV peak to calculate a new noise floor in terms of gamma-ray energy. LYSO coupled to a 16-element array of 3035X13 SiPMs was measured to give a noise floor of 55keV (Section 3.3.3.1). Scaling for light yield ( $63\text{ph}/\text{keV} / 32\text{ph}/\text{keV} = 1.93$ ) and PDE ( $12\% / 9\% = 1.33$ ), gives the total increase in the number of detected photons in the 662keV peak, a factor of 2.56. The noise floor may then be expected to fall to 21keV.

The SiPM array area has increased from 16 elements to 25 so a factor of  $25/16 = 1.56$  must be applied to include the increase in total dark count rate giving a predicted noise floor of 32keV. In this case, the 59keV  $\text{Am}^{241}$  peak will be visible above the tail of the SiPM noise.

Using LaBr(Ce) offers an alternative to CsI(Tl) in that 59keV gamma-rays could be resolved using large arrays (16 or 25 elements) without cooling. This option is made attractive by the good predicted energy resolution. However, in practical applications superior performance must be traded off against cost, as LaBr(Ce) is expensive. LaBr(Ce) may also be used with Hamamatsu SiPMs only, due to their unusually good PDE at less than 400nm.

### **6.5.2. Directional Response Simulation Method**

Simulations were carried out to estimate the transfer function and to determine  $\Psi$ . Although the problem was reduced to 2D, all four detector elements were simulated for realism with each element being a 2x2x4cm crystal of LaBr(Ce).

Directional response was measured by placing an isotropic gamma-ray source at a distance of 2m and moving it from  $\theta = 0^\circ$  to  $\theta = 90^\circ$  in  $5^\circ$  increments, calculating  $F(\theta)$  and  $\Delta F(\theta)$  at each step. Two gamma-ray energies were used: 662keV (as specified) and 180keV, chosen as it is a key line of highly enriched uranium, an important source to locate in any concentration. It was assumed that background subtraction would be used so no background counts were included in the simulations.

As multiple detectors are used, it is possible for data to be contaminated by double counting single gamma-rays due to Compton scattering. Anti-coincidence counting would solve this problem and was modelled by tagging gamma-rays as they interact with elements and rejecting those that interacted with more than one. In practice, this will be carried out based on timing and will be assisted by the high speed of LaBr(Ce), which will also reduce the likelihood of pulse pileup.

### 6.5.3. Directional Response Simulation Results

#### 6.5.3.1. Calculating Directional Resolution

The simulations described above were carried out and the number of counts in two identical detectors was recorded and plotted in Figure-6.3 which shows how  $A'$  and  $B'$  vary in the range  $\theta = 0^\circ$  to  $90^\circ$ . The source is 2mCi at 2m emitting gamma-rays of 662keV and a rolling integration time of 15s is used.

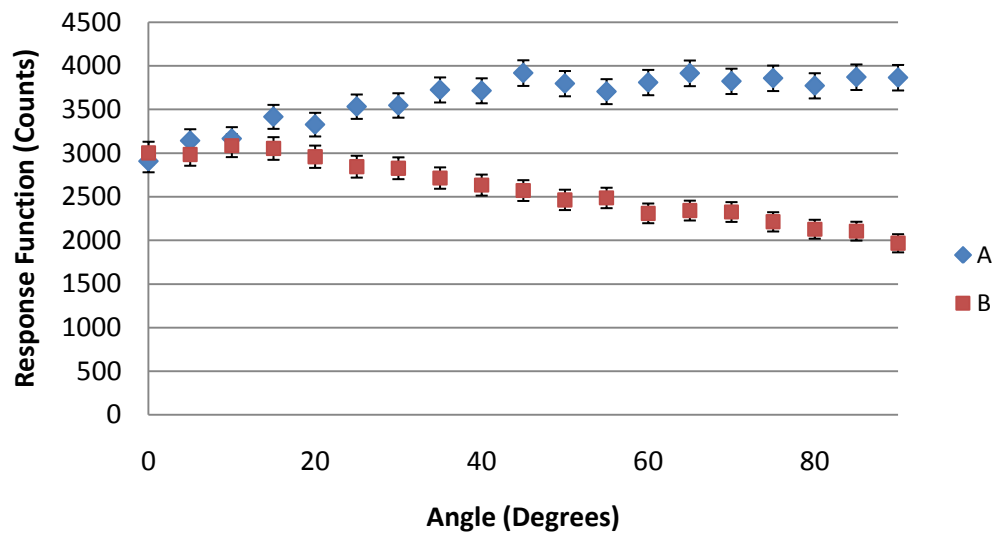


Figure-6.3: The response of detectors A and B to a 662keV gamma-ray source at a range of positions from boresight (Angle=0°) to side-on (Angle=90°). In each case, the gross number of counts in the scintillator is given. The error bars are the statistical error at the level of

$$\pm 1.175\sigma, \text{ where } \sigma_{A,B} = \sqrt{A,B}$$

Figure-6.4 shows the transfer function ( $F(\theta) = A'(\theta) - B'(\theta)$ ) derived from the data above. The error bars are set to  $\pm 1.175\sigma$  with  $\sigma$  being the quadratic sum of  $\Delta A'$  and  $\Delta B'$ .

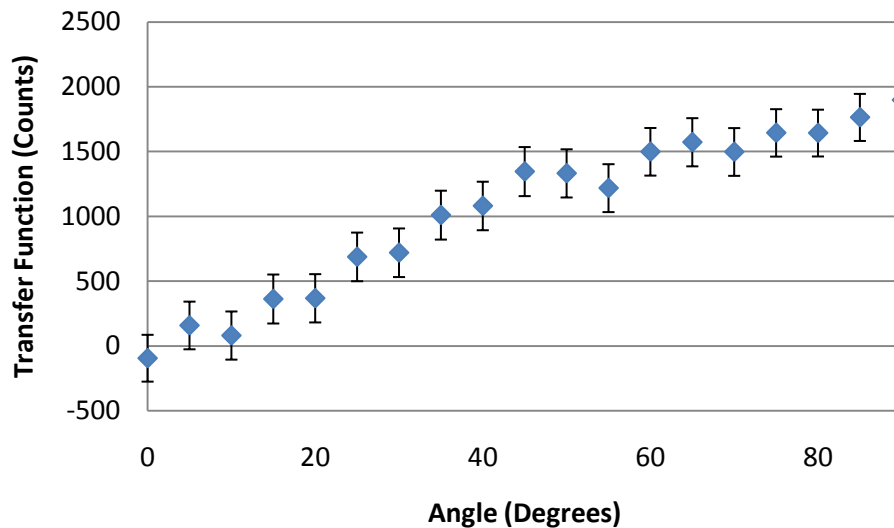
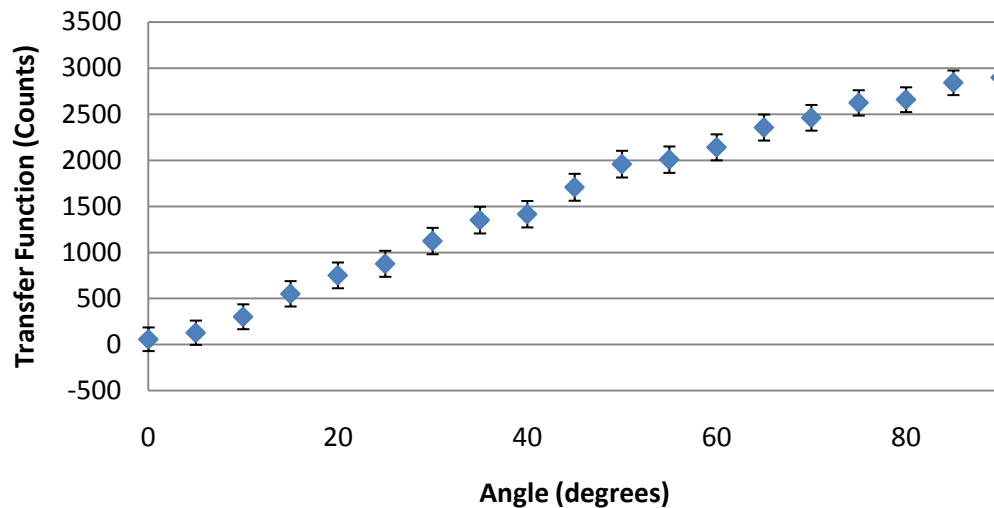


Figure-6.4: The transfer function  $F$  calculated from the simulated data above. The error bars are at  $\pm 1.175\sigma_f$ .

The directional resolution may be read off this plot as the lowest angle where the lower error bar exceeds that of  $F(0)$ . Here it is found to be  $15^\circ$ , when an integration time of 15s was used. Such an integration time is required to ensure that  $\Delta F$  is small enough due to the low gradient of  $F(\theta)$  at 662keV; 27 count/degree from  $\theta = 0^\circ$  to  $30^\circ$ .

Due to this limitation, 3000 counts are needed in each element with the count rate in this case being 190cps in the whole spectrum. The transfer function is curved so the resolution varies from  $15^\circ$  when  $\theta$  is small (near boresight region) to  $30^\circ$  when  $\theta \rightarrow 90^\circ$  (far region). That is, a source at  $60^\circ$  is resolved from one at  $90^\circ$ . Whilst imperfect, this is not an obstacle since the directional response in this range is required to guide the operator to rotate the instrument so that the source is in the near boresight region where resolution is better.

As anticipated, the directional resolution at 180keV is better than at 662keV, achieving  $10^\circ$  (in the near region) and  $10^\circ$  (in the far region), achieved due to the steeper gradient of 106 counts per degree and the higher count rate of 304cps at boresight. Both of these are due to the shorter attenuation length of 180keV gamma-rays. Figure-6.5 shows the transfer function and directional resolution for 180keV gamma-rays and an integration time of 15s.



Figure–6.5: Predicted transfer function for 180keV gamma-rays using an integration time of 15s. The source was 1mCi at 2m.

The integration time of 15s (at 662keV) can be shortened in practice by setting the number of counts in each element instead of an integration time. That is, 3000 counts are needed in each element to achieve  $\Psi = 15^\circ$ , so the instrument can simply ask the operator to remain still until that number is reached. Strong sources that are of greater interest will then be located more rapidly or more accurately.

In terms of sensitivity, this directional spectrometer is predicted to achieve 88cps (in the 662keV photopeak) in each element, when exposed to the specified  $\text{Cs}^{137}$  source (1mCi at 2m) at boresight; this gives a total of 352cps. In comparison a 1.5" cylinder of LaBr(Ce) was simulated to give 187cps, and a 2" NaI(Tl) detector was simulated to give 293cps in the same circumstances so the sensitivity of the directional spectrometer can be considered superior to existing common spectrometers.

### 6.6. Summary

Simulations suggest that this directional spectrometer concept will work well and provide adequate directional resolution using a simple detector and method. This concept is better suited to locating strong sources, with the integration period scaling linearly with source strength (for a fixed distance). Lower energy sources such as  $\text{Am}^{241}$  (59keV) and HEU (180keV) will be located more rapidly (or more accurately) due to a higher linear attenuation so the transfer function is steeper for low  $\theta$  and count statistics are better. Both sources are key to detecting atomic weapons so this is a significant advantage.

Superior sensitivity to 1.5" LaBr(Ce) crystals of 220g is achieved with a scintillator mass of 325g. However, the extra weight of the scintillators is not compounded by the weight of four PMTs. A 1.5" PMT such as 9972B [6-9] from Electron Tubes has a mass of 60g so a total of at least 240g may be avoided by using SiPMs instead of PMTs. PMTs would also require magnetic shielding, further driving up the weight.

The ability to provide directional information with a detector that is lighter than existing spectrometers indicates strong potential in the chosen field, though it depends strongly on improvements in SiPM technology and relies on expensive materials so material cost may need to reduce before it could be a viable solution.

The use of SiPM technology and LaBr(Ce) helps make this a viable instrument. Due to the size of the crystal, a PMT would typically be used due to its low photocathode noise. However, four PMTs would make the instrument far heavier and bulkier than is desirable. SiPMs offer high gain for a greatly reduced weight, whilst the high speed of LaBr(Ce) mitigates the noise problem encountered with SiPMs. Therefore, even though the required SiPM array is large, the noise floor is still low enough for Am<sup>241</sup> to be resolved.

## 7. Summary

Silicon photomultipliers (SiPMs) were evaluated for their potential contribution to the field of radiation sensing, specifically gamma-ray and neutron detection. In the case of gamma-ray detection, SiPM were tested using common scintillators and the resultant performance was considered in the context of a range of applications. By this process, a number of applications were identified where SiPMs could offer advantages over existing systems using PMTs or silicon diodes.

### 7.1. Gamma-Ray Sensors

Evaluation of SiPMs with gamma-ray scintillators began with coupling small inorganic crystals to single devices of  $9\text{mm}^2$  from SensL. Two crystals were used, CsI(Tl) and LSO, chosen for the difference in decay times in order to investigate how speed determines performance. A single 3035X13 SiPM from SensL was used and pulses were passed to an integrator with two selectable shaping times of  $2.2\mu\text{s}$  and  $0.4\mu\text{s}$  for CsI(Tl) and LSO. The integration time for LSO was limited by the bandwidth of the preamplifier.

It was found that LSO provided the best noise floor by virtue of its high speed which prevented the collection of a great deal of noise over the integration time. On the other hand, CsI(Tl) had a worse noise floor but better energy resolution due to higher photon stats.

Potential applications for these small sensors were considered and it was found that the LSO-SiPM combination would be very suitable for use in a PET imaging system. SiPMs have high gain so multiple detectors can be used without the expense of high performance preamplifiers. Cost advantages may also arise from mass production using conventional CMOS techniques. They are also very small and so can be packed into dense arrays without the need for complicated light pipes. Performance is also comparable to current APD and PS-PMT systems at 11% at 511keV. Such small devices could also be used in personal dosimeters. The spectroscopic performance is sufficient to provide enough information for energy calibrated dose, an advantage over simpler dosimeters.

Using SiPMs in other fields requires larger SiPMs or tiled arrays. Three arrays of 4, 9 and 16 elements were sourced from SensL and tested. Firstly, the comparison of different scintillators with SiPMs was expanded to include CsI(Tl), CsI(Na), NaI(Tl), LSO and BGO. It was found that as expected, the speed of LSO led to good performance, as did the brightness of CsI(Tl). CsI(Na) and NaI(Tl) offered the chance to measure how noise floor depended on pulse length

more directly as they had very similar light yield and SiPM spectral match. It was found that, as expected, the faster of the two had the better performance almost by a factor of two.

The use of tiled arrays allowed a direct comparison of how SiPMs perform compared to PIN diodes of the same size ( $1\text{cm}^2$ ) when viewing CsI(Tl). It was found that the 9-element array when coupled to a crystal of  $9\times 9\times 18\text{mm}$  gave a similar noise floor to a PIN diode of around 35keV but the energy resolution was worse at 9% at 662keV compared to 6%. Poor resolution is due to a lower PDE (16% compared to 80%) reducing photon statistics. Typically, this would also worsen the noise floor. However, part of the PIN diode noise floor is electronic noise from the preamplifier, the contribution of which is negligible in a SiPM due to gain. Therefore, the SiPM noise floor is solely comprised of noise counts generated in the photosensor itself.

A  $1\text{cm}^2$  SiPM coupled to a CsI(Tl) crystal like this may be used as an element in a coded mask gamma-ray telescope. High gain allows for simple and cheap preamplifiers to be used, and SiPMs have much thinner depletion regions so direct interaction of gamma-rays and charged particles with the photosensor are unlikely. Whilst the spectral resolution achieved with SiPMs is inferior, gamma-ray telescopes do not perform spectroscopy and typically collect counts in wide energy bands, so energy resolution is less significant.

The same SiPM-CsI(Tl) crystal combination could be used as a small portable spectrometer for use in homeland security applications. Both 9- and 16-element arrays could be used, though sensitivity (through volume) would be traded off against noise floor, as the 16-element array had a noise floor of 75keV and so could not resolve 59keV gamma-rays from  $\text{Am}^{241}$ . Such a device would be more compact than one using PMTs and cheaper than one using CZT semiconductor diodes, although in the latter case the advantage comes at the cost of spectral resolution (9% at 662keV compared to 1%). CZT is also typically only used in small volumes (<1cc) due to charge trapping in large crystals, so a CsI(Tl) crystal read out by a SiPM would have the advantage of sensitivity. Due to the small volume of the crystals, 1.5cc in the case of the 9-element array and 5.5cc in the case of the 16-element array, sensitivity is limited, and so these detectors could only be used in handheld or wearable instruments.

Development of a gamma-ray spectrometer of greater sensitivity was therefore carried out in order to evaluate how SiPMs could be used in large portable spectrometers. Typically a 2" cylindrical crystal of NaI(Tl) or more lately LaBr(Ce) coupled to a PMT is used in these instruments.

Any spectrometer would be constrained by the small size and high noise of the SiPMs used. Therefore, it was decided to explore the concept of a spherical spectrometer, which relied on

multiple diffuse reflections to achieve a uniform and high LCE with a large crystal and small photosensor. Such spectrometers had been explored before using PIN diodes and it was found that whilst the energy resolution achieved was good (7% at 662keV), the noise floor was limited to roughly 200keV by electronic noise due to the lack of intrinsic gain.

Through testing a range of sphere sizes with a 16-element array, it was found that, a sphere of 21cc and a percentage contact area 5% had the same LCE as the square block, leading to the same noise floor (75keV) and energy resolution (9% at 662keV) whilst having 3.8 times the volume. This result indicated that the ScintiSphere concept was useful in this context in that a larger crystal can be coupled to a SiPM without losing spectral performance.

A 9-element array was coupled to a sphere of 8cc, maintaining a percentage contact area of 5%, so that a noise floor of 35keV might be achieved, as with the 9x9x18mm square crystal. The noise floor was measured to be 35keV and the resolution 9% at 662keV. Therefore, the Scintisphere concept allowed the volume of a small spectrometer using SiPMs to increase by a factor of 5.3. This restriction could be overcome and larger spheres used if the PDE of SiPMs were to increase or the noise to decrease.

Whilst this volume of scintillator is not suitable for large handheld spectrometers it is superior to the volumes of CZT typically used, trading sensitivity for energy resolution. It is also greater than what could be achieved using simple square crystals.

Therefore, the conclusion of these chapters is that SiPMs hold great potential in the field of gamma-ray sensing, but it may take time for that to be realised to its full potential. At present they are suitable for replacing PIN diodes and APDs in small applications like PET imagers, gamma-ray telescopes and small spectrometers (up to 21cc depending on the low energy threshold desired). In the future they may be used with ScintiSpheres of volume ~50cc, comparable to 1.5" cylinders typically used in handheld spectrometers. When this happens, they will be suitable to replace small PMTs in the handheld spectrometer market, where their inherent advantages of size and robustness will bring great benefits.

## 7.2. Neutron Counters

The use of SiPMs in neutron detection was evaluated by developing a neutron counter and comparing it to an established instrument (3" long He<sup>3</sup> tube) and a published specification for a neutron detector for use in handheld gamma-ray spectrometers. By choosing a specification it was possible to guide development and establish the utility of the developed detector.

Lithium iodide was chosen as the neutron scintillator for its high light yield (11000ph/MeV) and good thermal neutron attenuation. Based on optical Monte Carlo simulations it was decided that a tapered light guide 15mm long would provide sufficient LCE with low VLCE due to multiple diffuse reflections similar to a ScintiSphere. In practice, excellent separation of the thermal neutron peak and Co<sup>60</sup> gamma-rays was achieved. Rejection of Co<sup>60</sup> gamma-rays was reliable with no change in neutron sensitivity or background count rate when tested in a flux of 820 counts/cm<sup>2</sup>/s.

A HDPE moderator was designed to fit around the LiI(Eu) crystal and light guide and was intended to efficiently moderate neutrons and provide a directionally uniform response. It was found that while this detector was not as sensitive as the standard 3" He<sup>3</sup> tube, it was more efficient, defined in terms of sensitivity per unit volume. High efficiency was achieved due to the tight fitting moderator and total opacity of LiI(Eu) to thermal neutrons. As intended, the detector had a uniform response, required to ensure reliable detection regardless of source position.

From this work it was concluded that SiPMs may be useful in neutron detection when coupled to LiI(Eu) as the relatively good light output can be exploited to achieve good gamma-ray rejection. Such a system has advantages compared to He<sup>3</sup> tubes as better sensitivity may be achieved, although this is also a function of moderator design. The detector is also simpler to operate as no high voltage supply is required and there are no pressurised components. Whilst this may be achieved with a PIN diode, gamma-rays can interact directly with the diode, causing false counts above the threshold and circumventing gamma-ray rejection. Such counts can be rejected by pulse shape discrimination, but this is not necessary with SiPMs due to the thin depletion region. Disadvantages with this detector include the expense and limited availability of LiI(Eu).

### **7.3. A Potential Instrument Exploiting Silicon Photomultipliers**

Finally, a potential instrument was considered that exploited the advantages of SiPMs to provide a high-quality, directional spectrometer. In this context the use of LaBr(Ce) as a scintillator with SiPMs was explored due to the good performance of the scintillator and potential good pairing with SiPMs. It was concluded that the SiPM-LaBr(Ce) combination could provide superior spectra compared to CsI(Tl) or LYSO due to the uniquely high speed and light output of LaBr(Ce), combining the desirable traits of both. The predicted energy resolution is 4.7% at 662keV and the predicted noise floor is 35keV, for an array of 25 S10931 SiPMs viewing a 2x2x4cm LaBr(Ce) crystal wrapped in ESR. However, this could only be achieved with blue-sensitive SiPMs from Hamamatsu, despite the poor packing efficiency of tiling individually packaged SiPMs (53%). This offers an attractive alternative to CsI(Tl) as 59keV gamma-rays may be resolved without the use of cooling.

Based on these encouraging predictions it was decided that such a detector could be used in the large handheld market. Using SiPMs allows for very compact detectors that can be used as elements of a larger system. Such a system was proposed which could provide directional gamma-ray spectroscopy by exploiting the mutual shielding of four elements in a 2x2 array aligned horizontally.

Simulations were carried out in Geant 4 to predict the sensitivity and direction-finding performance of an array of 2x2x4cm crystals of LaBr(Ce). The source was 1mCi of Cs<sup>137</sup> at 2m. It was found that the entire detector would be more 1.8 times as sensitive as a 1.5" cylinder of LaBr(Ce). It was also found that the proposed detector had a directional resolution of 15° (FWHM) after collecting counts for 15 seconds. Such good performance is due to the use of a dense scintillator to increase mutual shielding between elements.

In conclusion, this simulation study indicated that the small size and high gain of SiPMs may allow the development of a very promising compact and sensitive directional gamma-ray spectrometer that is light enough to be used in handheld devices.

### **7.4. Final Conclusion**

As a final note, the conclusion of this thesis is that SiPMs are an interesting new photosensor that, through its unique combination of PMT and diode characteristics, is able to replace either in a wide range of applications. At present, performance is limited by low PDE, though in the future this is expected to improve such that they will become an ever more significant part of radiation sensing.

## 8. References

### 8.1. Chapter 1

1-1: G.Knoll , “Radiation Detection and Measurement”, Third Edition, John Wiley & Sons, 2000, pg.219

1-2: “NaI(Tl) and Polyscin NaI(Tl) Sodium Iodide Material Product Data Sheet ”, Saint Gobain Crystals, 104 Route de Larchant, BP 521 ,77794 Nemours CEDEX, France

(<http://www.detectors.saint-gobain.com/MaterialsGasTubes.aspx>. Correct as of 13/07/2010)

1-3: “CsI(Na) and CsI(Tl) Material Product Data Sheet ”, Saint Gobain Crystals, 104 Route de Larchant, BP 521 ,77794 Nemours CEDEX, France

(<http://www.detectors.saint-gobain.com/MaterialsGasTubes.aspx>. Correct as of 13/07/2010)

1-4: “PreLude 420 Product Data Sheet ”, Saint Gobain Crystals, 104 Route de Larchant, BP 521 ,77794 Nemours CEDEX, France

(<http://www.detectors.saint-gobain.com/MaterialsGasTubes.aspx>. Correct as of 13/07/2010)

1-5: “Bismuth Germanate Scintillation Material”, Saint Gobain Crystals, 104 Route de Larchant, BP 521 ,77794 Nemours CEDEX, France

(<http://www.detectors.saint-gobain.com/MaterialsGasTubes.aspx>. Correct as of 13/07/2010)

1-6: “BriLanCe 380”, Saint Gobain Crystals, 104 Route de Larchant BP 521 ,77794 Nemours CEDEX, France

(<http://www.detectors.saint-gobain.com/MaterialsGasTubes.aspx>. Correct as of 13/07/2010)

1-7: G.Knoll , “Radiation Detection and Measurement”, Third Edition, John Wiley & Sons, 2000, pg.235

1-8: “EJ-200”, Eljen Technology, 2010 E. Broadway, Sweetwater , Texas, United States

(<http://www.eljentechnology.com/products.html>. Correct as of 13/07/2010)

1-9: G.Knoll , “Radiation Detection and Measurement”, Third Edition, John Wiley & Sons, 2000, pg.31

1-10: G.Knoll , “Radiation Detection and Measurement”, Third Edition, John Wiley & Sons, 2000, pg.46

1-11: G.Knoll , “Radiation Detection and Measurement”, Third Edition, John Wiley & Sons, 2000, pg.377

1-12: W. E. Burcham, “Nuclear Physics – An Introduction”, Longman Green and Company, 1963, pg.286

1-13: V. McLane et al, “Neutron Cross Sections, vol. 2”, Academic Press, London, 1988.

1-14: M. Wehr and J. Richards, “Physics of the Atom”, Addison-Wesley Publishing Company, London, 1960, pg. 66

1-15: G.Knoll , “Radiation Detection and Measurement”, Third Edition, John Wiley & Sons, 2000, pg.51

1-16: M. Moszyński et al, “Intrinsic energy resolution of NaI(Tl)”, Nuclear Instruments and Methods in Physics Research A, 484, (2002), 259–269

1-17: Charge Sensitive Preamplifier A250, Amptek, Inc., 14 De Angelo Drive, Bedford, MA 01730 U.S.A.

(<http://www.amptek.com/a250.html>. Correct as of 30/07/2010)

1-18: “Vikuiti™ Enhanced Specular Reflector (ESR)”, Optical Systems Division 3M Center, Building 235-1E-54, St.Paul, MN 55144-1000, USA

1-19: “Optical-Grade Spectralon material”, Pro-Lite Technology, Cranfield Innovation Centre, University Way, Cranfield, Bedfordshire, MK43 0BT, United Kingdom

(<http://www.labsphere.com/productdetail.aspx?id=794&catid=>. Correct as of 13/07/2010)

1-20: “GORE DRP Diffuse Reflector Material”, GORE, Corporate Offices, W. L. Gore & Associates, Inc., 555 Paper Mill Road, Newark, DE 19711, USA.

([http://www.gore.com/en\\_xx/products/electronic/specialty/diffuse-reflector-datasheet.html](http://www.gore.com/en_xx/products/electronic/specialty/diffuse-reflector-datasheet.html). Correct as of 13/07/2010)

1-21: A.J. Bird et al, “The Optimisation of Small CsI(Tl) Gamma-ray Detectors”, IEEE Transactions on Nuclear Science, vol.40, (1993), 395-399

1-22: “Photomultiplier Tube R7600-U200”, Hamamatsu Photonics, 2 Howard Court, 10 Tewin Road, Welwyn Garden City, Hertfordshire, AL7 1BW, United Kingdom

([http://jp.hamamatsu.com/products/sensor-etd/pd002/pd394/R7600U/index\\_en.html](http://jp.hamamatsu.com/products/sensor-etd/pd002/pd394/R7600U/index_en.html). Correct 13/07/2010)

1-23: "Photomultiplier Tube R375", Hamamatsu Photonics, 2 Howard Court, 10 Tewin Road, Welwyn Garden City, Hertfordshire, AL7 1BW, United Kingdom

([http://jp.hamamatsu.com/products/sensor-etd/pd002/pd394/R375/index\\_en.html](http://jp.hamamatsu.com/products/sensor-etd/pd002/pd394/R375/index_en.html). Correct as of 13/07/2010)

1-24: "Si PIN Photodiode S3590-18/-19", Hamamatsu Photonics, 2 Howard Court, 10 Tewin Road, Welwyn Garden City, Hertfordshire, AL7 1BW, United Kingdom

([http://jp.hamamatsu.com/products/sensor-ssd/pd041/pd054/pd058/S3590-19/index\\_en.html](http://jp.hamamatsu.com/products/sensor-ssd/pd041/pd054/pd058/S3590-19/index_en.html). Correct as of 13/07/2010)

1-25: L.J. Meng et al, "The Design and Performance of a large-volume spherical CsI(Tl) scintillation counter for gamma-ray spectroscopy", Nuclear Instruments and Methods in Physics Research A, 485, (2002), 468-476

1-26: A.J. Bird et al, "Pulse Shape Analysis of Signals from an CsI(Tl)/Photodiode Detector, Nuclear Instruments and Methods in Physics Research A, 353, (1994), 46-49

1-27: T. Ikagawa et al, "Study of Large Area Hamamatsu Avalanche Photodiode in a  $\gamma$ -ray Scintillation Detector", Nuclear Instruments and Methods in Physics Research A, 538, (2005), 640-650

## **8.2. Chapter 2**

2-1: P. Buzhan et al., "An Advanced Study of Silicon Photomultiplier", ICFA Instrumentation Bulletin, 23, (2001), pg.28.

2-2: E. Garutti, "Silicon-photomultiplier technology and their application in high energy physics detectors", DESY seminar, 2007

(available at: [www-zeuthen.desy.de/physics\\_seminar/transparencies/erika\\_garutti.pdf](http://www-zeuthen.desy.de/physics_seminar/transparencies/erika_garutti.pdf). Correct as of 15/07/2010.)

2-3: G.Knoll, "Radiation Detection and Measurement", Third Edition, John Wiley & Sons, 2000, pg.283

2-4: M. Yokoyama, et al., "Development of Multi-Pixel Photon Counters", SNIC Symposium, Stanford, California. (arXiv:physics/0605241, 2006)

2-5: B. Dolgoshein et al., "Silicon Photomultipliers in Particle Physics: Possibilities and Limitations", Proc. of 42<sup>nd</sup> Workshop "Innovative Detectors for Supercolliders" Erice, Italy, 28 Sep - 4 Oct 2003. Publ.: World Scientific, (2004), 442-456

2-6: "MPPC – S10362 series", Hamamatsu Photonics, 2 Howard Court, 10 Tewin Road, Welwyn Garden City, Hertfordshire, AL7 1BW, United Kingdom

([http://jp.hamamatsu.com/products/sensor-ssd/4010/S10362-33-100C/index\\_en.html](http://jp.hamamatsu.com/products/sensor-ssd/4010/S10362-33-100C/index_en.html).

Correct as of 13/07/2010)

2-7: C. Piemonte, "A new Silicon Photomultiplier structure for blue light detection", Nuclear Instruments and Methods in Physics Research A, 568, (2006), 224–232

2-8: "SPMMicro – 3035", SensL, Lee House, Riverview Business Park, Cork, Ireland

(<http://sensl.com/products/silicon-photomultipliers/>. Correct as of 13/07/2010)

2-9: D. Motta, "Optical properties of alkali photocathodes", Nuclear Instruments and Methods in Physics Research A, 539 (2005), 217–235

2-10: "Si PIN Photodiode S3590-18/-19", Hamamatsu Photonics, 2 Howard Court, 10 Tewin Road, Welwyn Garden City, Hertfordshire, AL7 1BW, United Kingdom "

([http://jp.hamamatsu.com/products/sensor-ssd/pd041/pd054/pd058/S3590-19/index\\_en.html](http://jp.hamamatsu.com/products/sensor-ssd/pd041/pd054/pd058/S3590-19/index_en.html). Correct as of 13/07/2010)

2-11: H. Moser, "Silicon Photomultipliers, A New Device For Low Light Level Photon Detection", AIP Conference Proceedings, Volume 867, (2006), 98-105

2-12: S. Gomi et al., "Development and Study of the Multi Pixel Photon Counter", Nuclear Instruments and Methods in Physics Research A, 581, (2007), 427–432

2-13: IR-Confocal Emission Microscope: Phemos 1000, Hamamatsu Photonics, 2 Howard Court, 10 Tewin Road, Welwyn Garden City, Hertfordshire, AL7 1BW, United Kingdom "

(<http://sales.hamamatsu.com/assets/pdf/hpspdf/Phemos1000.pdf>. Correct as of 01/08/2010)

2-14: P. Buzhan, "Large area silicon photomultipliers: Performance and applications", Nuclear Instruments and Methods in Physics Research A, 567, (2006), 78–82

2-15: M. A. Ward and A. Vacheret, "Impact of after-pulse, pixel crosstalk and recovery time in multi-pixel photon counter response", Nuclear Instruments and Methods in Physics Research, 610, (2009), 370-373

2-16: Y. Du et al, "After-pulsing and cross-talk in multi-pixel photon counters", Nuclear Instruments and Methods in Physics Research A, 596, (2008), 396-401

- 2-17: G. Bonanno et al, "Precision measurements of Photon Detection Efficiency for SiPM detectors", Nuclear Instruments and Methods in Physics Research A, 610, (2009), 93–97
- 2-18: P.Pakhlov, (ITEP), KEK R&D, Dec. 2005
- 2-19: D. Beznosko et al, "Investigation of a Solid-State Photodetector", Nuclear Instruments and Methods in Physics Research A, 545, (2005), 727-737
- 2-20: S. España et al., "Performance Evaluation of SiPM Photodetectors for PET Imaging in the Presence of Magnetic Fields", Nuclear Instruments and Methods in Physics Research A, 613 (2010), 308–316
- 2-21: C. Merck et al, "Back Illuminated Drift Silicon Photomultiplier as Novel Detector for Single Photon Counting", IEEE Nuclear Science Symposium Conference Record, (2006), 1562-1565
- 2-22: N.K. Doshi, "Comparison of Typical Scintillators for PET", IEEE Nuclear Science Symposium Conference Record, (2002), pg.1420
- 2-23: S. Weber, "Comparison of LuYAP, LSO, and BGO as Scintillators for High Resolution PET Detectors", IEEE Transactions on Nuclear Science, Vol. 50, 5, (2003), 1370-1372
- 2-24: "NaI(Tl) and Polyscin NaI(Tl) Sodium Iodide Material Product Data Sheet ", Saint Gobain Crystals, 104 Route de Larchant, BP 521 ,77794 Nemours CEDEX, France  
(<http://www.detectors.saint-gobain.com/MaterialsGasTubes.aspx>. Correct as of 13/07/2010)
- 2-25: "CsI(Na) and CsI(Tl) Material Product Data Sheet ", Saint Gobain Crystals, 104 Route de Larchant, BP 521 ,77794 Nemours CEDEX, France  
(<http://www.detectors.saint-gobain.com/MaterialsGasTubes.aspx>. Correct as of 13/07/2010)
- 2-26: "PreLude 420 Product Data Sheet ", Saint Gobain Crystals, 104 Route de Larchant, BP 521 ,77794 Nemours CEDEX, France  
(<http://www.detectors.saint-gobain.com/MaterialsGasTubes.aspx>. Correct as of 13/07/2010)
- 2-27: "Bismuth Germanate Scintillation Material", Saint Gobain Crystals, 104 Route de Larchant, BP 521 ,77794 Nemours CEDEX, France  
(<http://www.detectors.saint-gobain.com/MaterialsGasTubes.aspx>. Correct as of 13/07/2010)
- 2-28: "BriLanCe 380", Saint Gobain Crystals, 104 Route de Larchant BP 521 ,77794 Nemours CEDEX, France

(<http://www.detectors.saint-gobain.com/MaterialsGasTubes.aspx>. Correct as of 13/07/2010)

2-29: G.Knoll , “Radiation Detection and Measurement”, Third Edition, John Wiley & Sons, 2000, pg.235

2-30:“EJ-200”, Eljen Technology, 2010 E. Broadway, Sweetwater , Texas, United States

(<http://www.eljentechnology.com/products.html>. Correct as of 13/07/2010)

### **8.3. Chapter 3**

3-1: “CsI(Na) and CsI(Tl) Material Product Data Sheet ”, Saint Gobain Crystals, 104 Route de Larchant, BP 521 ,77794 Nemours CEDEX, France

(<http://www.detectors.saint-gobain.com/MaterialsGasTubes.aspx>. Correct as of 13/07/2010)

3-2: “EJ-260”, Eljen Technology, 2010 E. Broadway, Sweetwater , Texas, United States

(<http://www.eljentechnology.com/products.html>. Correct as of 13/07/2010)

3-3: MultiChannel Analyzer PMCA: MCA-8000A, Amptek, Inc., 14 De Angelo Drive, Bedford, MA 01730 U.S.A.

(<http://www.amptek.com/mca8000a.html>. Correct as of 30/07/2010)

3-4: G.Knoll , “Radiation Detection and Measurement”, Third Edition, John Wiley & Sons, 2000, pg.244

3-5: P. Dorenbos et al, “Non-Proportioanlity in the Scintillation Response and the Energy Resolution Obtainable with Scintillation Crystals”, IEEE Transactions on Nuclear Science, volume 42, 6, (1995), 2190-2202

3-6: Syntfeld-Kazuch, “Non-proportionality and energy resolution of CsI(Tl)”, IEEE Nuclear Science Symposium Conference Record, (2006), 1144-1149

3-7: Erik Mittra and Andrew Quon, “Positron Emission Tomography/Computed Tomography: The Current Technology and Applications”, Radiologic Clinics of North America,Volume 47, 1, (2009), 147-160

3-8: N.K. Doshi, “Comparison of Typical Scintillators for PET”, IEEE Nuclear Science Symposium Conference Record, (2002), pg.1420

3-9: S. Weber, “Comparison of LuYAP, LSO, and BGO as Scintillators for High Resolution PET Detectors”, IEEE Transactions on Nuclear Science, Vol. 50, 5, (2003), 1370-1372

- 3-10: G. Llosa, "First results in the application of silicon photomultiplier matrices to small animal PET", *Nuclear Instruments and Methods in Physics Research A*, 610, (2009), 196–199
- 3-11: D. Herbert, "Study of SiPM as a potential photodetector for scintillator readout", *Nuclear Instruments and Methods in Physics Research A*, 567, (2006), 356–359
- 3-12: A.N.Otte et al, "A test of silicon photomultipliers as readout for PET", *Nuclear Instruments and Methods in Physics Research A*, 545, (2005), 705–715
- 3-13: S. Moehrs et al, "A Small-Animal PET Design Using SiPMs and Anger Logic with Intrinsic DOI", *Conference Proceedings, IEEE-NSS 2004*
- 3-14: "SPMArray2", SensL, Lee House, Riverview Business Park, Cork, Ireland  
(<http://sensl.com/products/silicon-photomultipliers/>. Correct as of 13/07/2010)
- 3-15: "SPMMicro – 6035", SensL, Lee House, Riverview Business Park, Cork, Ireland  
(<http://sensl.com/products/silicon-photomultipliers/>. Correct as of 13/07/2010)
- 3-16: A. Douraghy et al, "Evaluation of Scintillator Afterglow for use in a Combined Optical and PET Imaging Tomography", *Nuclear Instruments and Methods in Physics Research A* 569, (2006), 557–562
- 3-17: H. S. Kim, "Fabrication and performance characteristics of a CsI(Tl)/PIN diode radiation sensor for industrial applications", *Applied Radiation and Isotopes*, 67, (2009), 1463–1465
- 3-18: American National Standards Institute, "N42.48: American National Standard Performance Requirements for Spectroscopic Personal Radiation Detectors (SPRDs) for Homeland Security", 2008, pg.7. Available from "<http://webstore.ansi.org/>" (correct at time of print)
- 3-19: A.J. Bird et al, "The Optimisation of Small CsI(Tl) Gamma-ray Detectors", *IEEE Transactions on Nuclear Science*, vol.40, (1993), 395-399
- 3-20: C. E. Seifert et al, "Directionality in the GammaTracker Handheld Radioisotope Identifier", *IEEE Transactions on Nuclear Science*, vol.56, (2009), 1351-1355
- 3-21: S. Gomi et al., "Development and Study of the Multi Pixel Photon Counter", *Nuclear Instruments and Methods in Physics Research A*, 581, (2007), 427–432
- 3-22: "BriLanCe 380", Saint Gobain Crystals, 104 Route de Larchant  
BP 521 ,77794 Nemours CEDEX, France

(<http://www.detectors.saint-gobain.com/MaterialsGasTubes.aspx>. Correct as of 13/07/2010)

3-23: Flamanc, Jeremy and Csaba Rozsa. "Compact LaBr<sub>3</sub>: Ce Gamma Ray Detector with Si-APD Readout.", CAARI 2008 Proceedings, 2009 AIP Conference Proceedings, 2008

3-24: "EJ-280", Eljen Technology, 2010 E. Broadway, Sweetwater , Texas, United States

(<http://www.eljentechnology.com/products.html>. Correct as of 13/07/2010)

#### **8.4. Chapter 4**

4-1: American National Standards Institute, "N42.48: American National Standard Performance Requirements for Spectroscopic Personal Radiation Detectors (SPRDs) for Homeland Security", 2008, pg.7. Available from "<http://webstore.ansi.org/>" (correct at time of print)

4-2: M. Moszyński et al, "Intrinsic energy resolution of NaI(Tl)", Nuclear Instruments and Methods in Physics Research A, 484, (2002), 259–269

4-3: H. S. Kim, "Fabrication and performance characteristics of a CsI(Tl)/PIN diode radiation sensor for industrial applications", Applied Radiation and Isotopes, 67, (2009), 1463–1465

4-4: A.J. Bird et al, "The Optimisation of Small CsI(Tl) Gamma-ray Detectors", IEEE Transactions on Nuclear Science, vol.40, (1993), 395-399

4-5: L.J. Meng et al, "The Design and Performance of a large-volume spherical CsI(Tl) scintillation counter for gamma-ray spectroscopy", Nuclear Instruments and Methods in Physics Research A, 485, (2002), 468-476

4-6: M. Dallimore et al, "Towards both larger and smaller ScintiSpheres", IEEE Transactions on Nuclear Science, vol.50, 4, (2003), 782-787

4-7: "ICS 4000", LAURUS Systems Inc., - 3505 Ellicott Mills Dr, B-1, Ellicott City, USA

4-8: "Interceptor", Thermo Scientific, 27 Forge Parkway, Franklin, MA, USA

4-9: I. Jung et al, "Simulation studies of CZT detectors as gamma-ray calorimeter", Astroparticle Physics, 26, (2006), 119–128

4-10: "PDS-100G/GN", MGP Instruments Inc., 5000 Highlands Parkway, Suite 150, Smyrna, Georgia, 30082, USA

4-11: "CsI(Na) and CsI(Tl) Material Product Data Sheet ", Saint Gobain Crystals, 104 Route de Larchant, BP 521 ,77794 Nemours CEDEX, France

(<http://www.detectors.saint-gobain.com/MaterialsGasTubes.aspx>. Correct as of 13/07/2010)

4-12:P.S. Marrocchesi et al., "Active Control of the Gain of a3 mm x 3mm Silicon Photomultiplier", Nuclear Instruments and Methods in Physics Research A, 602, (2009), 391–395

4-13: "MPPC", Hamamatsu Photonics, 2 Howard Court, 10 Tewin Road, Welwyn Garden City, Hertfordshire, AL7 1BW, United Kingdom

([http://jp.hamamatsu.com/products/sensor-ssd/4010/S10362-33-100C/index\\_en.html](http://jp.hamamatsu.com/products/sensor-ssd/4010/S10362-33-100C/index_en.html).

Correct as of 13/07/2010)

4-14: M. A. Ward and A. Vacheret, "Impact of after-pulse, pixel crosstalk and recovery time in multi-pixel photon counter response", Nuclear Instruments and Methods in Physics Research, 610, (2009), 370-373

4-15: G. Bonanno et al, "Precision measurements of Photon Detection Efficiency for SiPM detectors", Nuclear Instruments and Methods in Physics Research A, 610, (2009), 93–97

## **8.5. Chapter 5**

5-1: G.Knoll , "Radiation Detection and Measurement", Third Edition, John Wiley & Sons, 2000, pg.524

5-2: K. Anderson et al, "Neutron Irradiation Tests of an S-LINK-over-G-link System", Atlas Tile Calorimeter internal document, (1999).

([http://hep.uchicago.edu/atlas/tilecal/rad/Glink\\_radtest.pdf](http://hep.uchicago.edu/atlas/tilecal/rad/Glink_radtest.pdf). Correct as of 14/07/2010)

5-3: C.R. Heimbach, "Cosmic Coincidences: Investigations for Neutron Background Suppression", Journal of Research of the National Institute of Standards and Technology, 112, (2007), 95-105

5-4: R.T.Kouzes et al, "Cosmic-ray-induced Ship-effect Neutron Measurements and Implications for Cargo Scanning at Borders", Nuclear Instruments and Methods in Physics Research A, 587, (2008), 89-100.

5-5: D.L. Haggard et al, "Neutron Coincidence Counting of Plutonium or is it High-Energy Muon-Induced Time-Related Events in Lead", Proceedings of the SPIE – The International Society for Optical Engineering, vol. 3536, (1999), 159-167.

- 5-6: "Performance Specification for Human Portable Radiation Detection System (HPRDS)", Document number: DNSO-PS-100680v4.00, (2006), pg.20  
(<https://www.fbo.gov/utills/view?id=ace97667742cf0d0e8c1267d63df0cc5>. Correct as of 14/07/2010)
- 5-7: V. McLane et al, "Neutron Cross Sections, vol. 2", Academic Press, London, 1988.
- 5-8: R. E. Krebs, "The History and Use of Our Earth's Chemical Elements: A Reference Guide, Greenwood Press, London, 2006.
- 5-9: S. Mukhopadhyay and H. R. McHugh, "Portable Gamma and Thermal Neutron Detector Using LiI(Eu) Crystals", *Proc. SPIE*, vol. 5198, (2004), pg.73
- 5-10: G.Knoll , "Radiation Detection and Measurement", Third Edition, John Wiley & Sons, 2000, pg.235
- 5-11: A. Syntfeld, "6LiI(Eu) in Neutron and  $\gamma$ -ray Spectrometry – A Highly Sensitive Thermal Neutron Detector", *IEEE Transactions on Nuclear Science*, 2005, vol. 52 (2), 6, 3151-3156
- 5-12: "Lithium Glass Scintillators", Applied Scintillation Technologies Ltd., 8 Roydonbury Industrial Estate, Harlow, CM19 5BZ, UK
- 5-13: C.W.E Eijk, "Inorganic-Scintillator Development", *Nuclear Instruments and Methods in Physics Research A*, 460, (2001), 1-14
- 5-14: D. J. Bennet, "The Elements of Nuclear Power", Longman Scientific and Technical, 1989, pg.38
- 5-15: G.Knoll , "Radiation Detection and Measurement", Third Edition, John Wiley & Sons, 2000, pg.554
- 5-16: Rutherford E. (1911). "The Scattering of  $\alpha$  and  $\beta$  Particles by Matter and the Structure of the Atom", *Philosophical Magazine*, Series 6, 21, 669–688.
- 5-17: R.L. Bramblett et al, "A new type of neutron spectrometer", *Nuclear Instruments and Methods*, vol 9, issue 1, (1960), 1-12
- 5-18: "SK01226", LND inc., 3230 Lawson Boulevard, Oceanside, New York, USA
- 5-19: G.Knoll , "Radiation Detection and Measurement", Third Edition, John Wiley & Sons, 2000, pg.546

5-20: R. T. Kouzes, "The  $^3\text{He}$  Supply Problem", Pacific Northwest National Laboratory Report, PNNL-18388,(2009) ([http://www.pnl.gov/main/publications/external/technical\\_reports/PNNL-18388.pdf](http://www.pnl.gov/main/publications/external/technical_reports/PNNL-18388.pdf). Correct as of 14/07/2010)

## 8.6. Chapter 6

6-1: Carey L Larsson and Salah Djeflal, "Development of a Directional Gamma Ray Probe", IEEE Nuclear Science Symposium Conference Record, (2005), 16-18

6-2: C. E. Seifert, M. J. Myjak, D. V. Jordan, "Simulated performance of the Gamma Tracker CdZnTe handheld radioisotope identifier," IEEE Nuclear Science Symposium Conference Record, (2005), 940-944

6-3: C. E. Seifert et al, "Directionality in the GammaTracker Handheld Radioisotope Identifier", IEEE Transactions on Nuclear Science, vol.56, (2009), 1351-1355

6-4: Gary W Phillips, "Gamma-Ray Imaging With Compton Cameras", Nuclear Instruments and Methods in Physics Research B, 99, (1995), 674-677

6-5: Se-Hwan Park et al, "New concept of CZT-based hand-held radioisotope identifier", Applied Radiation and Isotopes, 67, (2009), 1471–1475

6-6: "BriLanCe 380", Saint Gobain Crystals, 104 Route de Larchant  
BP 521 ,77794 Nemours CEDEX, France

(<http://www.detectors.saint-gobain.com/MaterialsGasTubes.aspx>. Correct as of 13/07/2010)

6-7: "MPPC – S10931 Series", Hamamatsu Photonics, 2 Howard Court, 10 Tewin Road,  
Welwyn Garden City, Hertfordshire, AL7 1BW, United Kingdom

([http://jp.hamamatsu.com/products/sensor-ssd/4010/S10362-33-100C/index\\_en.html](http://jp.hamamatsu.com/products/sensor-ssd/4010/S10362-33-100C/index_en.html).  
Correct as of 13/07/2010)

6-8: G. Bonanno et al, "Precision measurements of Photon Detection Efficiency for SiPM detectors", Nuclear Instruments and Methods in Physics Research A 610 (2009) 93–97

6-9: "9972B series data sheet", ET Enterprises, 45 Riverside Way, Uxbridge , UB8 2YF, United Kingdom

(<http://www.electrontubes.com/>. Correct as of 13/07/2010)